THE HENRYK NIEWODNICZAŃSKI INSTITUTE OF
NUCLEAR PHYSICS POLISH ACADEMY OF SCIENCES

DOCTORAL THESIS

Measurement of the azimuthal anisotropy in Pb+Pb collisions at $\sqrt{s_{\mathrm{NN}}}$ = 5.02 TeV with the ATLAS detector at the LHC

Author:
mgr inż. Klaudia BURKA

Supervisor:
dr hab. Adam TRZUPEK
Auxiliary Supervisor:
dr hab. inż. Tomasz BOŁD

Kraków, 2018

Abstract

Azimuthal anisotropy of particles produced in ultra-relativistic heavy-ion collisions provides unique information about the created hot and dense medium. It is one of the main signatures that, a new state of matter, Quark-Gluon Plasma (QGP) is formed in the nuclear interactions with properties resembling those of perfect fluid, characterised by very low viscosity. The study of azimuthal anisotropy in heavy-ion collisions provides an insight into the initial conditions and collective expansion of QGP. The azimuthal anisotropy originates from the asymmetric shape of the initial volume of the two nuclei interaction. The asymmetry of the collision zone leads to the formation of huge pressure gradients inside the QGP fluid and thereby to intensified particle production along the reaction plane direction. The azimuthal angle distribution of created particles relative to the reaction plane is commonly described by the Fourier series.

The main goal of the thesis is to determine the Fourier harmonics amplitudes, v_n, of azimuthal angle distributions of charged particles produced in Pb+Pb collisions at $\sqrt{s_{\mathrm{NN}}} = 5.02$ TeV in the ATLAS detector at the LHC. Presented analysis utilises the minimum-bias sample of the integrated luminosity of 22 μb^{-1}. Furthermore, the event statistics in the most central collisions are enhanced by dedicated “ultra-central” triggers that sampled the total luminosity of 0.49 nb^{-1}. The v_n harmonics are measured for $n = 2$–7 over an extended transverse momentum range (p_{T} = 0–60 GeV) and wide ranges of pseudorapidity ($|\eta| < 2.5$) and collision centrality (0–80%). The measurements are based on the event-plane and the scalar-product methods. The results obtained with these methods are compared to each other as well as to complementary results of the two-particle correlation analysis and to the measurements from the CMS experiment. Furthermore, the comparisons with measurements obtained with the lower collision energy of the Pb+Pb system ($\sqrt{s_{\mathrm{NN}}}$ = 2.76 TeV), also with new data from the Xe+Xe collision system and to theoretical predictions are also performed. The results obtained in this thesis are one of the most precise measurements of the flow harmonics and thus allow for strong tests of theoretical models, in particular for testing the ultra-relativistic hydrodynamics that is customarily used to explain the QGP evolution.

Streszczenie

Przepływ anizotropowy jest zjawiskiem charakterystycznym dla występowania plazmy kwarkowo-gluonowej (ang. Quark- Gluon Plasma - QGP). Plazma kwarkowo-gluonowa jest to bardzo gorąca i bardzo gęsta materia, która może być wyprodukowana w ultrarelatywistycznych zderzeniach ciężkich jonów. Materia wykazuje właściwości charakterystyczne dla idealnej cieczy z bardzo małą lepkością, dlatego też dobrym źródłem informacji o plazmie jest badanie kolektywnego przepływu cząstek wyprodukowanych w zderzeniach jądrowych. Pomiar anizotropowego przepływu cząstek naładowanych pozwala na eksperymentalne poznanie jej ewolucji w czasie oraz poznanie warunków początkowych. Powszechnie uważa się, że źródłem anizotropii azymutalnej jest asymetryczny kształt początkowego obszaru oddziaływania dwóch jąder. Asymetria kształtu obszaru oddziaływania prowadzi do powstania gradientów ciśnień wewnątrz QGP, w wyniku których obserwuje się wzmożoną produkcje cząstek w kierunku płaszczyzny reakcji. Rozkład kąta azymutalnego wyprodukowanych cząstek względem płaszczyzny reakcji opisywany jest poprzez szereg Fouriera.

Przedmiotem rozprawy jest wyznaczenie harmonicznych rozwinięcia Fouriera, v_n, dla rozkładów azymutalnych kątów cząstek produkowanych w zderzeniach Pb+Pb przy energii $\sqrt{s_{\mathrm{NN}}} = 5.02$ TeV w eksperymencie ATLAS na LHC. Prezentowana analiza wykorzystuje dane minimum-bias o scałkowanej świetlności 22 $\mu\mathrm{b}^{-1}$. Ponadto, statystyka najbardziej centralnych zderzeń jest zwiększona przez użycie dedykowanych wyzwalaczy (ang. “ultra-central” triggers), które zebrały scałkowaną świetlność odpowiadającą 0.49 $n\mathrm{b}^{-1}$. Współczynniki v_n są wyznaczone dla $n = 2$–7 w szerokim zakresie pędów poprzecznych, $0.5 < p_{\mathrm{T}} < 60$ GeV, pseudorapidity, $|\eta| < 2.5$, a także centralności zderzeń jonów, 0–80%. Pomiar anizotropowego przepływu został przeprowadzony przy pomocy dwóch metod badawczych: metody płaszczyzny reakcji (ang. event-plane) oraz metody iloczynu skalarnego (ang. scalar-product). Otrzymane rezultaty są porównane między sobą, jak również z komplementarną metodą korelacji dwucząstkowych (ang. two-particle correlations) oraz z rezultatami eksperymentu CMS. Dodatkowe porównania z wynikami uzyskanymi przy niższej energii zderzenia ($\sqrt{s_{\mathrm{NN}}} = 2.76$ TeV), z wynikami otrzymanymi dla zderzeń Xe+Xe oraz z przewidywaniami teoretycznymi są również zawarte w niniejszej pracy. Prezentowana rozprawa zawiera precyzyjne pomiary współczynników przepływu, które stanowią istotne narzędzie do testów modeli teoretycznych, w szczególności w istotny sposób mogą przyczynić się do uzyskania kluczowych informacji o warunkach początkowych układu, a także do zrozumienia dynamicznej ewolucji plazmy kwarkowo-gluonowej.

Acknowledgements

First and foremost, I would like to express my gratitude to my supervisor dr hab. Adam Trzupek for his guidance, attention and invaluable help during the course of this thesis. I would also like to thank, my auxiliary supervisor, dr inż. hab. Tomasz Bołd for his assistance and continuous support throughout my studies. My special thanks also go to H. Niewodniczański, Institute of Nuclear Physics, Polish Academy of Sciences for healthy work environment and support for all my work. I also wish to thank the members of the Department of ATLAS experiment (NZ14) for creating a friendly atmosphere for work and study. This work was performed within a scope of the Heavy Ion Working Group of the ATLAS experiment. I would like to thank CERN and my collaborators in ATLAS for successful operation of the LHC and data taking with our detector. I am grateful to several ATLAS students and senior colleagues for the very inspiring and friendly atmosphere in the group.

I am especially grateful to my family, friends and my fiance for their support throughout my PhD studies. I thank you all.

This work was supported in part by the National Science Centre, Poland, grant no. 2016/23/N/ST2/01339 and by PL-Grid Infrastructure. I am indebted to the Academic Computer Centre CYFRONET AGH in Kraków, Poland, where my numerical simulations were performed with the use of the computing cluster Zeus.

Contents

Abstract **iii**

Acknowledgements **vii**

1 Introduction **1**

2 Heavy-ion physics **5**
2.1 Quantum Chromodynamics 5
2.2 Heavy-ion collision 7
2.3 Azimuthal anisotropy 9
2.4 Recent results on azimuthal anisotropy in heavy-ion collisions 11

3 Experimental setup **17**
3.1 The Large Hadron Collider 17
3.2 The ATLAS Detector 18
3.2.1 Inner Detector 19
3.2.2 ATLAS calorimetry system 21
3.2.3 Minimum bias trigger scintillators 24
3.2.4 Zero Degree Calorimeter 24
3.2.5 Trigger system 24

4 The dataset description **27**
4.1 Event selections 27
4.2 Pileup removal 29
4.3 Centrality determination 30
4.4 Track quality selections 32
4.5 Monte Carlo simulations 33
4.6 Track reconstruction efficiency and fake rates 34
4.6.1 Efficiency 35
4.6.2 Fake track rates 36

5 Methodology **37**
5.1 Azimuthal anisotropy measurements 37
5.1.1 The event-plane method 37
5.1.2 The scalar-product method 39
5.2 Detailed analysis description 40
5.2.1 Detector calibration: event plane and flow vector uniformity 40
Re-centering Q_n-vector correction 41
Q_n-vector skewness correction 41

- 5.2.2 Tracking corrections 45
- 5.2.3 Flow harmonics measurements with the scalar-product and event-plane methods 45
- 5.2.4 Integrated v_n 47

6 Monte Carlo studies 49
- 6.1 Monte Carlo closure test 49
- 6.2 Sources of Monte Carlo non-closure 50
- 6.3 Fake correction 52

7 Sources of systematic uncertainty 55
- 7.1 Track selection 56
- 7.2 Tracking efficiency 58
- 7.3 Centrality determination 58
- 7.4 Monte Carlo corrections 59
- 7.5 Residual sine terms 59
- 7.6 Variation of FCal acceptance in the $Q_n^{N|P}$ estimation 59
- 7.7 Residual detector non-uniformity 60
- 7.8 Systematics summary 60

8 Results 63
- 8.1 The transverse momentum dependence of $v_n\{\mathrm{SP}\}$ 63
- 8.2 The pseudorapidity dependence of $v_n\{\mathrm{SP}\}$ 65
- 8.3 The number of participants dependence of $v_n\{\mathrm{SP}\}$ 66
- 8.4 The scalar-product and event-plane methods comparison 67
- 8.5 The scalar-product and two-particle correlation methods comparison 69
- 8.6 Comparison to Pb+Pb results at $\sqrt{s_{\mathrm{NN}}} = 2.76$ TeV 70
- 8.7 Comparison to Xe+Xe results at $\sqrt{s_{\mathrm{NN}}} = 5.44$ TeV 72
- 8.8 Comparison to CMS results 73
- 8.9 Comparison to theoretical predictions 75

9 Conclusions 77

A Event plane uniformity 81

B Monte Carlo closure test 85

C Event-plane results 89

Chapter 1

Introduction

The Large Hadron Collider (LHC) [1] is the world's largest and the most powerful particle accelerator. It is located at the European Organization for Nuclear Research (CERN) on the France-Switzerland border near Geneva. The LHC beam operation started up in September 2008, after nearly 20 years of construction. Since then, the proton beams accelerated to the energy (per single proton) varying in the range from 450 GeV to 4 TeV in the first physics operation period in 2010-2013 (RUN-1) and reaching in the second operation period starting in May 2015 (RUN-2) the proton energy of 6.5 TeV. A huge amount of data collected since the LHC startup allowed to make several important measurements in the elementary particle physics. The most important discovery at the LHC up to date, announced on 4th of July 2012, was the observation of the Higgs boson [2] by the ATLAS [3] and CMS [4] experiments. Both, ATLAS and CMS, are large, general-purpose particle detectors investigating a wide range of physics topics, including the study of Higgs boson properties, search for exotic particles and extra dimensions or the heavy-ion (HI) physics. The other two major experiments operating at the LHC, ALICE [5] and LHCb [6], are focused on more specific research. The ALICE experiment is designed to study the heavy-ion collisions, while the LHCb experiment is optimised to perform precise measurements in the heavy-quark sector.

At the LHC, about 90% of the operating time is devoted to the proton-proton physics and the remaining 10% is allocated for ion beams. The main goal of ultra-relativistic heavy-ion collisions at the LHC is to investigate the properties of Quark-Gluon Plasma (QGP) formed in these collisions [7]. During RUN-1 lead ions were collided at the nucleon-nucleon center of mass energy $\sqrt{s_{\mathrm{NN}}} = 2.76$ TeV, and since 2015, during RUN-2, the collision energy reached $\sqrt{s_{\mathrm{NN}}} = 5.02$ TeV. All four major LHC experiments: ALICE, ATLAS, CMS and LHCb[1] collect the ion data and perform heavy-ion physics program.

In the laboratory, the first ultra-relativistic ($\gamma \gg 1$) heavy-ion collisions were performed at the Alternating Gradient Synchrotron (AGS) at Brookhaven and at the Super Proton Synchrotron (SPS) with Au+Au and Pb+Pb collisions at the center of mass energies per nucleon pair of $\sqrt{s_{\mathrm{NN}}} = 11.5$ and 17 GeV, respectively. A big milestone for experimental study of the hot and dense QCD matter was the start of the Relativistic Heavy Ion Collider (RHIC) at Brookhaven. The RHIC provided the opportunity to explore collisions with different types of projectile combinations such as Au+Au, Cu+Cu, U+U as well as asymmetric systems like d+Au and p+Au at varied energies $\sqrt{s_{\mathrm{NN}}} = 7-200$ GeV. Such variety of collision systems provided baseline measurements

---

[1] The LHCb experiment joined the heavy-ion program in 2015.

for the heavy-ion collisions, which led to the discovery of the QGP medium [8–11]. Since then the properties of QGP have been under thorough investigation also at the LHC energies. The LHC performed collisions for different projectile combinations, including collisions of Pb+Pb at $\sqrt{s_{\mathrm{NN}}}$ = 2.76 and 5.02 TeV, p+Pb at $\sqrt{s_{\mathrm{NN}}}$ = 5.02 and 8.16 TeV, as well as Xe+Xe at $\sqrt{s_{\mathrm{NN}}}$ = 5.44 TeV.

In the thesis, the measurements of the azimuthal anisotropy at $\sqrt{s_{\mathrm{NN}}}$ = 5.02 TeV Pb+Pb collisions are presented. The QGP formed in ultra-relativistic heavy-ion collisions collectively evolves (flows) as the interaction region cools down. The collective expansion of produced particles allows to assess fundamental properties of the QGP matter, such as very low viscosity, resembling that of a perfect fluid. Therefore, one of the basic measurements that are commonly performed to examine the QGP is the azimuthal anisotropy in particle distributions, which is sensitive to initial conditions and space-time evolution of the system. Thus, measurements of the anisotropic flow provide a unique experimental information about the properties of created medium. The work is based on two measurement techniques: the scalar-product (SP) method and the event-plane (EP) method that are commonly used in this kind of studies. The azimuthal anisotropy is measured over a wide transverse momentum range of p_{T} =0–60 GeV, pseudorapidity range of $|\eta| < 2.5$ and collision centrality of 0–80%. Results presented in the thesis are the most precise measurements of v_n coefficients over such a broad range of kinematic variables and centrality as well as in ultra-central collisions, which provide information about the initial state dominated by fluctuations.

The thesis is composed of nine chapters and three appendices. Chapter 2 contains an introduction to the heavy-ion physics. The experimental setup is summarized in Chapter 3. Chapter 4 describes the $\sqrt{s_{\mathrm{NN}}}$ = 5.02 TeV Pb+Pb dataset used in the analysis. This includes event and track selection requirements, pileup rejection, event centrality definition and characteristics of basic observables. The techniques used to measure charged-particle azimuthal anisotropy as well as necessary corrections are provided in detail in Chapter 5. A short description of Monte Carlo (MC) studies including "closure tests" and MC corrections applied to the final results can be found in Chapter 6. Chapter 7 contains the description of systematic-uncertainty sources. Results are presented in Chapter 8. Comparisons to v_n harmonics obtained with other measurements techniques, to the CMS results, to the results at the lower system energy ($\sqrt{s_{\mathrm{NN}}}$ = 2.76 TeV) and theory predictions are also included in this chapter. Chapter 9 contains the summary and conclusions. Figures related to the details of the measurement techniques are included in Appendix A. Appendix B covers the MC closure test for v_2–v_6 harmonics, while in Appendix C results obtained with the complementary method are shown.

The results presented in the thesis are part of the ATLAS experiment analysis of a wider scope, which, apart from the measurement based on the scalar-product and event-plane methods also included the v_n harmonics obtained with the two-particle correlation (2PC) method. The paper with the analysis results was just submitted to European Physical Journal C and corresponding arXiv preprint is available at Ref. [12]. In the analysis I was fully responsible for the measurement of v_n harmonics with the scalar-product and event-plane methods reported in this thesis. In particular, the analysis code including all necessary corrections was developed by myself, as well as the code for preparation of all figures relevant for the scalar-product and event-plane methods. I was also involved in validation of the main Pb+Pb $\sqrt{s_{\mathrm{NN}}}$ = 5.02 TeV MC sample, which is used not only in the presented analysis but also it was used in other ATLAS measurements [13–15]. Performance studies presented in Chapter 5 as well as work presented in Chapters 6 and 7 were done by myself.

I took an active role in the preparation of the aforementioned publication as well as a prior conference note [16] which contains preliminary results on the $\sqrt{s_{\mathrm{NN}}} = 5.02$ TeV Pb+Pb v_n harmonics, that were shown for the first time by myself at the *2016 Hard Probes Conference* in Wuhan, China. Proceedings of this presentation are published in Ref. [17]. Moreover, I had presentations at the *Epiphany 2016*, *DIS 2016*, *2016 Polish Workshop on Relativistic Heavy-Ion Collisions* and *WPCF 2018* conferences. Proceedings of the two first presentations are published in Ref. [18] and [19], respectively. I also presented a poster on the results of this thesis at the *Quark Matter2018* conference. I was involved in the analysis of azimuthal anisotropy in $\sqrt{s_{\mathrm{NN}}} = 5.44$ TeV Xe+Xe collisions published as preliminary results in Ref. [20]. The Xe+Xe analysis of azimuthal anisotropy repeated all steps presented in this work using the same code. During the doctoral studies I obtained the National Science Centre grant, "PRELUDIUM", for the azimuthal anisotropy measurement in Pb+Pb collisions using techniques developed for this analysis. In addition, I was also responsible for the development of electron and photon triggers suitable for heavy-ion data taking conditions. Moreover, I took part in the operation effort as an online shifter responsible for monitoring the trigger performance during Pb+Pb and *pp* collisions.

The thesis followed the convention adopted by the ATLAS Collaboration to describe physical quantities. In particular, a speed of light is c =1, which allows to express a momentum or energy in GeV or TeV units as well as the time to be expressed in the dimension of length.

Chapter 2

Heavy-ion physics

2.1 Quantum Chromodynamics

The foundation of high energy physics is quantum chromodynamics (QCD), the theory of strong interactions [7, 21]. The theory is based on the symmetry group $SU(3)_C$ and provides thorough quark-model description of hadrons, strongly interacting particles, composed of quarks that are accessible for direct laboratory study. There are six flavors of quarks: *up*, *down*, *charm*, *strange*, *bottom* and *top*. Each quark comes in three color charges: *red*, *blue* and *green*. For every quark there is corresponding anti-particle noted as anti-quark which is characterised by anti-colors. All particles, that exist in nature, are colorless i.e. their net color charge is zero. This rule implies that hadrons, bound states of quarks, are divided into: *mesons*, consisting of quark and anti-quark, and *baryons* composed of three quarks (or three anti-quarks). In addition to the color charge, quarks also carry the fractional electric charge, which is: $\frac{2}{3}e$ for the *up*, *charm* and *top* flavors, and $-\frac{1}{3}e$ for the *down*, *strange* and *bottom* flavors, where e is the electron's charge. The strong interactions among quarks are described in QCD by mediating (by exchanging of) vector particles called gluons. Gluons themselves, in contrary to photons in electrodynamics, experience the strong interactions by carrying the color charge. This fact implies that gluons can emit and absorb other gluons. Hereafter, an ensemble composed of quarks and gluons is called "QCD matter".

The QCD theory features two interesting phenomena: *color confinement* and *asymptotic freedom*. The *color confinement* [22] implies that quarks or gluons cannot be isolated i.e. cannot be found as single particles. In nature they are bound in hadrons. Phenomenologically, the color confinement may be characterized by the "QCD potential" [21]:

$$V_{QCD} = -\frac{4}{3}\frac{\alpha_S}{r} + kr, \tag{2.1}$$

where α_S is the strong coupling constant, r is the distance between quarks and k is constant ($k \approx 1$ GeV/fm). The first, term of V_{QCD}, dominant at small r, is related to the gluon Coulombian exchange, while the latter stands for *confinement*. The interaction energy increases with the distance between quarks in hadrons. An attempt to pull apart quarks leads to the spontaneous appearance of more and more gluons that strengthen the color field. As a result, a new pair of quarks is produced.

The *asymptotic freedom* was first predicted by Gross, Politzer and Wilczek in 1970s [23–25]. The strong coupling constant, α_S, is dependent on the energy transfer in the interaction. At small distance between partons and large energy transfers $\alpha_S \rightarrow 0$, i.e. quarks and gluons turn into asymptotically free particles. Due to small α_S, the

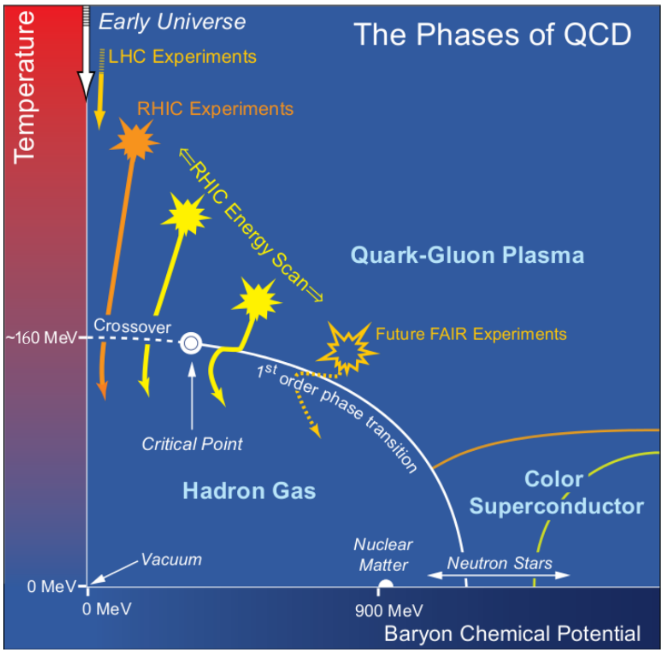

FIGURE 2.1: The phase diagram of QCD matter in the temperature, T, and baryon chemical potential, μ_B, plane. Figure adapted from [28].

process of *asymptotic freedom* can be described via perturbative QCD [26]. In the opposite limit i.e. at low energy transfers, the α_S increases, which is likely related to confinement of color charge at large distances. In this case QCD can not be represented by the perturbation theory. Instead, it is studied using the discrete space-time lattice [27].

The discovery of QCD asymptotic freedom lead to a prediction [29, 30] that at sufficiently high temperature and/or baryon density a deconfined phase of quarks and gluons, the QGP, should be present [8–11]. Properties of strongly interacting matter are usually expressed using thermodynamic parameters: temperature and baryon chemical potential (T, μ_B). It is expected [31] that at vanishing chemical potential the matter go through a phase transition between hadron gas to QGP at critical temperature T_C. Figure 2.1 shows a schematic phase diagram of QCD matter as a function of T[1] vs. μ_B[2]. The origin on this diagram, $T = 0$ MeV and $\mu_B = 0$ MeV, represents the vacuum. The ordinary nuclear matter is observed to be at $T \approx 0$ MeV and $\mu_B \approx 900$ MeV (the mass of nucleon). The region between vacuum and ordinary matter at low temperatures (< 170 MeV) corresponds to so-called "hadron-gas" phase in which the interactions are relatively weak. On the other hand if the μ_B is set constant and the temperature increases, the QGP phase is expected to be reached in which quarks and gluons are not confined within a hadron but form separate degrees of freedom. At small μ_B and high temperature the numerical lattice QCD calculations indicate a smooth transition from hadron gas to QGP, called *crossover*. The point at which the first order phase transition becomes a crossover, known as critical point, is expected to occur at $T_C \sim 154(\pm 9)$ MeV [32, 33]. In the crossover region there is a large increase in energy density $\epsilon(T)$ [33]. The search for the location of the critical point in the QCD phase diagram in the high μ_B region,

---

[1] A temperature of 170 MeV is about $2\cdot10^{12}$K and 273 K is equivalent to $23.5\cdot10^{-3}$eV

[2] Baryon chemical potential is the amount of energy needed to add a baryon to the system

is performed by Shine experiment [34] at SPS, RHIC experiments [35] and also is planned in the future FAIR experiments [36]. It is believed that QGP was present in the early stages of the universe, in a few micro-seconds after the Big-Bang. The transition from a QGP to hadrons occurred at vanishing μ_B and high T, during a rapid expansion and cooling of the early universe. Nowadays, the conditions of low μ_B and high T are recreated and investigated with ultra-relativistic heavy ion collisions at RHIC and LHC. The QGP is also expected to form compact and dense neutron stars at high values of the μ_B and at a temperature close to zero, due to the gravitational collapse.

2.2 Heavy-ion collision

Since heavy ions are extended objects, their collisions are categorised by their overlap area i.e. centrality. Centrality in a given collision is associated with the impact parameter, b, which is the distance between the ions centers. Figure 2.2 shows an illustration of a heavy-ion collision. The b parameter cannot be directly measured in the experiment. The Glauber MC models [37, 38], which describe well the data, indicate that the impact parameter is directly related to the number of participants taking part in the collision, N_{part}, and, thus, to the particles observed in the final state, N_{ch}. Nucleon is considered as participant (or wounded nucleon) if it takes part in at least one inelastic nucleon-nucleon collision. If the nucleon passes through the collision unaffected, it is called a spectator.

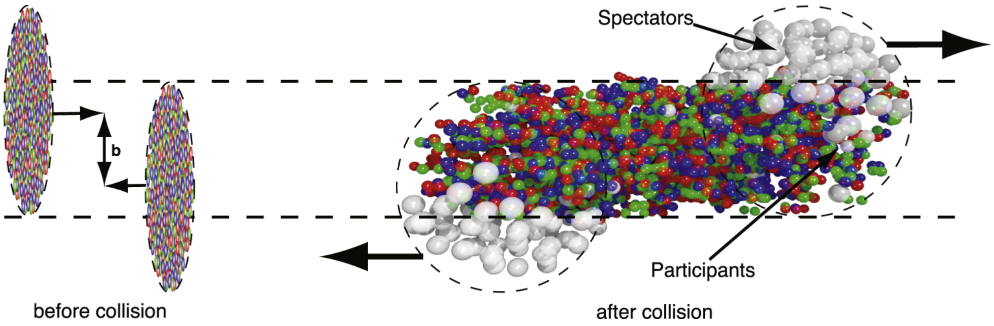

FIGURE 2.2: Simplified sketch of a heavy-ion collision [39]. Left: Two ions before the collision with the impact parameter b. Right: Ions after collision divided into participants and spectators.

An illustration of the space-time evolution of the matter created in ultra-relativistic heavy-ion collisions is shown in Figure 2.3. The system evolves through various stages before the final hadrons are emitted and detected by the detector:

- **Before the collision**: In the lab frame two incoming nuclei are Lorentz contracted along the beam direction. In the Pb+Pb collision at $\sqrt{s_{\text{NN}}} = 5.02$ TeV at the LHC the Lorentz contraction factor $\gamma \sim 2600$. This means that the size of Pb ion is reduced ~ 2600 times along the beam direction.
- **Collision**: At the time $\tau = 0$ the two nuclei collide. The initial stage of a collision is dominated by 'hard' interactions. Hard processes are those involving relatively large momenta transfer ($(Q)^2 \geq (10\text{ GeV})^2$) and hence occur faster (due to uncertainty principle). This leads to the creation of high-p_{T} probes, like jets,

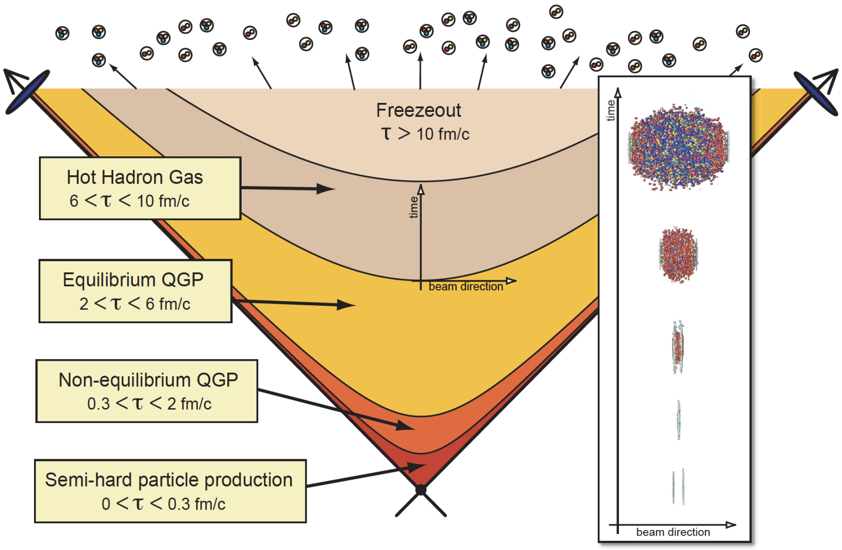

FIGURE 2.3: Diagram of the space-time evolution of a heavy-ion collision. Colors represent the different stages of a collision. Figure adapted from [40].

heavy quarks, photons and EW bosons. At the same time a very fast expansion of the dense medium is expected. The initial-stage partons liberated at this point form a dense medium.

- **Thermalization**: Partons produced in a collision strongly interact with each other. The interactions are mediated between partons despite the fact that they recede from each other very fast as the medium expands. Consequently, the partonic matter comes to local thermal equilibrium in a relatively short time ($\sim$ 1fm).

- **QGP**: The thermalised QCD matter, i.e. QGP, is the next phase of the HI collision. The existence of the QGP phase is well confirmed by the QCD lattice calculations [27]. As the plasma expands, the large pressure gradients are formed inside the matter. It is expected that these gradients are not isotropic due to the initial elliptical geometry of the overlap region of the two nuclei as well as the initial fluctuations of the system. Thus, the expansion of the QGP exhibits the anisotropic nature. The analysis presented in this work is focused on studying the anisotropic features of the QGP.

- **Hadronic rescattering**: The medium continues to expand and cool down. Eventually, when the temperature reaches the critical temperature T_C, quarks and gluons begin to hadronize, i.e. they combine into ordinary hadrons. The scattering interactions between produced particles are still present but system energy is too small to keep partons deconfined.

- **Freeze-out**: The relative chemical abundances for various particle species are expected to be fixed at T_C when the inelastic interactions cease. This is known as *chemical freeze-out*. At this stage system continues to expand and hadrons interact elastically. The system constantly cools down until it reaches the temperature at which the interactions completely fade away. Finally, the system enters the *kinetic freeze-out* stage when the particle momentum distributions are fixed.

- **Free streaming**: Particles produced during the collision move towards the detectors.

High energy heavy-ion experiments are devoted to study interactions between most fundamental particles by producing strongly interacting QCD matter composed of the mixture of weakly bound quarks and gluons. The energy density achieved in ultra-relativistic heavy-ion collisions is high enough for the QGP phase transition to take place. This allows to probe the phase diagram of QCD matter and disentangle the different mechanisms that dominate each collision stage.

The properties of the QGP are inferred via studying the final state hadrons observed in the detector. This is done using different experimental observables that are sensitive to different properties of the medium. There are three main types of probes commonly used in experiments: soft, hard and electromagnetic (EM) probes.

The *soft* term refers to the low transverse momentum exchange (the non-perturbative regime of QCD). These are light particles with the low transverse momentum produced in the hadronization stage. These represent the majority of measured particles. Soft studies are focused on describing the bulk properties of the medium, such as the viscosity or the size of the system, using e.g. p_T spectra, particle correlations and fluctuations, azimuthal anisotropy.

Hard probes are the energetic particles generated in the initial stages of the collision with the high momentum transfer (perturbative QCD regime). Thus, they experience the full evolution of the QGP while traversing it. This is mainly through multiple scatterings with the plasma which eventually results in the suppression of high-p_T spectra and parton energy loss. The mechanisms induced by the QGP are studied using e.g. high-p_T particles, heavy quarks, quarkonia, jet production.

2.3 Azimuthal anisotropy

The anisotropic flow results from the large initial pressure gradients in the QGP created in the collisions. These pressure gradients transform the initial spatial anisotropies of created matter into momentum anisotropies of the final-state particle production, which are experimentally characterized by so-called flow harmonics [41, 42]. Initial theoretical predictions assumed that QGP would behave as a weakly interacting gas of quarks and gluons and consequently unable to develop strong collective expansion. Therefore, the discovery of the large second-order flow harmonic, at RHIC and more recently at the higher-energy LHC [43–45], has changed significantly the understanding of the QGP. Usually, the QGP description is based on relativistic viscous hydrodynamic models [46]. These models typically assume that the system is in local equilibrium and, thus, the description by fluid dynamics is adequate. Recently, it was suggested that a non-equilibrium system can also be described by relativistic hydrodynamics [47].

Figure 2.4 illustrates an example collision between two lead nuclei. During non-central heavy-ion collision, like a Pb+Pb collision at the LHC, interacting nucleons form an almond-shaped fireball oriented so that the long axis is perpendicular to the reaction plane. The shorter axis of the almond fireball lies in the reaction plane by definition.

Large pressure gradients in the system, stronger in the reaction plane direction, act in the initial stage of system evolution. As a result, the initial spatial anisotropy is turned

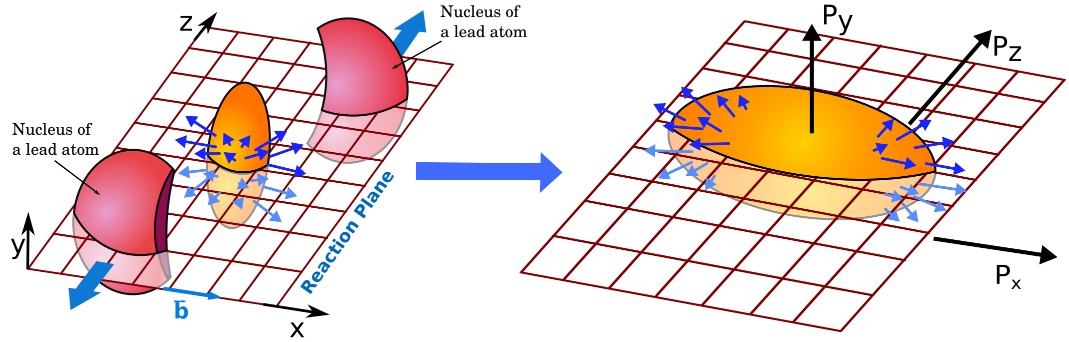

FIGURE 2.4: Sketch of the non-central heavy-ion collision and expansion of the resulting fireball. Orange regions denote a shape of the overlap region (left) and hydrodynamically expanded plasma (right). The reaction plane is defined by the impact parameter b and the z-axis. The coordinate system is chosen so that the impact parameter is oriented in the x direction.

into anisotropy of the final transverse momentum distribution. Particles produced in the collision are thus emitted preferentially in the in-plane direction. This is a global correlation, which affects all particles.

The final distribution of azimuthal angles of produced particles measured with respect to the reaction plane angle is customarily expanded in the Fourier series [48, 49]:

$$\frac{dN}{d\phi} = \frac{N_0}{2\pi}\left(1 + \sum_{n=1} 2v_n \cos\left[n\left(\phi - \Phi^{RP}\right)\right]\right), \tag{2.2}$$

where v_n coefficients are called flow harmonics of n-th order, ϕ is the azimuthal angle of a produced particle and Φ^{RP} is the reaction plane angle. The v_n characterise the strength of the anisotropy. The v_n coefficients are studied as functions of the particle pseudorapidity, transverse momentum and the event collision centrality. The sine terms are negligible due to the symmetry with respect to the reaction plane. The reaction plane angle, Φ^{RP}, can not be directly measured in the experiment, thus, the corresponding symmetry angle for each n-th harmonic is estimated and denoted as Ψ_n. The Ψ_n are estimated, event-by-event, from the particle azimuthal distribution. The measurement techniques explore the fact that the flow phenomenon is global (affect all particles). Therefore, the values of v_n can be extracted from the correlations between disparate regions of phase space. Both the size of the collision overlap region and, for a given size, the number of interacting nucleons fluctuate from event to event. This generates so-called anisotropic flow fluctuations i.e. flow harmonics fluctuations, which arise from the initial fluctuations of the overlap region.

The first harmonic, v_1, is known as *directed flow* and it refers to the sideward motion of particles. The v_n carry an information about the early collision stage. The most extensive studies are related to the second flow harmonic v_2, also known as *elliptic flow*. It is sensitive to the initial spatial asymmetry of the almond-shaped overlapping zone of colliding nuclei. Since the number of wounded nucleons is finite and their initial positions within nuclei can significantly fluctuate from event to event, the initial collision geometry also fluctuates. These initial fluctuations lead to the non-zero values of higher order flow harmonics present in the final particle distributions. Figure 2.5

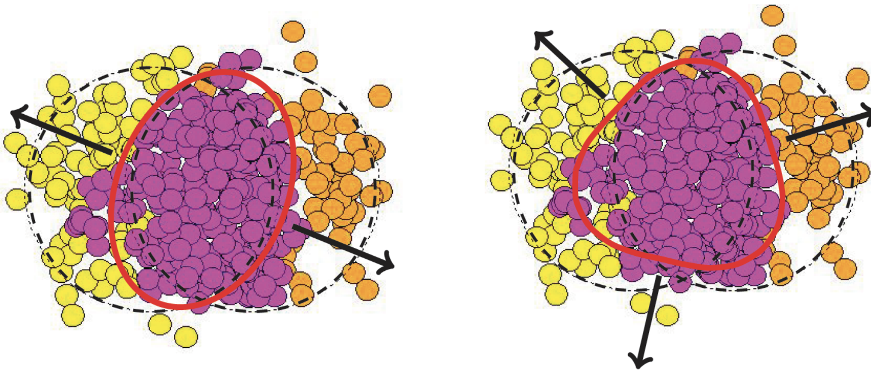

FIGURE 2.5: Schematic distribution of nucleons in the initial geometry of a collision. Both, the second (v_2) and third (v_3) moments of the initial asymmetry can be distinguished. Arrows indicate the event plane angles Ψ_2 and Ψ_3. Figure taken from [50].

shows schematic diagram of fluctuations in the initial geometry including elliptic (v_2) and triangular (v_3) modes. In the LHC RUN-1 data, the Fourier v_n coefficients were measured to be non zero up to 6-th mode, which is the indication of the very low shear viscosity of the QGP medium [51].

2.4 Recent results on azimuthal anisotropy in heavy-ion collisions

Elliptic flow, as a fundamental observable, has been measured by many heavy-ion experiments over a wide range of energies, collision systems and collision centralities. The early measurements performed by fixed target and all four RHIC [8–11] heavy-ion experiments were recently complemented by Pb+Pb flow results from ALICE [43], ATLAS [44], and CMS [45] at the LHC, with collision energies $\sqrt{s_{NN}} = 2.76$ TeV, and $\sqrt{s_{NN}} = 5.02$ TeV, which is twenty fife times higher than the top RHIC Au+Au collision energy $\sqrt{s_{\mathrm{NN}}} = 200$ GeV. Figure 2.6 shows a compilation of an integrated v_2 in a wide range of the heavy-ion collision energy in the centrality interval 20–30% including the most recent LHC results. At energy lower than 4–5 GeV, v_2 shows non-monotonic behaviour due to shadowing by the spectators, whereas for higher collision energies a weak logarithmic growth of v_2 is observed. Based on the hydrodynamical model predictions [52, 53], the large values of v_2 measured at RHIC energies were interpreted as a signal of strongly coupled QGP and lead to an exciting conclusion that the medium behaves like an almost perfect fluid. The first flow results at the LHC energy were published by ALICE [43], ATLAS [44] and CMS [45] experiments, showing that the integrated elliptic flow of charged particles increased by about 30% compared to RHIC measurements in Au+Au collisions at $\sqrt{s_{NN}} = 0.2$ TeV. Nevertheless, measurements of the elliptic flow as a function of transverse momentum, p_{T}, revealed a very good agreement between RHIC and LHC results in the same centrality class. Figure 2.7 shows the comparison of $v_2(p_{\mathrm{T}})$ measured by ATLAS [44], ALICE [43], STAR [54] and PHENIX [55] in similar centrality class (40–50%) and mid-rapidity region ($|\eta| < 1.0$) for charged hadrons (except of PHENIX which measured elliptic flow for

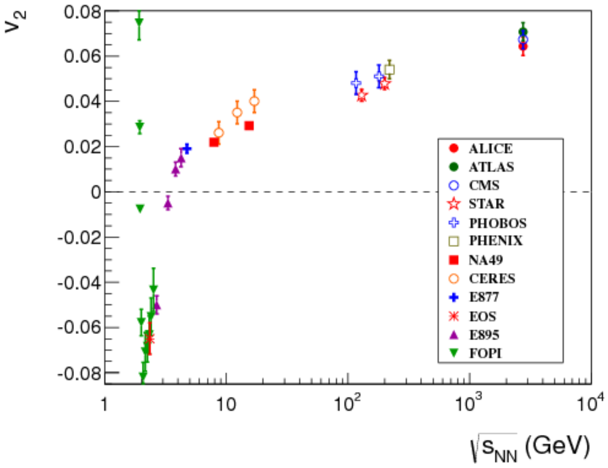

FIGURE 2.6: Integrated elliptic flow, v_2, as a function of the collision $\sqrt{s_{\mathrm{NN}}}$ energy for the 20–30% centrality interval [39].

π^0 mesons). The results showed that distribution of $v_2(p_{\mathrm{T}})$ has very similar behaviour in all experiments. First there is a rapid rise up to about p_{T} = 3 GeV and then the flow drops and becomes weakly dependent on p_{T} above 8–9 GeV. These observations imply that the QGP medium created in Pb+Pb collisions at the LHC resembles the perfect fluid already observed at RHIC energies.

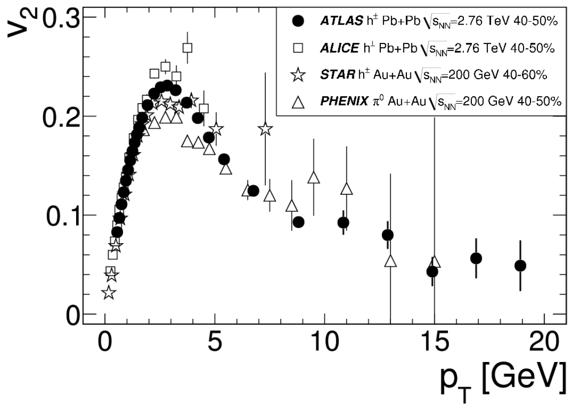

FIGURE 2.7: Elliptic flow, v_2, as a function of the transverse momentum, p_{T}, at $|\eta| < 1$ in the 40–50% centrality class [44].

During the first operational period at the LHC, in years 2010 and 2011, ATLAS collected a 8 μb^{-1} sample of Pb+Pb collisions at $\sqrt{s_{\mathrm{NN}}}$ = 2.76 TeV that allows for extensive studies of the elliptic flow and higher order Fourier coefficients, v_n. Measurements of flow were performed in broad transverse momentum, pseudorapidity and event centrality regions using the standard event-plane (EP) method [44], two-particle correlation function (2PC) [51] and multi-particle cumulants [56]. The second operational period of LHC data taking started in 2015, after the long upgrade shutdown, and its completion is scheduled at the end of 2018. In November and December 2015 the first heavy ion collisions with the increased collision energy of $\sqrt{s_{\mathrm{NN}}}$ = 5.02 TeV were performed at the LHC. The Pb+Pb collisions at the highest energy achieved in the laboratory provides a new opportunity to explore properties of the medium and test the validity of QGP hydrodynamic models.

Figure 2.8 presents the anisotropic flow harmonics dependence on centrality classes [51] for $n = 2$–6 measured in Pb+Pb collisions at $\sqrt{s_{\mathrm{NN}}} = 2.76$ TeV. As expected, the v_2 harmonic is the most significant, except for the most central events, where the v_3 is the largest. The elliptic flow increases as the centrality changes from most central (0%) to more peripheral events, reaching its maximum around 40−50% and then slightly decreases as expected from the centrality dependence of initial asymmetries. On the other hand, higher flow harmonics show very weak dependence on centrality.

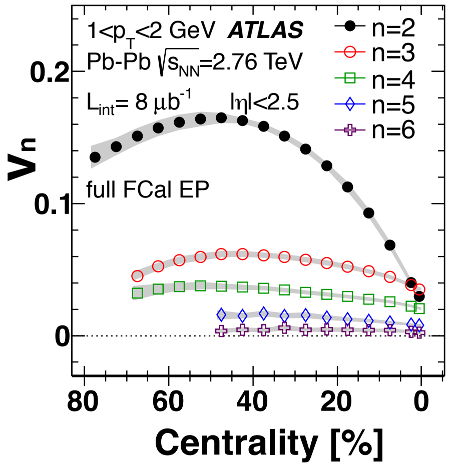

Figure 2.8: The v_n harmonics integrated over $1 < p_{\mathrm{T}} < 2$ GeV and $|\eta| < 2.5$ as a function of centrality in Pb+Pb collisions at $\sqrt{s_{\mathrm{NN}}} = 2.76$ TeV [51].

Figure 2.9 shows the ALICE experiment measurement of flow harmonics in Pb+Pb collisions at the $\sqrt{s_{\mathrm{NN}}} = 5.02$ TeV [57]. In the top panel the centrality dependence of v_2, v_3 and v_4 obtained with multi-particle correlations is presented. The results are compared to Pb+Pb collisions at $\sqrt{s_{\mathrm{NN}}} = 2.76$ TeV. Results on v_2 for 4-, 6-, 8-particle cumulants, agree within 1% which proofs that non-flow effects, i.e. correlation due to energy and momentum conservation, resonance decays, jet production, etc., are strongly suppressed, as was already seen in the measurements at the lower energy (e.g. [56]). The $v_2\{2, |\Delta\eta| > 1\}$ is higher than $v_2\{4, 6, 8\}$, which implies significant fluctuations in the initial geometry. The v_3 and v_4 harmonics, which reflect the initial energy-density fluctuations of the system, exhibit much weaker centrality dependence. The ratios of flow harmonics at $\sqrt{s_{\mathrm{NN}}} = 5.02$ TeV and $\sqrt{s_{\mathrm{NN}}} = 2.76$ TeV together with the hydrodynamical models calculations are shown in middle and bottom panels of Figure 2.9. The increase of v_n values in the centrality range 0–50% between two energies is at the level of 3.0 ± 0.6%, 4.3 ± 1.4% and 10.2 ± 3.8% for v_2, v_3 and v_4, respectively. The results are in good agreement with predictions. Figures 2.10 and 2.11 show examples of $v_n(p_{\mathrm{T}})$ and $v_n(\eta)$ dependence, respectively, in two centrality intervals 0–5% and 30–40% at the collision energy of $\sqrt{s_{\mathrm{NN}}} = 2.76$ TeV [51].

The CMS measurement of flow harmonics in a wide p_{T} range, up to 100 GeV, using the scalar product method and two- and multi-particle correlations are presented in Figure 2.12 [58]. It is expected that flow harmonics at high-p_{T} mirror the path-length dependence of parton energy loss in QGP. A smaller energy loss, or larger number of high-p_{T} particles produced, in-plane than out of the reaction plane direction is expected,

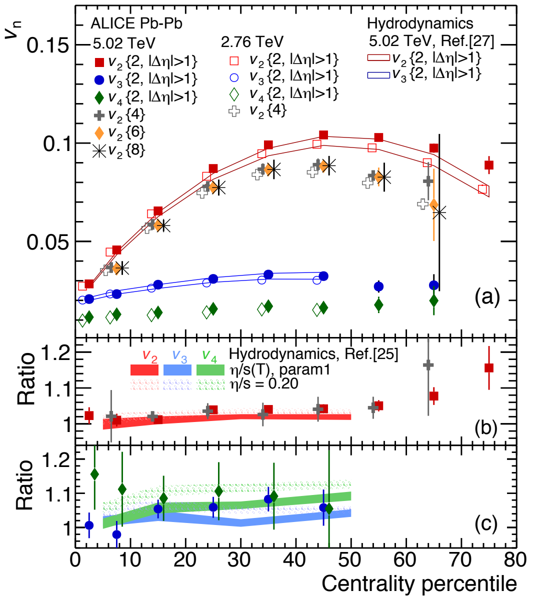

FIGURE 2.9: (a) Anisotropic flow v_n harmonics integrated over the p_T range of 0.2 < p_T < 5 GeV as a function of event centrality measured by ALICE with two- and multi-particle correlations in Pb+Pb collisions at $\sqrt{s_{NN}}$ = 5.02 TeV (solid points) and $\sqrt{s_{NN}}$ = 2.76 TeV (open points). (b and c) The ratios of $v_2\{2\}$, $v_2\{4\}$ and $v_3\{2\}$, $v_4\{2\}$ between measurements at 5.02 TeV and 2.76 TeV. Shaded bands corresponds to hydrodynamic calculations. Figure from [57].

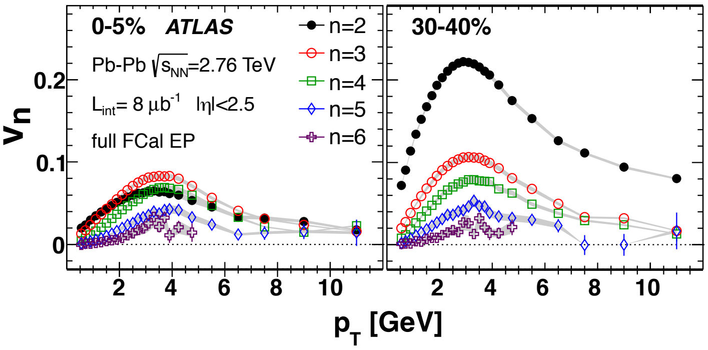

FIGURE 2.10: The v_n harmonics integrated over $|\eta|$ < 2.5 as a function of transverse momentum, p_T, for n=2–6 in two centrality classes: 0–5% (left) and 30–40% (right) at collision energy $\sqrt{s_{NN}}$ = 2.76 TeV [51].

resulting with non-zero values of flow harmonics. The v_2 and v_3 as a function of p_T obtained from the SP method are shown in Figure 2.12. The v_2 values are positive up to $p_T \sim$ 60–80 GeV, above which v_2 becomes consistent with zero. The v_3 remains positive up to $p_T \approx 20$ GeV over the 0–40% centrality range. CMS compared their results to the models: CUJET3.0 and SHEE, both valid for $p_T > 10$ GeV. The CUJET3.0 framework uses smooth hydrodynamic background, while the latter includes initial-state geometry fluctuations. Better agreement with the data is obtained for the SHEE model.

One of the most exciting results obtained at the LHC accelerator is the measurement of collective, flow-like phenomena in small systems, like *pp* [59, 61] or *p*+Pb

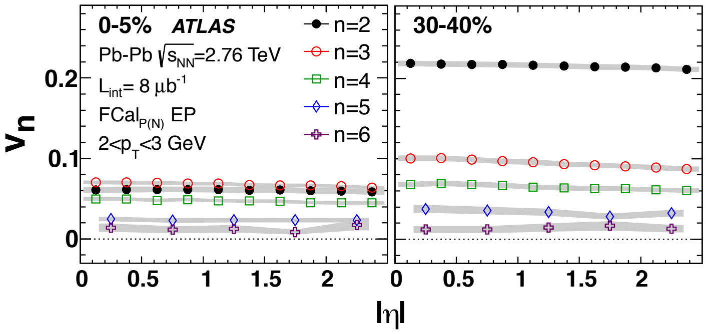

FIGURE 2.11: The v_n harmonics integrated over $2 < p_T < 3$ GeV as a function of pseudorapidity, $|\eta|$, for $n = 2$–6 in two centrality classes: 0–5% (left) and 30–40% (right) at collision energy $\sqrt{s_{NN}} = 2.76$ TeV [51].

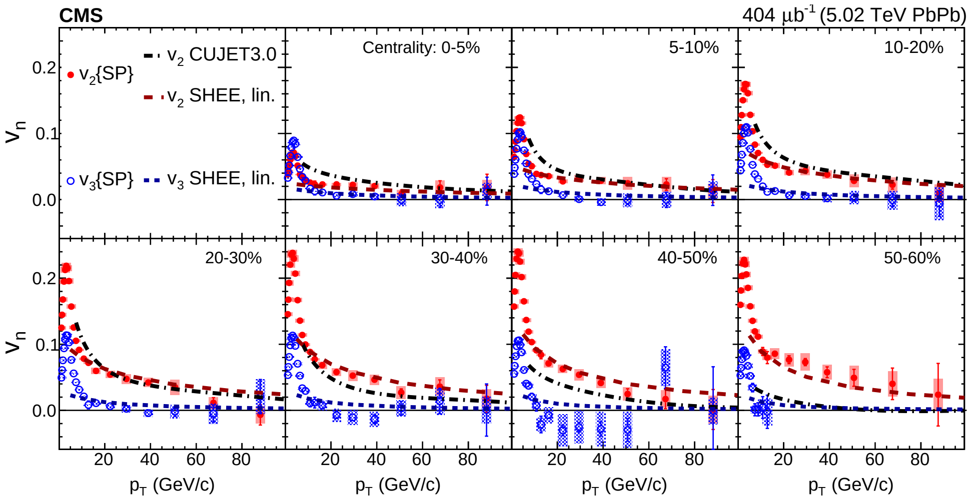

FIGURE 2.12: The v_2 and v_3 as a function of p_T obtained by CMS at $\sqrt{s_{NN}} = 5.02$ TeV with the SP method in seven centrality bins [58]. The dotted lines corresponds to the different models calculations.

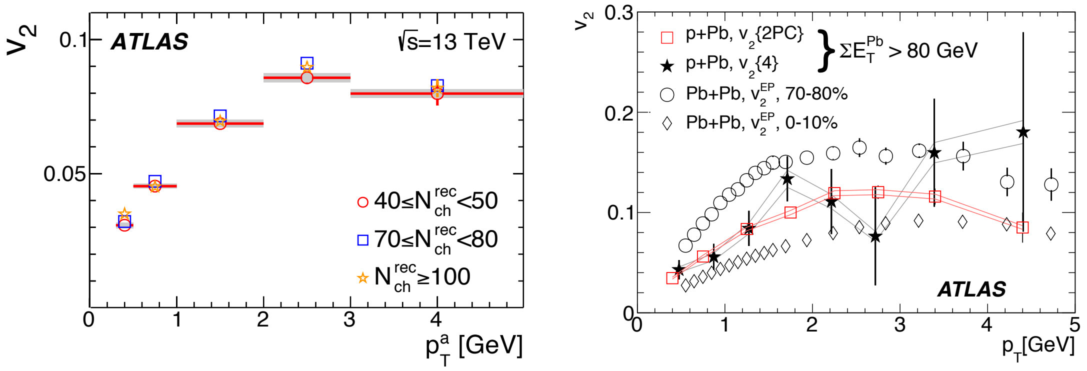

FIGURE 2.13: Left: The $v_2(p_T)$ measured in 13 TeV *pp* collisions for three N_{ch}^{rec} intervals [59]. Right: The $v_2(p_T)$ measured in 5.02 TeV *p*+Pb collisions with 2PC and 4-particle cumulant compared to the v_2 obtained with the EP method for central and peripheral Pb+Pb collisions [60]

collisions [62, 63]. The v_2 (p_T) measured in 13 TeV *pp* collisions with 2PC method for three charged-particle multiplicity, $N_\mathrm{ch}^\mathrm{rec}$, intervals is presented in the left panel of Figure 2.13 [59]. The right panel of Figure 2.13 shows the comparison of $v_2(p_\mathrm{T})$ measured in *p*+Pb collisions at $\sqrt{s_\mathrm{NN}}$ = 5.02 TeV with the 2PC and 4-particle cumulant methods to the $v_2(p_\mathrm{T})$ dependence observed in central and peripheral Pb+Pb collisions. The $v_2(p_\mathrm{T})$ dependence measured in both, *pp* and *p*+Pb, collision systems show similar trend to that observed in Pb+Pb collisions [60]. These results imply that the underlying physics in the small collision systems is the same or similar to the collective mechanisms observed in large collision systems. This unexpected discovery, although predicted in Ref. [65–67], leads to puzzling questions on possible origin of anisotropic flow, which cannot be explained by commonly used particle production models, including PYTHIA [68]. The study of collisions of other species which would “bridge” the small and large systems could provide better understanding of the underlying mechanism. The medium sized ions, such as Cu+Cu were collided at RHIC [69, 70] and recently in 2017 LHC performed Xe+Xe collisions at $\sqrt{s_\mathrm{NN}}$ = 5.44 TeV to bridge the gap between light and heavy collision systems. The results on v_2 in three example centrality intervals obtained by CMS [64] are shown in Figure 2.14. Elliptic flow was measured as a function of p_T using three techniques: SP, two- and multi-particle correlations. Similarly to the previous Pb+Pb results, the p_T-dependence shows common trend for each method: v_2 rises with the p_T reaching the maximum around 3−4 GeV and then gradually decreases.

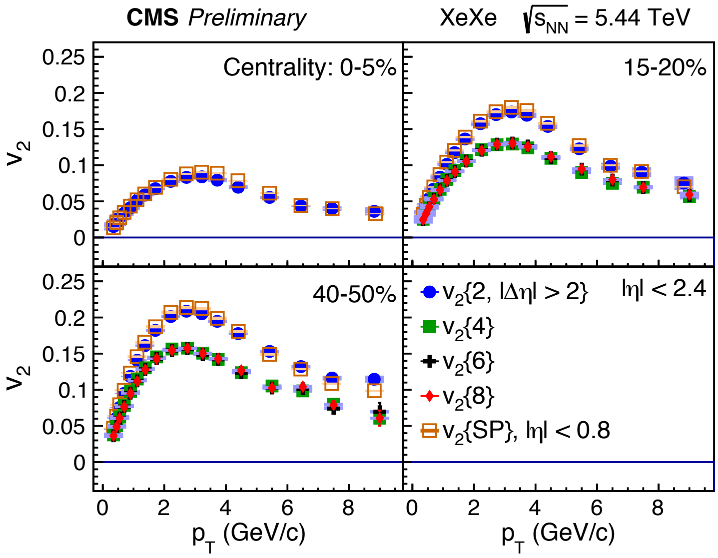

FIGURE 2.14: The v_2 as a function of p_T in three centrality intervals measured by CMS using SP, two- and multi-particle correlation methods in Xe+Xe collisions at $\sqrt{s_\mathrm{NN}}$ = 5.44 TeV [64].

Chapter 3

Experimental setup

3.1 The Large Hadron Collider

The LHC is installed in 27 km tunnel about 45−170 m below the surface, in a tunnel previously used for the Large Electron Positron Collider (LEP) machine. Two counter-circulating beams of protons or ions in the two LHC beam-pipes are lead to collisions in the four main interaction points (IP). Each IP is surrounded by a different LHC detectors: ATLAS, ALICE, CMS and LHCb.

The LHC accelerates and collides protons and ions since 2009. During RUN-1, the first physics operation period in 2010-2013, protons were collided at the centre of mass energy up to $\sqrt{s}$ = 8 TeV, Pb ions at the energy of $\sqrt{s_{\mathrm{NN}}}$ = 2.76 TeV and proton and

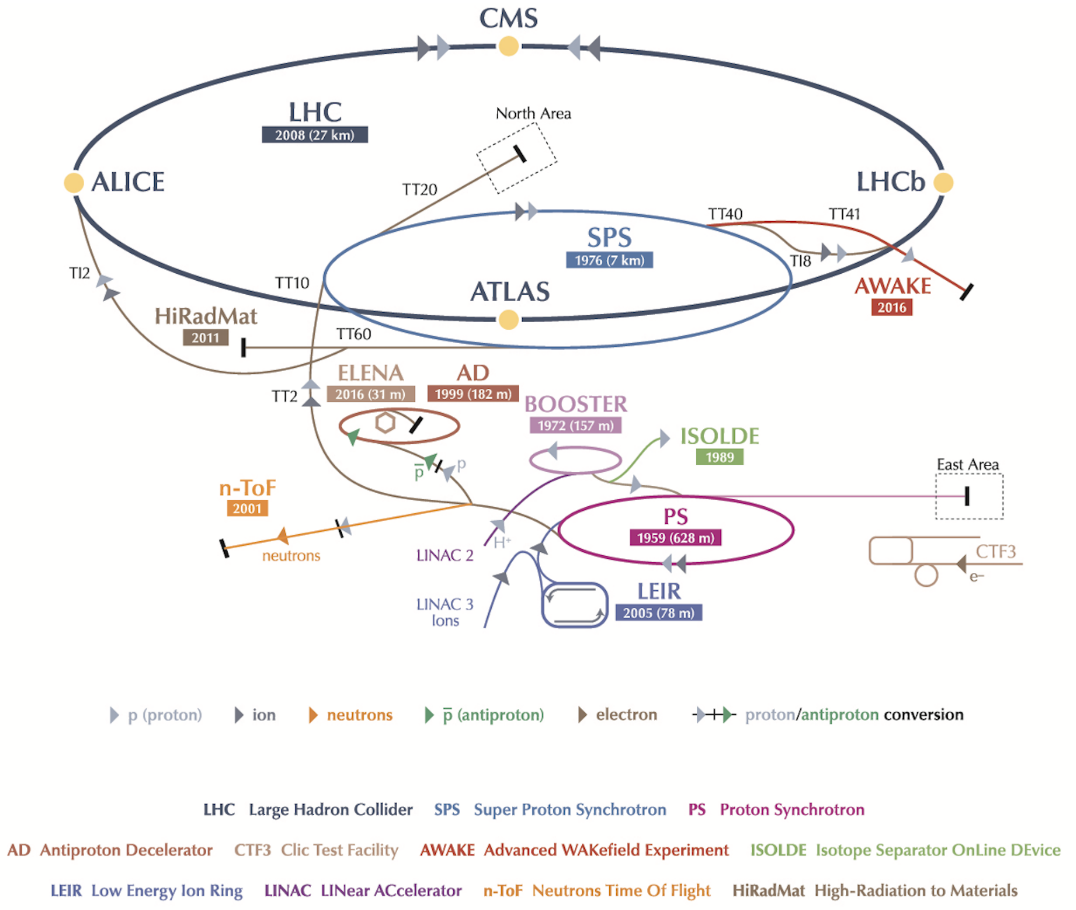

FIGURE 3.1: A sketch of CERN's accelerator complex including the LHC [71].

Pb ions at $\sqrt{s_{\mathrm{NN}}}$ = 5.02 TeV. Afterwards, in 2013-2015 the LHC was upgraded. The second operational period, RUN-2, started in 2015 and is currently ongoing (the end of the RUN-2 is scheduled for 2018). The protons are collided at $\sqrt{s}$ = 13 TeV, currently the maximal energy obtained in the laboratory. In November and December 2015 the first Pb+Pb collisions with higher collision energy of 5.02 TeVwere performed. Data collected during this period are used to obtain the main results presented here. On 12 October 2017 the LHC performed one-day run of xenon (Xe) collisions at the energy of $\sqrt{s_{\mathrm{NN}}}$ = 5.44 TeV. Results obtained with this data are also presented.

Figure 3.1 shows the CERN accelerator complex. The Pb (or Xe) ions go through several stages before being injected into the LHC ring. The energy is rumped up at each stage. The injection sequence for ions is as follows: LINAC3 (4.2 MeV/n) → LEIR (72 MeV/n) → PS (6 GeV/n) → SPS (177 GeV/n) → LHC (2.5 TeV/n).

The LHC collides particles not only with high energy but also with a high frequency. The nominal frequency for proton-proton collision is 40 MHz. Particles are organized into so-called bunches, which are collided every 25 ns. The LHC beam production is design to provide 2808 bunches per ring at maximum. Each bunch can be filled with about 10^{11} protons. The total number of events rate that can be observed per second in a detector, R, depends on the total cross section of a given process, σ_{tot}, and instantaneous *luminosity*, L:

$$R = L \times \sigma. \tag{3.1}$$

The luminosity is a function of the beam parameters. For Gaussian profile beams colliding head-on it can be expressed as [72]:

$$L = f \frac{N_1 N_2}{4\pi\sigma_x\sigma_y}, \tag{3.2}$$

where f is the bunches crossing frequency, N_1 and N_2 are the number of protons per crossing bunches, and σ_x, σ_y are related to the bunches dimensions in the x and y directions - $S_{eff} = 4\pi\sigma_x\sigma y$ is effective overlap area of the bunches. The total number of events produced in a given period of data taking is usually expressed by the production rate integrated over the time: $\sigma \times \mathcal{L}$, where $\mathcal{L} = \int Ldt$ is the integrated luminosity. The design instantaneous luminosity delivered during pp collisions at the LHC is L = 10^{34}cm^{-2}s^{-1}. In heavy ion collisions due to smaller number of ions per bunch and smaller number of bunches the design luminosity is of the order of L = 10^{27}cm^{-2}s^{-1}.

3.2 The ATLAS Detector

The measurements presented in this work where performed using the data collected by the ATLAS (A Toroidal LHC ApparatuS) detector [3]. The ATLAS reference system is a Cartesian right-handed co-ordinate system, with the nominal collision point at the origin. The anti-clockwise beam direction defines the positive z-axis, while the positive x-axis is defined as pointing from the collision point to the center of the LHC ring and the positive y-axis points upwards. The azimuth angle ϕ is measured around the beam axis, and the polar angle Φ is measured with respect to the z-axis. The pseudo-rapidity is defined as η = ln tan($\Phi/2$). ATLAS consists of several detecting systems arranged in barrel-shape layers with the interaction point (IP) in the middle. Figure 3.2 shows the main subsystems of the ATLAS detector along with the solenoid and toroid

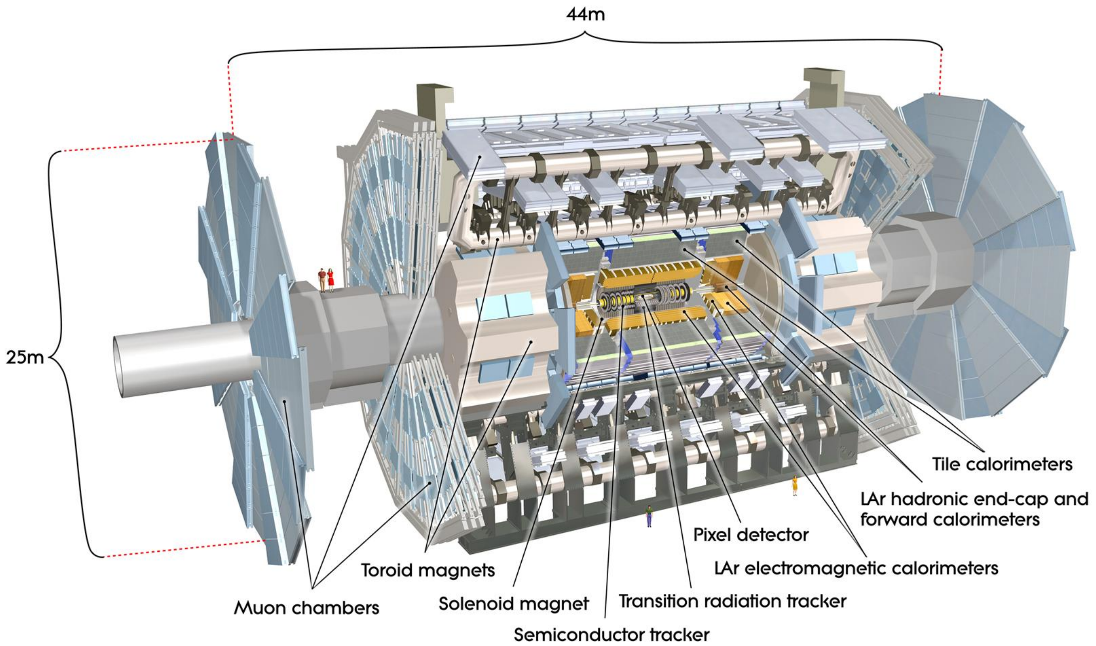

FIGURE 3.2: The schematic view of the ATLAS detector including its major sub-systems [3].

magnets. From the inside out the main systems are: the Pixel detector, semiconductor tracker and transition radiation tracker which constitute the ATLAS Inner Detector (ID). The ID, immersed in solenoidal field, provides charged particles tracking. The ATLAS calorimeter system includes the LAr electromagnetic calorimeters, the Tile calorimeters, the LAr hadronic end-cap and forward calorimeters (FCal). They are used to measure energies of electromagnetic and hadronic objects. The outermost part of the ATLAS detector is the Muon Spectrometer composed of the muon chambers and toroid magnets. The Muon spectrometer reconstructs muon trajectories and measures their momenta.

In the following subsections subsystems relevant for the presented study are briefly described. These are the ID and FCal together with the two detectors used for triggering on the minimum-bias events: Minimum Bias Trigger Scintillators (MBTS) and the Zero Degree Calorimeter (ZDC). For more details on the ATLAS experimental setup, see [3].

3.2.1 Inner Detector

The ATLAS ID provides efficient track reconstruction of particles produced in collisions. It is embedded in a 2 T magnetic field generated by superconducting solenoid magnet and occupies the barrel volume of 6.2 m long and diameter of 2.1 m closest to the IP. The ID consists of three subsystems: silicon pixel detectors (Pixel), semiconducor tracker (SCT) and a straw tube transition radiation tracker (TRT). Each of the subsystems is characterised by similar construction: parallel to the beam pipe the barrel modules are spread, they are closed by end-caps disks perpendicular to the beam axis. The Pixel and SCT are high-resolution tracking detectors designed to measure charged particle tracks in pseudorapidity range of $|\eta| < 2.5$. The TRT covers $|\eta| < 2$. Figure 3.3 shows a cut-away view of the ID including three sub-systems. A quarter cross-section of the ATLAS inner detector including the dimensions of each detector element is shown in Figure 3.4.

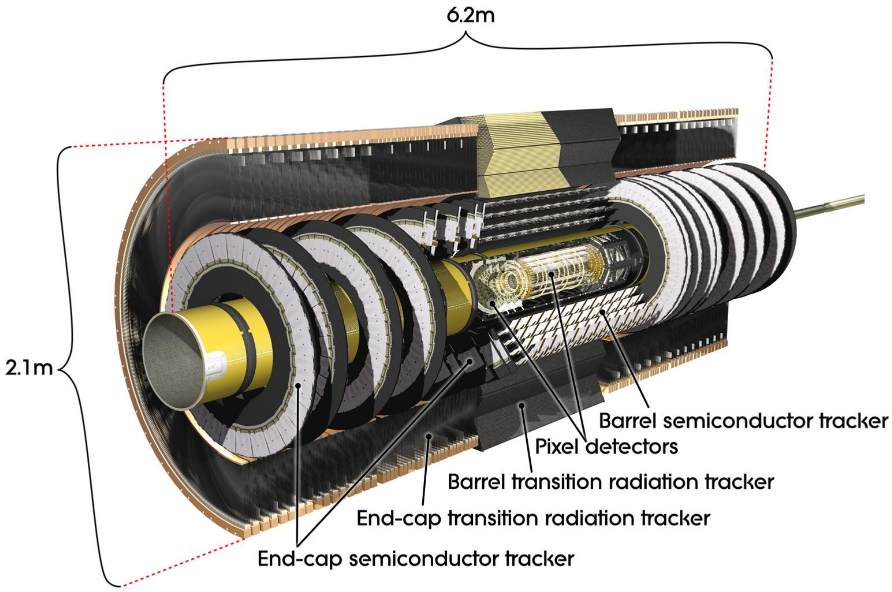

FIGURE 3.3: Cutaway view of the ATLAS ID [3].

Pixel detector

The Pixel is composed of three layers of sensors in the barrel and three layers on both sides of end-caps. During the LHC upgrade period between RUN-1 and RUN-2 one more innermost pixel layer, the insertable B-layer (IBL) [74], was added. The IBL layer was installed to improve track and vertex reconstruction in dense environments by providing additional measurement points closer to the IP. Moreover, the IBL has direct impact on the b-jet identification and significantly improves sensitivity of many analyses e.g. related to a *bottom - antibottom* quark pair in Higgs boson searches. Improvements in tracking and vertexing are particularly important in the b-jet identification All pixel layers were design to have extremely fine granularity to provide precise collision vertices location as well as the secondary vertexing. The IBL consist of 50×250 μm^2 sensors, while other pixel layers have pixel size of 50×400 μm^2. The built-in resolution of the pixel detector is 10 μm ($R-\phi$) and 115 μm (z) for the barrel region and 10 μm ($R-\phi$) and 115 μm (R) in the end-cap regions. In total, the pixel detector has approximately 92 M readout channels.

Semiconductor Tracker

The Pixel is surrounded by four SCT barrel strip layers and nine SCT end-cap disks perpendicular to the beam direction. The barrel region consists of stereo strips oriented with small-angle of 40 mrad to measure both coordinates, with one set of strips in each layer parallel to the beam direction to measure $R-\phi$. Barrel strips are double-sided and consist of two 6.4 cm long sensors. The end-cap disks are divided into a set of radially arranged strips together with a set of stereo strips at an angle of 40 mrad. Each sensor, both in the barrel and end-cap regions, has the mean pitch of approximately 80 μm. The intrinsic accuracy of the SCT modules is of 17 μm in the transverse direction in

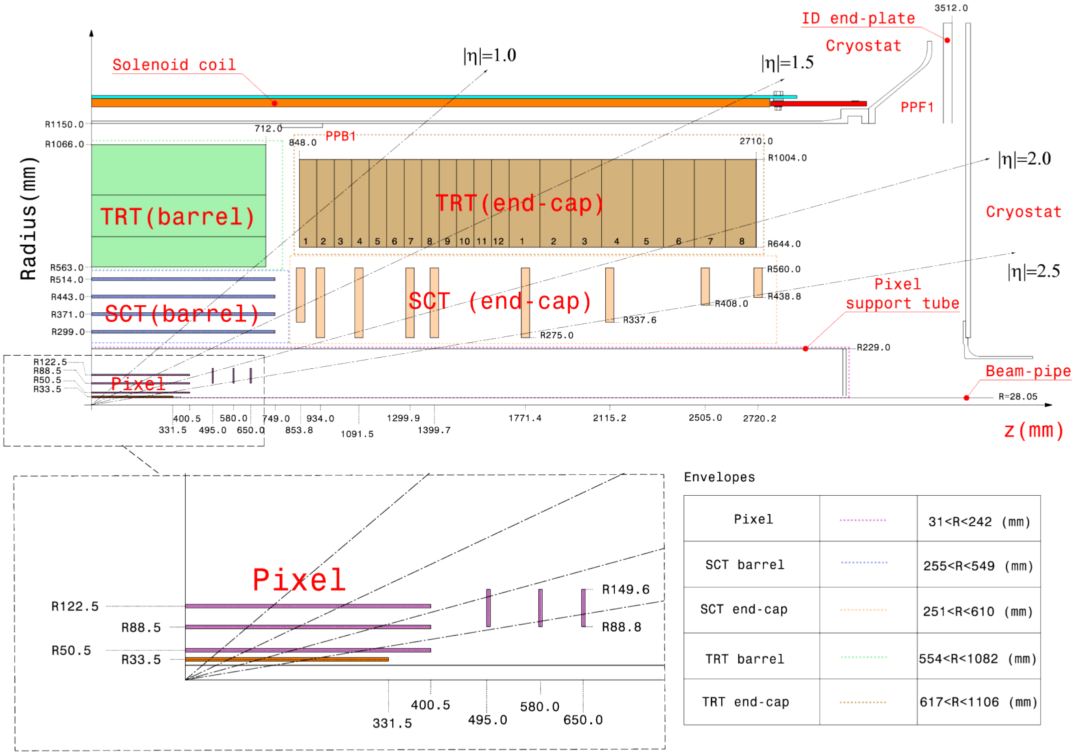

Pixel	⋯	31<R<242 (mm)
SCT barrel	⋯	255<R<549 (mm)
SCT end-cap	⋯	251<R<610 (mm)
TRT barrel	⋯	554<R<1082 (mm)
TRT end-cap	⋯	617<R<1106 (mm)

FIGURE 3.4: A quater-section view of the ATLAS ID [3, 73]. All the major systems are shown along with their dimensions. Dashed lines illustrate several examples of tracks at different η showing a typical detector elements they traverse.

the barrel and 580 μm in the longitudinal direction. The SCT has about 6.3 M readout channels in total.

Transition Radiation Tracker

The outermost layer of the ID is the TRT detector. The TRT allows for the discrimination between electrons and pions. The information from TRT is important component in the electron selection criteria in ATLAS. It consists of the 4 mm diameter and 144 cm long straw tubes parallel to the beam axis in its barrel part. The TRT end-cap region is composed of 37 cm long straws organised radially in the wheels. The straw tube elements are filled with a mixture of $Xe/CO_2/O_2$ gases. They are arranged alternately with transition radiation material. The TRT was design to provide only $R-\phi$ information with the intrinsic accuracy of 130 μm per straw. The total number of TRT readout channels is approximately 351 000. The TRT was not used in the heavy-ion running due to high hit occupancy in the most central events, which limited its use for tracking and electron identification. The analysis presented here does not benefit from the TRT hits information.

3.2.2 ATLAS calorimetry system

The ATLAS electromagnetic and hadronic calorimeter system is presented in Figure 3.5. It is positioned outside the ID and covers the range $|\eta| < 4.9$ with the transition region between $1.37 < \eta < 1.52$. It is composed of alternating layers of a dense absorber material that initiate the electromagnetic or hadronic particle shower and layers of an

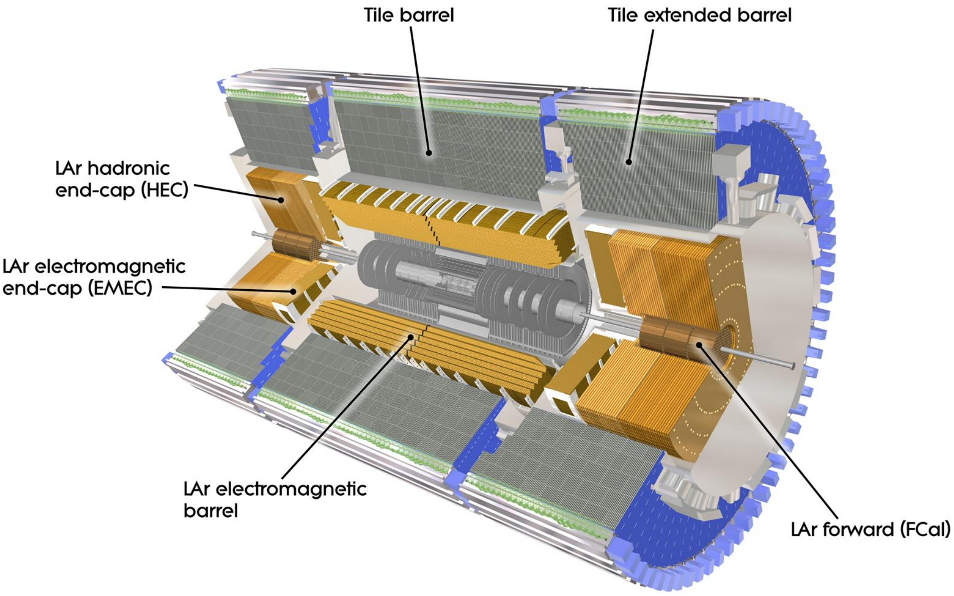

FIGURE 3.5: Profile of the ATLAS calorimeter system [3].

active material which is used to detect particle showers. It consists of an inner high granularity liquid-argon electromagnetic (LAr EM) calorimeter and hadronic sampling calorimeter.

The LAr electromagnetic calorimeter

The lead-LAr EM calorimeter is divided into a barrel ($|\eta| < 1.475$) and two end-caps components ($1.375 < |\eta| < 3.2$). It is composed of accordion-shaped kapton electrodes embedded in LAr and lead absorber plates. Such geometry provides complete ϕ symmetry without azimuthal cracks and fast signal extraction from the electrodes. The barrel part is composed of axial, accordion modules, which run in ϕ. The liquid-argon gaps are constant, which implies that the folding angles of modules vary with radius. The end-caps are divided into coaxial wheels and its accordion modules are arranged parallel to the radial direction.

Figure 3.6 shows the $\eta \times \phi$ segmentation of EM barrel layers at $\eta = 0$ as well as the accordion geometry of the EM calorimeters. Such segmentation is also valid for end-caps. The segmentation in $\eta \times \phi$ is always smaller than or equal to 0.1×0.1.

Forward calorimeters

The LAr Forward Calorimeter is formed of two end-caps placed 4.7 m away from IP. Each FCal end-cap consists of three modules: FCal1, FCal2 and FCal3, which together cover the pseudorapidity range of $3.1 < |\eta| < 4.9$. Left panel in Figure 3.7 shows the positions of the three FCal layers. The first layer is electromagnetic, while the other two are hadronic. The FCal consists of three layers of copper (FCal1) and tungsten (FCal2 and FCal3) absorbers with liquid argon as the active medium, which together provide 10 interaction lengths of material. The FCal1 module consists of copper plates arranged one behind the other with holes drilled in them through which electrodes are inserted. Electrodes are made of coaxial copper rods and copper tubes. Tubes and rods are separated by a plastic fibre wound around the rod. The arrangement of electrodes together with the Moliere radius for the FCal1 modules are shown in the right panel

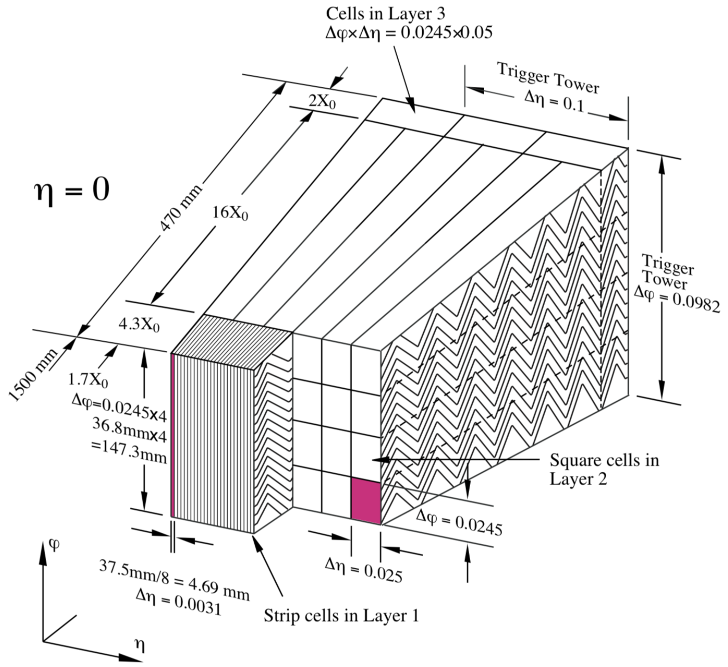

FIGURE 3.6: The $\eta \times \phi$ segmentation of EM barrel layers at $\eta = 0$ [3].

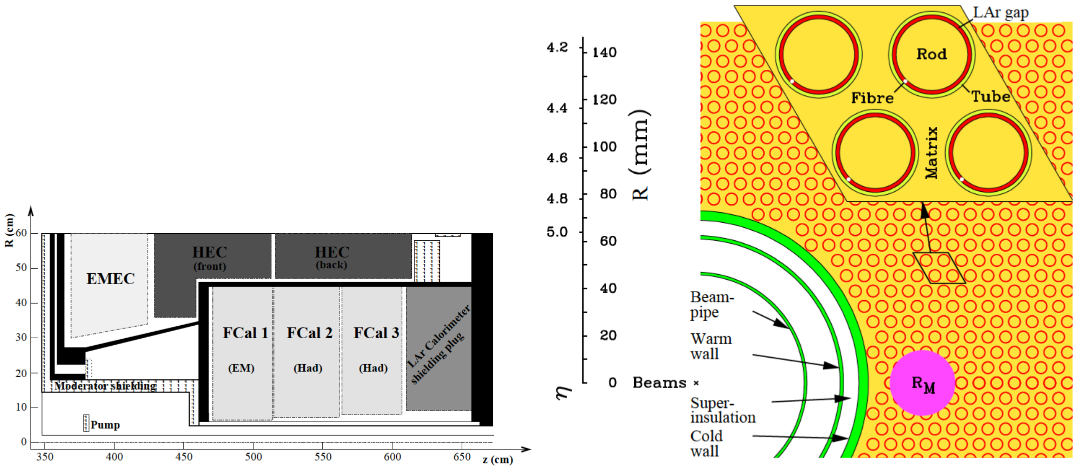

FIGURE 3.7: Left: The schematic view of the three FCal layers. Right: Schematic view on the cross-section of FCal1 electrodes.

of Figure 3.7. The structure of hadronic FCal2 and FCal3 modules is similar to the FCal1. Both consist of two copper end-plates with the electrodes arrangement as shown in right panel of Figure 3.7. The difference is in tungsten rods instead of copper rods. The amount of tungsten in these modules is maximised to provide a high absorption length. The FCal electrodes are positioned parallel to the beam-pipe in the x-y grid which is in contrast to $\Delta\eta - \Delta\phi$ segmentation of the electromagnetic calorimeter. The x-y segmentations (cells) are combined to form towers having segmentation in $\Delta\eta \times \Delta\phi$ of 0.1×0.1. In regions were the segmentation of calorimeter cells is larger than 0.1×0.1, the cell contributes to multiple towers with its energy divided between the towers.

3.2.3 Minimum bias trigger scintillators

The information provided by the MBTS detector is used for triggering minimum-bias events. The MBTS consists of two discs perpendicular to the beam pipe positioned at $z = \pm 3.56$ m in between of liquid-argon end-cap calorimeter cryostat covering the pseudorapidity range $2.08 < |\eta| < 3.86$. Each disc is composed of 12 scintillator counters segmented in 2 modules in η, which form an inner, $2.08 < |\eta| < 2.76$, and outer rings, $2.76 < |\eta| < 3.86$. Additionally, the inner pseudorapidity ring is divided into 8 modules in ϕ, each of $2\pi/8$ radians wide, while the outer ring has 4 azimuthal modules.

3.2.4 Zero Degree Calorimeter

The ZDC detector is located along the beam (i.e. at zero polar angle) on both sides of the ATLAS detector at a distance of ± 140 m from the ATLAS IP. At this point both LHC beams are deflected and separated into respective vacuum pipes so that the ZDC can detect forward neutral particles with $|\eta| > 8.3$. In heavy-ion collisions the ZDC measures spectator neutrons. The ZDC consists of four modules each of which is composed of 11 tungsten plates in the beam direction and quartz rods that run vertically between the plates as an active material.

3.2.5 Trigger system

The crucial component of each detector is the trigger system. The LHC bunch-crossing rates reaching up to 40 MHz would result in too many events to be recorded. The ATLAS trigger system reduces the recording rate to a few hundreds Hz by selecting only interesting events and rejecting the rest. The decision whether the event is accepted or not depends on characteristics of the event e.g. the presence of energetic electrons, muons, photons, jets etc. The strategy for identifying and reconstructing interesting events is different in each case and depends on what physics information is of interest.

The ATLAS trigger system has two levels: a hardware Level-1 and software-based High Level Trigger (HLT). The Regions-of-interest (RoIs) are determined at the Level-1 trigger utilizing the information collected from the full calorimeter and muon system including also MBTS and ZDC. The Level-1 trigger is divided into two components including Level-1 calorimeter (Level-1 Calo) and Level-1 muon (Level-1 Muon). The final Level-1 decision is formed by the Central Trigger Processor (CTP). It combines the information from all the Level-1 triggers and distribute signal to the sub-detector readout systems. The Level-1 trigger with the latency of 2.5 μs reduces the event rate from 40 MHz to 100 kHz. At this level, RoIs are geometrical regions within η and ϕ. The Level-1 RoIs information is sent further to be processed in the HLT. The HLT decision time, whether to accept or reject event, is about 300 ms. The HLT uses fast trigger reconstruction algorithms in the initial processing stage to be followed by analogous to those used in the offline reconstruction to diminish any possible inefficiencies. The HLT output rate is approximately 1 kHz.

ATLAS trigger system contains a variety of trigger items at L1 and HLT chains [3]. To tackle a huge data flow and a large variety of physics goals at the LHC, accepted events are recorded in so-called data streams. A stream is a collection of events with similar physics signatures selected by a group of closely related trigger chains e.g.

electrons, jets or minimum-bias triggers. Furthermore, the event-rate of a particular trigger item (at L1 or HLT) can be reduced by applying prescale factors. The prescale procedure allow to reject a fraction of events that would be otherwise selected by that trigger. For example a prescale factor of 5 applied on L1 trigger item implies that every 5-th event accepted by this trigger is passed to HLT.

Recorded events are collected in groups and marked with the unique numbering scheme. The individual number assigned to each event is so-called Event Number, while the number for group of events is known as Run Number. The Run Number represents the continuous period of data taking, typically lasting a few hours, which is additionally divided into luminosity blocks, usually lasting one/two minutes. The data and detector state examined each luminosity block to confirm its utility before it is used in analyses. A block that passes the qualitative criteria is classified as "good". A list of "good" runs, so-called Good Run List (GRL) is the starting point of every physics analysis.

Data successfully selected by the trigger are aggregated and stored for further processing in the form of raw information (byte-streams). The RAW files are reconstructed using a dedicated software to translate the bits and bytes to useful information about the events. The output from the data reconstruction step that allows to read the data is analysis object data (AOD). The primary physics AOD file contains a full information about reconstructed event, suitable for use in analysis. Most analyses need only a fraction of data related for specific studies. Thus, to facilitate analysis, the size of AOD files is reduced by removing events, object within events or variables within objects that are not required for given analysis. Such derived AODs (DAODs) are sent to the Worldwide LHC Computing Grid, which integrates computing centres worldwide and provides computing and storage resources.

Chapter 4

The dataset description

4.1 Event selections

The analysis uses the data sample of Pb+Pb collisions at the $\sqrt{s_{NN}} = 5.02$ TeV. The Pb+Pb run was very successful in providing large sample of events. The Pb+Pb collision data recorded in November and December 2015 by the ATLAS experiment correspond to the total luminosity of 0.49 nb^{-1}. The flow study presented in this thesis is based on the reconstructed charged particles derived from minimum-bias (MinBias) data stream including 32 Pb+Pb good runs. This sample consists of about 274 M of minimum-bias events. The collected data sample was carefully inspected by data quality groups of each ATLAS detector sub-system and the Pb+Pb GRL, consisting runs and lumi-blocks when all sub-detectors function optimally, was created. The number of events that passed the quality selections required for the GRL is approximately 264 M.

Bulk of events are selected in trigger system by a combination of two mutually exclusive minimum-bias trigger chains which sample:

- peripheral events; by requiring the total transverse energy measured in calorimeters to be less 50 GeV, one neutron on each side of the ZDC and at least one charge particle track at the HLT level.
- central and semi-central collisions; by requiring the total transverse energy measured in calorimeters to be greater than 50 GeV.

The minimum-bias triggers sample represents the luminosity of 22 μb^{-1}. Moreover, the analysis is enhanced by the ultra-central, 1% and 0.1%, collisions recorded by two dedicated triggers: UCC-1 and UCC-2, respecively. The ultra-central triggers select events in which the total transverse energy measured in FCal at L1 was more than 4.21 TeV and 4.54 TeV for UCC-1 and UCC-2, respectively. The luminosity sampled by the UCC-1 trigger is 45 μb^{-1}, while UCC-2 trigger sampled 0.49 nb^{-1}. Table 4.1 summarises the luminosities sampled by the triggers used in the analysis.

Trigger	sampled lumionosity	events
Minimum-bias	22 μb^{-1}	~ 130 M
UCC-1	45 μb^{-1}	~ 3 M
UCC-2	0.49 nb^{-1}	~ 3.5 M

TABLE 4.1: The luminosities and number of events sampled by the triggers used in the analysis.

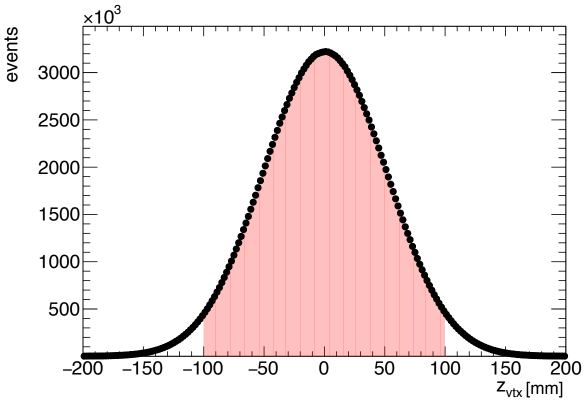

FIGURE 4.1: The distribution of the z coordinate of the primary vertex for Pb+Pb collisions $\sqrt{s_{\mathrm{NN}}} = 5.02$ TeV. Shaded area indicates the cut $|z_{vtx}| < 100$ mm.

selection criterion	number of events [M]	percentage [%]
All	273.94	100%
GRL	265.59	96.95%
MB + UCC triggers	211.36	77.16%
Primary vtx	204.69	74.72%
vtx with $\lvert z\rvert < 100$mm	195.30	71.30%
pileup	194.65	71.06%
80% of most central events	136.28	49.75%

TABLE 4.2: Number of events surviving successive selection requirements.

In addition to the trigger selection, events are also required to have a good-quality reconstructed primary vertex. Events with none or multiple reconstructed vertices are rejected from analysis. Moreover, the z coordinate of the vertex is required to be within $|z_{vtx}| < 100$ mm. Such selection removes events near the edge of the detector which might have issues with tracking. The distribution of z_{vtx} before and after the aforementioned selection is shown in Figure 4.1.

The GRL requirement removes the detector problems that affect entire luminosity block (i.e. 1−2 minutes of data taking). One luminosity block can represent even a thousands of events. Single or some portion of events inside one luminosity block can be affected by localised detector problems. For that reason, to avoid cutting out the whole block of events there are also additional event-level detector flags implemented to reject “bad” events. In presented analysis following event-cleaning criteria to remove problematic events are imposed:

(a) due to the LAr system

(b) due to the Tile Calorimeter

(c) due to the SCT inner detector system

(d) due to incomplete events (event key information missing)

Table 4.2 summarises the number of events on each selection step. The two last selection criteria included in the table are described in the next subsections.

4.2 Pileup removal

In the Pb+Pb run in 2015 the probability to produce a pileup event, i.e. register an event containing more than one Pb+Pb collision per bunch crossing, was reaching a value of ~0.002. Therefore the expected influence of the multiple events on analyses is considered to be negligible with the min-bias sample. Events with pileup can be distinguished using two complementary methods.

The first method uses the correlation between signals detected in the ZDC and FCal. The signal in the ZDC is calibrated to the number of detected neutrons based on the location of the peak corresponding to a single neutron. The correlation between number of neutrons in the ZDC and the total transverse energy E_{T} in the FCal has characteristic "banana" shape [75–77] as presented in the example Figure 4.2 obtained by ALICE experiment. Events outside the correlation pattern are considered as pileup events. Figure 4.3 (left panel) shows the correlation of the count of tracks and energy in the FCal.

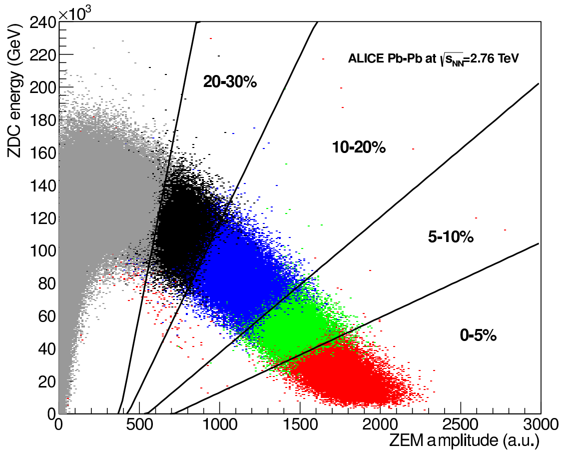

FIGURE 4.2: Spectator energy deposited in the ZDC calorimeters measured by ALICE experiment at $\sqrt{s_{\mathrm{NN}}} = 2.76$ TeV Pb+Pb collisions as a function of small electromagnetic calorimeters (ZEM) amplitude [75].

The former, due to the setup of the track reconstruction for HI environment is always constrained to a single vertex, while the energy in the FCal contains contributions from all concurrent collisions. Events with multiple collision are the ones below the main correlation trend and can be clearly seen in this figures. Middle panel of Figure 4.3 shows events after applying pileup rejection using the first method. As some small, remaining fraction of pileup events is still present outside of the main correlation shape, the second method is introduced: events below the red line ($N_{\mathrm{ch}}^{\mathrm{rec}} = 629.848 \Sigma E_{\mathrm{T}}^{\mathrm{FCal}}$ - 151.764) and above the magenta line ($N_{\mathrm{ch}}^{\mathrm{rec}} = 792.511 \Sigma E_{\mathrm{T}}^{\mathrm{FCal}} + 205.818$) shown in middle panel of Figure 4.3 were removed. The final FCal-$\mathrm{N}_{\mathrm{ch}}^{\mathrm{rec}}$ correlation after applying all selection cuts is shown in right panel of Figure 4.3.

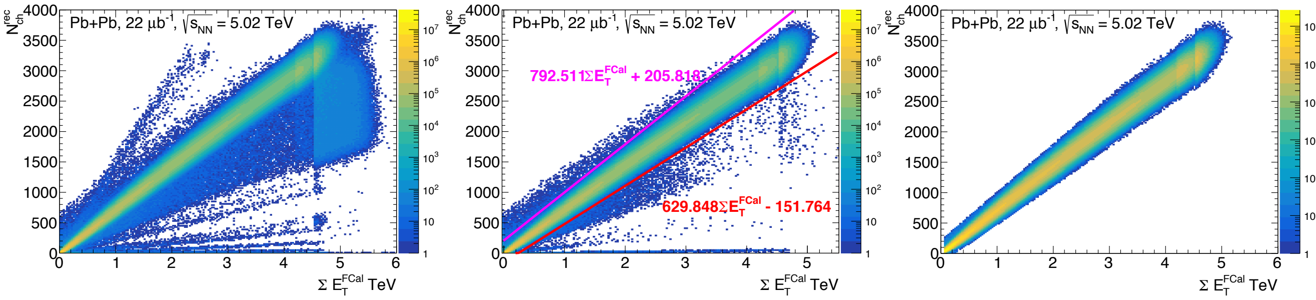

FIGURE 4.3: Left: Correlation between the number of reconstructed charged particles, $N_{\text{ch}}^{\text{rec}}$, and the total transverse energy measured in FCal, $\Sigma E_{\text{T}}^{\text{FCal}}$, after the event selection. Middle: Correlation after applying the pileup rejection tool together with additional cuts to remove pileup leftovers. Right: Final $N_{\text{ch}}^{\text{rec}}$ vs. $\Sigma E_{\text{T}}^{\text{FCal}}$ correlation.

4.3 Centrality determination

The lead ions, accelerated at the LHC, have significant dimensions and their collision can not be treated like a collision of two point-like particles. Two ions can collide head-on with all their constituent nucleons participating in the collision or the ions could barely scratch each other with the edges so only few nucleons interact. The impact parameter b, defined as the distance between centers of two nuclei in the transverse plane perpendicular to the beam axis, changes in this two extreme cases from 0 in central, head-on collisions to about 20 fm in peripheral collisions. Centrality can also be expressed in terms of the total number of binary nucleon-nucleon collisions, N_{coll}, and the number of nucleons participating in the collision, N_{part}. The impact parameter, N_{coll} and N_{part} can not be measured directly but they can be calculated with the Monte Carlo Glauber model [37] based on various observables that exhibit a monotonic relationship with them. Figure 4.4 shows an illustrative relationship between the b, the N_{part} and

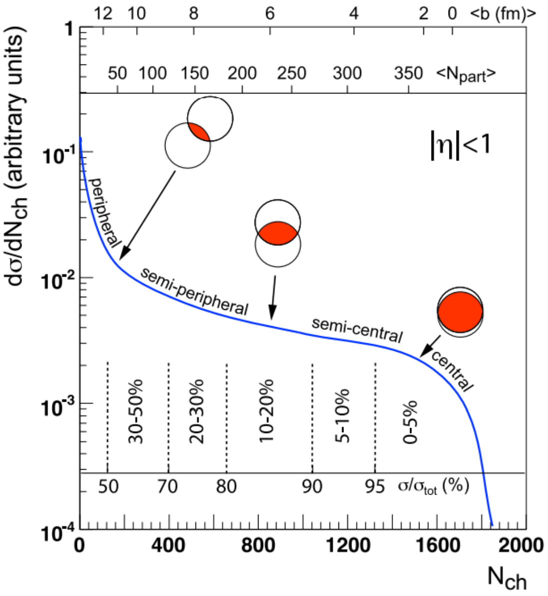

FIGURE 4.4: Illustration of the relationship of the final state event multiplicity, N_{ch}, with Glauber calculated quantities - b and N_{part} [38].

Centrality [%]	$\langle N_{\text{part}}\rangle$	f = 84.5% $\Sigma E_{\text{T}}^{FCal}$ [TeV]	f = 83.5% $\Sigma E_{\text{T}}^{FCal}$ [TeV]	f = 85.5% $\Sigma E_{\text{T}}^{FCal}$ [TeV]
0 - 0.1	406.62	4.54199	4.54094	4.54291
0 - 1	402.93	4.26258	4.26017	4.2649
0 - 5	384.49	3.61844	3.60999	3.62674
5 - 10	333.11	2.98931	2.9759	3.00247
10 - 20	264.08	2.04651	2.0277	2.06495
20 - 30	189.22	1.36875	1.34812	1.38892
30 - 40	131.43	0.87541	0.855791	0.894902
40 - 50	87.019	0.525092	0.508105	0.542107
50 - 60	53.94	0.289595	0.276461	0.302826
60 - 70	30.57	0.14414	0.135286	0.15318
70 - 80	15.41	0.063719	0.058527	0.069136

TABLE 4.3: Centrality classes used in the analysis defined with $\Sigma E_{\text{T}}^{FCal}$ for the nominal sampling fraction. The $\Sigma E_{\text{T}}^{FCal}$ thresholds for the two systematic sampling fractions (83.5% and 85.5%) are also listed. $\langle N_{\text{part}}\rangle$ is the mean number of nucleons participating in the collision.

N_{ch}. Events with large overlap between colliding nuclei, i.e. events with small b and thus, large N_{part} are called central collisions. On the other hand, events with large b and small N_{part} are called peripheral collisions. Commonly, heavy-ion experiments express the event centrality via percentile classes, which are evaluated using multiplicity or transverse energy measured in a specific sub-detector.

In ATLAS, for the centrality determination, the transverse energy deposited in the FCal ($\Sigma E_{\text{T}}^{FCal}$) was chosen[1]. The centrality is defined as percentile of the minimum-bias $\Sigma E_{\text{T}}^{FCal}$ distribution, e.g. 0-10% indicate the 10% of events with highest deposit. The main idea is that 10% of events with the highest measured $\Sigma E_{\text{T}}^{FCal}$ approximately corresponds to the 10% of the events with the lowest values of b or the highest N_{part} (N_{coll}) numbers [44]. The minimum-bias triggers aim to sample significant fraction of the total non-Coulomb cross section in collision data. The fraction, called "sampling fraction", is f =100% when 100% of non-Coulomb events (referred to as minimum-bias events) are collected. Nevertheless, it could happen that f <100% in case of inefficient event selection or f >100% when the data sample is contaminated with Coulomb and/or noise events. In order to extract the mapping from the observed $\Sigma E_{\text{T}}^{FCal}$ to the basic features for each centrality class, such as N_{coll} or N_{part}, a model based on the Monte Carlo Glauber [38, 78] approach is used. The Glauber model provides a description of a correlation between the $\Sigma E_{\text{T}}^{FCal}$ distribution and the sampling fraction of the total inelastic Pb+Pb cross section, allowing to assign the centrality percentiles.

For 2015 Pb+Pb data a dedicated analysis of centrality determination in ATLAS was carried out. In the analysis the Glauber simulation was matched to the Pb+Pb data in the region above $\Sigma E_{\text{T}}^{FCal}$ > 40 GeV to select non-Coulomb sample and avoid anticipated difficulties with selecting very peripheral collisions. With such selection the sampling fraction was estimated to be f = 84.5±1%. The base measurements in the presented analysis are performed assuming f = 84.5%, while measurements

---

[1] The centrality determination is not a part of this thesis - only the description is provided. The values are directly used in the presented analysis.

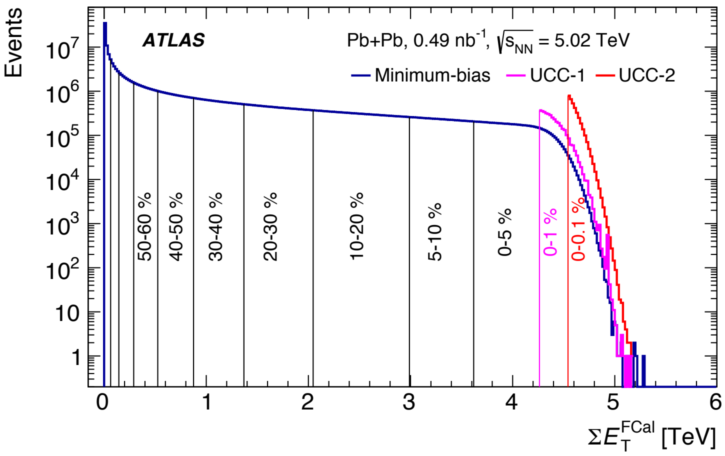

FIGURE 4.5: The FCal $\sum E_T$ distribution from Pb+Pb data at $\sqrt{s_{NN}}$ = 5.02 TeV. Vertical lines indicate centrality cuts.

with f = 83.5% and f = 85.5%, that covering uncertainties of the fast simulation, are considered as a part of the systematic studies. Analyses in HI are conventionally performed in bins of centrality. In this analysis, the v_n harmonics are determined in 9 centrality classes of the minimum-bias sample: 0-5%, 5-10%, 10-20%, ..., and 70-80%. Moreover, two ultra-central bins: 0-0.1% and 0-1%, are also considered, which give 11 centrality intervals in total. Table 4.3 summarises the nominal (based on f = 84.5%) and systematics (based on f = 83.5% and f = 85.5%) centrality classes used in the analysis defined by ΣE_T^{FCal}. The mean number of nucleons participating in the collision, $\langle N_{\text{part}} \rangle$, is also provided. The ΣE_T^{FCal} distribution in the data including the default thresholds for the several centrality classes is shown in Figure 4.5. To avoid any biases from diffraction or other processes that may contribute to very peripheral collisions (centrality class 80 - 100%) the presented work exploits a selection of the 80% most central collisions (i.e. centrality 0 - 80%).

4.4 Track quality selections

Flow measurement presented in this work is based on charged tracks detected in ATLAS ID and reconstructed by the ATLAS track reconstruction algorithms optimised for HI conditions i.e. high tracks density. Each reconstructed track is required to pass additional topological and geometrical selection criteria. There are three sets of track quality selections used in the analysis presented in Table 4.4. The default is named as *HITight*. For systematic studies, discussed latter, two sets of cuts are studied: *HILoose* and *HITight+* which affect the quality of tracks needed in the analysis as compared to the default selection. By varying tracking cuts the balance between the real and fake tracks can be modified in the sample. Real tracks correspond to the good reconstructed track that come from the real charged particle, while fake tracks are due to random combinations of hits in Pixel and SCT detectors. All aforementioned track quality selections require tracks with track $|\eta| < 2.5$ and track $p_T > 0.5$ GeV. Additionally, a requirement of an IBL hit if expected on a track trajectory or if not expected then hit in the next layer is also common for the three selections. A hit is expected if the extrapolated track crosses an active region of a pixel module that has not been disabled, and a hit is said to be missing when it is expected but not found. Table 4.4 lists remaining track selection criteria that differ between *HITight*, *HILoose* and *HITight+*. The d_0 impact parameter is the distance of the reconstructed track from the primary vertex projected to the transverse plane. The z_0 impact parameter is defined as "z" of the point on track which determines the d_0. The $\chi^2/ndof$ is η dependent cut on the track fit quality.

track selection criteria	*HITight*	*HILoose*	*HITight+*
number of Pixel hits	≥ 2	≥ 1	≥ 2
number of SCT hits	≥ 8	≥ 6	≥ 8
maximum number of SCT holes	1	-	1
$\lvert d_0 \rvert$	< 1 mm	< 1.5 mm	<0.5 mm
$\lvert z_0 \sin\theta \rvert$	< 1mm	< 1.5 mm	< 0.5 mm
$\chi^2/ndof$	< 6	-	< 6

TABLE 4.4: Differences between track quality selections used as default: *HITight*, and for systematic studies: *HILoose* and *HITight+*.

4.5 Monte Carlo simulations

In experimental practice of studying particle collisions, it is necessary to work with Monte-Carlo (MC) simulations. In this case simulations allow for a thorough examination of processes occurring in the detector and also allow for evaluation of the reconstruction algorithms performance for specific physical quantities or the properties of a collision.

In the presented analysis the Heavy Ion Jet INteraction Generator, HIJING [79] model has been used to generate Pb+Pb collision events. All generated events have been processed through a full GEANT4 [80] simulation of the detector response. The simulated events are reconstructed using identical algorithms as used for data. The HIJING model was developed to study particle production in high-energy *pp*, *p*+A and A+A collisions. It is based on a perturbative QCD description of multiple mini-jet production in hard parton scattering processes. For soft processes, with small transverse momentum transfers (below 2 GeV), a string description of soft-gluon exchanges between valence quarks or di-quarks is adopted. The Lund JETSET fragmentation scheme is used for jet and string hadronization. A nucleus-nucleus collision is decomposed into a sequence of binary collisions involving participant and excited nucleons. The Glauber model is used to describe the collision geometry and to compute the number of binary collisions and the number of participant nucleons. Additional nuclear effects are also incorporated, including nuclear shadowing and final-state energy loss (jet quenching). Nuclear shadowing is the suppression of the effective number of partons at low values of x, leading to a decrease in the multiplicity of produced particles. This is implemented by suitable parameterisations of the quark and gluon structure functions in the small and medium x region. Jet quenching occurs via gluon radiation with an assumed average energy loss of partons traversing the dense medium. In HIJING, the process of energy loss is stopped when p_{T} of a parton falls below 2 GeV. For the studies presented in this thesis HIJING does not contain jet quenching.

The MC study is based on the fully simulated samples of Pb+Pb collisions at $\sqrt{s_{\mathrm{NN}}}$ = 5.02 TeV. Simulations of complex and large heavy-ion events, including detailed detector response, are CPU time consuming. To save the CPU time, the MC sample used in the presented analysis was produced with a simplified and fast simulation of ATLAS calorimeter response, which is a novel approach in ATLAS heavy-ion studies. The simulation architecture is designed to make simulation algorithms as fast as possible. The model is organised so that the ID and muon system are fully simulated with GEANT 4, while calorimeter is simulated using a dedicated program *FastCaloSim* [81, 82]. The FastCaloSim is based on a simplified detector geometry and replaces simulation of particle showers and the energy distribution in calorimeter by parametrisation. The parametrisation model uses only three particle types: electrons, photons and charged pions. The latter is used for parametrising all hadrons (neutral and charged). The FastCaloSim package reproduces the longitudinal shower properties, including fluctuations and correlations, but assuming only the average transverse shower information. The fast simulation approach significantly reduced the simulation time and allowed to produce relatively large (as for heavy-ion standards) sample of approximately 4M Pb+Pb Hijing events, which is used in the analysis.

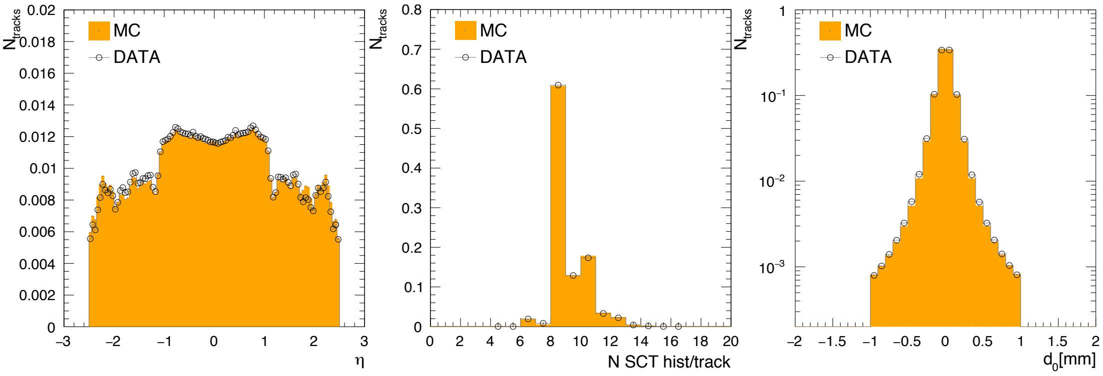

FIGURE 4.6: Comparison of selected track quantities in Pb+Pb collisions at $\sqrt{s_{\mathrm{NN}}}$ = 5.02 TeV and MC simulations. From the left are shown: distribution of number of reconstructed tracks as a function of η, the distribution of the number of hits in silicon detectors per track and the impact parameter d_0 distribution.

The elementary tracking quantities such as η, number of hits in silicon detectors and d_0 impact parameter distributions are shown in Figure 4.6. They are compared between the MC and the data to validate the produced MC sample. Overall there is a good agreement between the MC and data distributions.

4.6 Track reconstruction efficiency and fake rates

The MC sample is used to determine the track-reconstruction efficiency as well as fake track rates. Both efficiency and fake rates are established as a functions of p_{T}, η and event centrality. MC events are categorised into centrality intervals by matching the MC data event multiplicity distributions in each centrality class.

4.6.1 Efficiency

The efficiency, $\epsilon(p_{\mathrm{T}}, \eta)$, is defined as:

$$\epsilon(p_{\mathrm{T}}, \eta) = \frac{N_{ch}|match\ to\ reco}{N_{ch}}, \tag{4.1}$$

where the N_{ch} is the number of primary [83] charged particles and in the numerator is the number of them having reconstructed counterpart. The matching criterion is based on so called match probability which is defined as the ratio of number hits common to the generated particle and the reconstructed track for Pixel and SCT detectors to the number of hits which form the track. Number of hits in each detector is weighted. The weights are 10 for Pixel, 5 for SCT. In this analysis the weighted fraction of detector hits shared between the track and generated, charged particle trajectory is required to be more than 30%. The efficiency is shown in Figure 4.7 as a function of each p_{T}, η and centrality, with the other two variables constrained to a narrow range. The efficiency varies most at low p_{T} region where a significant changes can be seen as a function of η and centrality. For events with centrality < 5% at mid-rapidity ($|\eta| < 1$) the reconstruction efficiency varies from ~60% at low p_{T} = 0.5−0.7 GeV to ~75% at high $p_{\mathrm{T}} > 5$ GeV. At rapidities of $|\eta| > 1$ the efficiency decreases to ~40−60% depending on p_{T} and centrality. The strongest centrality dependence is observed for low-p_{T} tracks. The difference between efficiencies for the most central and peripheral events is about 5%. For higher-p_{T}, this difference is less than 1%.

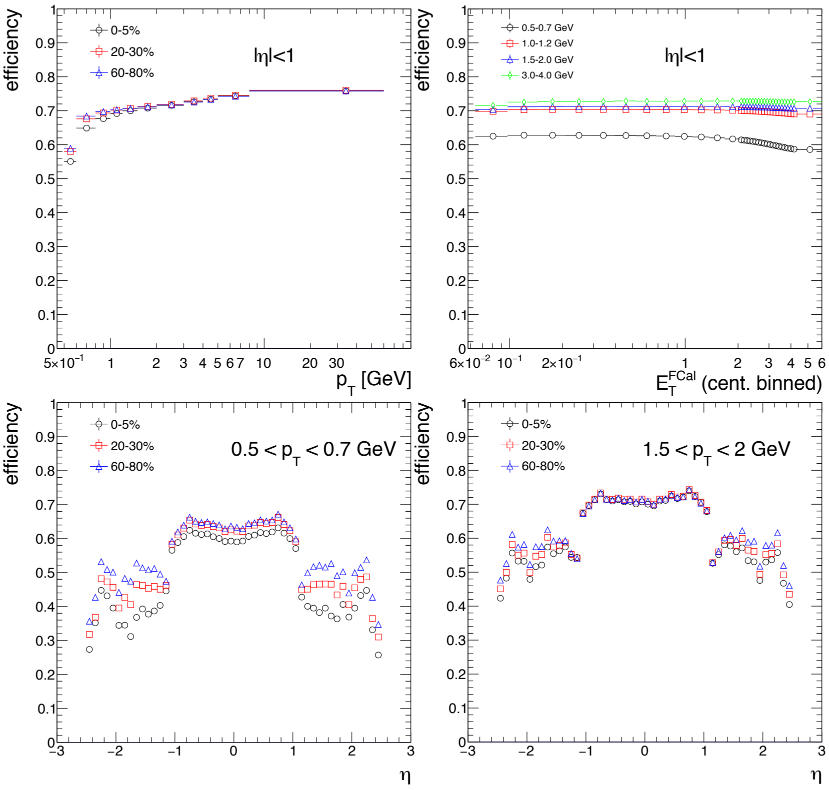

Figure 4.7: Tracking efficiency as a function of p_{T} (top left) $\Sigma E_{\mathrm{T}}^{FCal}$ (top right) and as a function of η in at low p_{T} (bottom left) and high p_{T} (bottom right).

4.6.2 Fake track rates

Fake track rate is defined as:

$$f = \frac{N_{\text{reco}}|NOT\ matched\ to\ truth}{N_{\text{reco}}} \tag{4.2}$$

where the N_{reco} in the denominator is the total number of reconstructed tracks. The numerator corresponds to the number of tracks, which were not matched to a primary, stable generated MC particles or are produced from random combinations of hits in the ID and thus not matched to any particle. Figure 4.8 shows an overview of the fake tracks rate as a function of p_{T} and η for different centrality intervals. The fake rate shows significant dependence on η. The highest values are observed in central events, low p_{T} and in the region of transition from the barrel to endcaps, reaching up to 18% of all reconstructed tracks. Number of fakes drops quickly at higher p_{T} and for semi-central and peripheral events up to ~5% for 60–80% event centrality. For $|\eta| < 1$ and low-p_{T} tracks it varies from ~10% to ~3–5% for the most central events to the peripheral events, respectively. No significant fake rate dependence on centrality is observed in the 0–1% most central collisions.

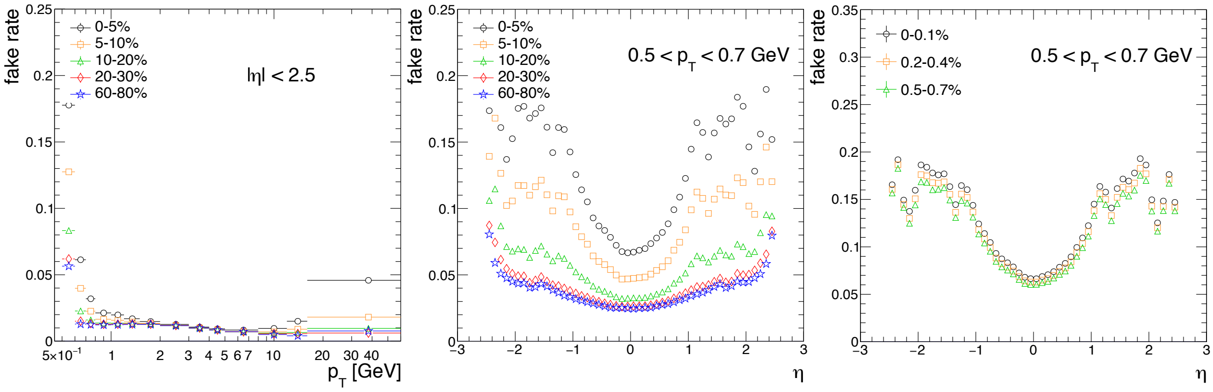

FIGURE 4.8: Fake rates as a function of p_{T} for several centrality bins (left panel); fake rates as a function of η for lowest p_{T} in a broad centrality range (middle panel) and for very central events (right panel).

Chapter 5

Methodology

5.1 Azimuthal anisotropy measurements

Over the years, several experimental methods developed to evaluate the v_n coefficients. The event-plane [42, 48] and scalar-product [84] methods, that are the main focus of the presented thesis, can be seen as a particular case of the two-particle correlation method [49]. The 2PC can be extended further to $2k$-particle correlations calculated with multi-particle cumulant method [85]. Finally, there is Lee-Yang Zeros (LYZ) method, which extracts the v_n harmonics from the correlation among a large number of particles [86]. The 2PC method is briefly described in section 8.5, while the cumulant and LYZ methods are not covered in the scope of this work.

5.1.1 The event-plane method

The idea behind the event-plane method [42, 48] is correlating the particles emitted in each event with the reaction plane angle of that event, related to the orientation of the impact parameter. The real reaction plane angle is not measurable experimentally. However, an estimate of the reaction plane, called the event-plane, is measurable using emitted particles. It is denoted as Ψ_n for the n-th order plane. The n-th event-planes are determined using information from sub-detectors at different η. In ATLAS the event-plane detector is the FCal detector. The granularity of FCal allows for precise measurements of harmonic planes for $n = 2$–7. Moreover, the large separation in η between both sides of FCal allows for reduction of short-range correlations when correlating both event-plane angles. For the same reason short-range correlations are reduced in measurements involving tracks in ID.

The azimuthal distributions of ID tracks as well as FCal calorimeter towers are used to define the flow vectors as:

$$Q_n = |Q_n| e^{in\Psi_n} = \frac{1}{\sum_j w_j} \sum_j q_{n,j} = \frac{1}{\sum_j w_j} \sum_j w_j e^{in\phi_j}, \tag{5.1}$$

where the sums run over tracks or calorimeter towers in a single event restricted to a selected region of $\eta - p_{\mathrm{T}}$ space. The ϕ_j is track or calorimeter tower azimuthal angle and n is the harmonic order. The weight, w_j, when Q_n is obtained from FCal is accounting for the number of particles registered in the calorimeter tower and is thus proportional to the transverse energy, E_{T}, in the tower. In case of tracks the weights are correcting for ID detector inefficiency to reconstructed charged particles. The Q_n-vector orientation delivers the EP angle:

$$\Psi_n = \frac{1}{n}\tan^{-1}\frac{Q_{n,y}}{Q_{n,x}} = \frac{1}{n}\tan^{-1}\frac{\sum_j w_j sin[n(\phi_j)]}{\sum_j w_j cos[n(\phi_j)]}. \tag{5.2}$$

The raw n-th order flow harmonic is defined using correlation of particles with Ψ_n as [49]:

$$v_n^{\text{obs}} = \langle \cos[n(\phi_j - \Psi_n)]\rangle, \tag{5.3}$$

where angle brackets stand for the average over tracks. Since the Ψ_n estimate differs from Ψ^{RP}, the v_n^{obs} has to be corrected for the factor related to the n-th order event-plane resolution. The resolution correction factor, R_n, is obtained as:

$$R_n = \sqrt{\langle \cos[n(\Psi_n - \Psi^{\text{RP}})]\rangle}. \tag{5.4}$$

The angle brackets denotes an average over events. In the limit of infinite number of particles, i.e. $v_n \gg 1/\sqrt{N}$, where N is the number of particles, the Ψ_n can be exactly reconstructed as $\Psi_n = \Psi_n^{RP}$ and thus the resolution approaches unity: $R_n \longrightarrow 1$. In the opposite limit, $v_n\sqrt{N} \ll 1$, the resolution is low: $R_n \longrightarrow kv_n$, where $k \sim \sqrt{N}$ [87].

There are several techniques to estimate the resolution factor, R_n, including e.g. full-event and sub-event resolution techniques [48, 49]. In this analysis, it is determined using correlation of event-plane angles obtained from two similar sub-events at different pseudorapidity regions. The R_n is calculated with sub-event N that covers the negative region of η ($-4.9 < \eta < -3.2$) and sub-event P that covers the positive η ($3.2 < \eta < 4.9$). If any correlations not related to the flow are assumed to be negligible, the relation between the two EP angles, Ψ_n^N and Ψ_n^P, and the reaction plane can be expressed as follows:

$$\langle \cos[n(\Psi_n^N - \Psi_n^P)]\rangle = \langle \cos[n(\Psi_n^N - \Psi^{RP})]\rangle\langle \cos[n(\Psi_n^P - \Psi^{RP})]\rangle, \tag{5.5}$$

where Ψ_n^N and Ψ_n^P are estimated in sub-event N and P, respectively. When the two sub-events have similar multiplicity then the resolution correction for each sub-event is:

$$R_n = \langle \cos[n(\Psi_n^N - \Psi^{RP})]\rangle = \langle \cos[n(\Psi_n^P - \Psi^{RP})]\rangle = \sqrt{\langle \cos[n(\Psi_n^N - \Psi_n^P)]\rangle}. \tag{5.6}$$

The v_n obtained with EP method is defined as:

$$v_n\{\text{EP}\} = \frac{v_n^{obs}}{R_n} = \frac{\langle \cos[n(\phi_j - \Psi_n^{N|P})]\rangle}{\sqrt{\langle \cos[n(\Psi_n^N - \Psi_n^P)]\rangle}}, \tag{5.7}$$

where $\Psi_n^{N|P}$ denotes the Ψ_n^N or Ψ_n^P depending on the η of the $j-th$ track. If the ϕ_j of the track is associated with the η range within $0-2.5$ then $\Psi_n^{N|P} \longrightarrow \Psi_n^N$. Whereas if the ϕ_j of the track is from $-2.5 < \eta < 0$, then in the numerator $\Psi_n^{N|P} \longrightarrow \Psi_n^P$. Such choice provides a maximum η-separation between tracks and Ψ_n allowing for reduction of the bias from short-range effects. Using the notation from Eq. (5.1), the Eq. (5.7) can be expressed as:

$$v_n\{\mathrm{EP}\} = Re\frac{\left\langle q_{n,j}\frac{Q_n^{N|P*}}{|Q_n^{N|P}|}\right\rangle}{\sqrt{\left\langle\frac{Q_n^N}{|Q_n^N|}\frac{Q_n^{P*}}{|Q_n^P|}\right\rangle}}, \tag{5.8}$$

where the subscripts N and P have the same meaning as for Ψ_n. The imaginary parts of the numerator and denominator in Eq. (5.8) can be neglected (set to 0), as a result of the symmetry with respect to the reaction plane (except for statistical fluctuations). The Q-vectors, Q_n^N and Q_n^P, are measured for each FCal arm using calorimeter towers within $-4.8 < \eta < -3.2$ and $3.2 < \eta < 4.8$, respectively. The $q_{n,j} = |q_{n,j}|e^{in\phi_j}$ is associated with $j-th$ charged track in the ID. The η separation in the EP method is illustrated in Figure 5.1. The ID tracks ($q_{n,j}$) at positive η are correlated with the Q_n obtained in negative η FCal arm and those at the negative η with the Q_n obtained in the positive η FCal arm.

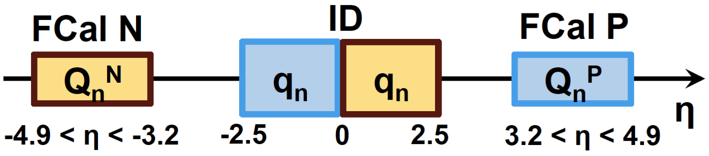

FIGURE 5.1: Illustration of the flow vectors used in the EP method.

The disadvantage of the EP method is that the same resolution correction is applied for all events in a centrality class. In practice, the reaction plane resolution depends on the multiplicity of particles used to define the event plane angle and the magnitude of the anisotropy v_n. In the high resolution limit ($R_n \to 1$):

$$v_n\{\mathrm{EP}\} \to \frac{\langle v_n \cdot 1\rangle}{\sqrt{1^2}} = \langle v_n\rangle, \tag{5.9}$$

while in the low resolution limit ($R_n \to kv_n$):

$$v_n\{\mathrm{EP}\} \to \frac{\langle v_n \cdot kv_n\rangle}{\sqrt{\langle k^2v_n^2\rangle}} = \sqrt{\langle v_n^2\rangle}, \tag{5.10}$$

Consequently, in realistic experimental conditions the v_n measured with the EP method does not estimate the $\langle v_n\rangle$ but the quantity in between $\langle v_n\rangle$ and $\sqrt{\langle v_n^2\rangle}$ in a detector dependent manner. Such an ambiguity is relevant when comparing results from different experiments or models.

5.1.2 The scalar-product method

The scalar-product method (SP) has been introduced by the STAR Experiment [84] and further discussed in Ref. [49] as the alternative to the EP method. The advantage of the SP method is that it removes the clear dependence on event planes. Therefore the $v_n\{SP\}$ is always $\sqrt{\langle v_n^2\rangle}$ [87]. The $v_n\{SP\}$ formula is constructed using the notation from Eq. (5.1) and is obtained by removing the $|Q_n|$ normalization factors in Eq. (5.8):

$$v_n\{\mathrm{SP}\} = Re\frac{\langle q_{n,j}Q_n^{N|P*}\rangle}{\sqrt{\langle Q_n^N Q_n^{P*}\rangle}}, \tag{5.11}$$

where the * denotes complex conjugation and the angular brackets indicate an average over all tracks and all events. As in the EP method, the sine term in numerator and denominator are neglected in $v_n\{\mathrm{SP}\}$ calculation. The notation used in the numerator of Eq. 5.11, $N|P$, indicates the choice of Q_n^P or Q_n^N described in section 5.1.1. The Q_n vectors are used to construct scalar products which carry information on the azimuthal correlation between the two regions for which the flow vectors are defined. The scalar product, averaged over many events, calculated for two regions which are not correlated should be zero. Consequently, a formula in Eq. (5.11) can be rewritten as follows:

$$v_n\{\mathrm{SP}\} = \frac{\langle cos[n(\phi_j - \phi_n^{N|P})]\rangle}{\sqrt{\langle cos[n(\phi_n^N - \phi_n^P)]\rangle}}, \tag{5.12}$$

where ϕ_j is related to $j-th$ track azimuthal angle. The ϕ_n^N and ϕ_n^P correspond to the azimuthal angles of calorimeter towers from sub-events N and P, respectively. Moreover, the cosine terms are weighted by the weights proportional to the tower E_{T}. The SP method introduces the same large separation in η as the EP method by correlating ID tracks with the FCal towers from the opposite η hemispheres. The advantage of SP method is its unambiguity in v_n measurement as compared to the EP method. The SP method always measures the:

$$v_n\{\mathrm{SP}\} = \sqrt{\langle v_n^2\rangle}. \tag{5.13}$$

For that reason, the SP method is a better choice to compare results between different experimetnts and theoretical models.

5.2 Detailed analysis description

5.2.1 Detector calibration: event plane and flow vector uniformity

The orientation of the collision reaction plane (or the impact parameter vector) is random from event-to-event. Therefore, the Ψ_n distributions should be uniform. In other words the Q-vector is not expected to be biased towards any preferable direction, i.e. averaged over many events should be zero. In practice, the event plane modulations, Ψ_n or Q_n, measured in the event-plane detector (FCal) can be biased due to detector effects including e.g. mis-calibration, inefficiencies or dead areas. For example, the regions with dead towers yield a smaller contribution to Q_n-vectors estimation comparing to fully active areas. As a result, the Q_n-vectors will be biased away from those regions. Such effects directly affect the calculation of the resolution correction factor, R_n, and thus v_n measurement. To eliminate any detector non-uniformity a two-step re-centering and flattening procedure is applied to the Q_n-vectors.

Re-centering Q_n-vector correction

The flow vectors are required to be centered at (0,0) in the whole detector, independently on the event centrality. The correction is based on subtracting the mean Q_n in each narrow 1% centrality bin and on a run-by-run basis for each FCal arm [51]:

$$Q_n = Q_n^{raw} - \langle Q_n^{raw} \rangle. \tag{5.14}$$

The Q_n^{raw} corresponds to the *raw* Q_n-vectors calculated without any correction. The Q_n^{raw} averaged over many events, $\langle Q_n^{raw} \rangle$, have non-zero real (x) and imaginary (y) components. Figure 5.2 shows an example of the mean of the Q_2-vector as a function of $\Sigma E_{\mathrm{T}}^{FCal}$ before and after the correction. The real and imaginary parts of the Q_2-vector are shown in the left panel and right panel, respectively. The raw $Q_{2,x}$ and $Q_{2,y}$ are significantly shifted from (0,0) in the entire centrality range. The higher-order flow vectors show similar tendency for the raw measurement. The distributions for $n > 2$ are included in the Appendix A. Such re-centering is done for each order of Q_n-vector.

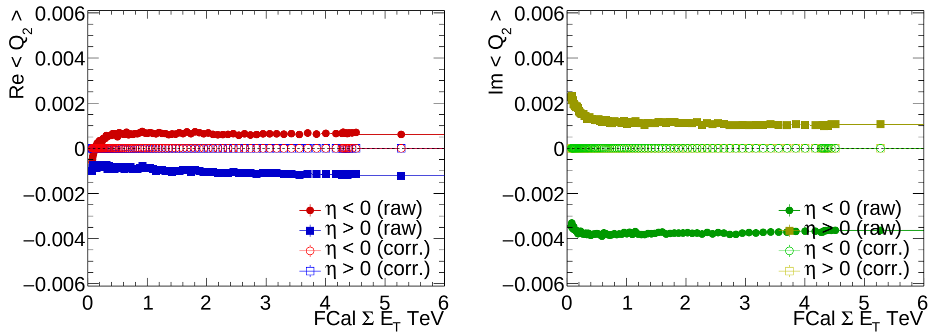

FIGURE 5.2: Mean Q_2-vector constituents as function of ΣE_T^{FCal} before (solid points) and after (open points) correction. The distributions are shown for both FCal sides: $\eta < 0$ and $\eta > 0$. Left panel presents real part of Q_2 and the right panel presents imaginary part of Q_2.

Q_n-vector skewness correction

Some additional non-uniformities persist in the Ψ_n and Q_n distributions after correcting for the non-vanishing $\langle Q_n^{raw} \rangle$. They arise from higher-order detector irregularities that lead to a distortions in the $Q_{n,x}Q_{n,y}$ distributions. In order to correct for these effects and make $\langle Q_{n,i}Q_{n,j} \rangle$ $(i = x, y; j = x, y)$ proportional to the identity matrix, the second-step correction is introduced in which the re-centered Q_n vector is multiplied by the matrix [88]:

$$\frac{1}{\sqrt{N}} \begin{pmatrix} \langle Q_{n,y}^2 + D \rangle & -\langle Q_{n,x}Q_{n,y} \rangle \\ -\langle Q_{n,x}Q_{n,y} \rangle & \langle Q_{n,x}^2 + D \rangle \end{pmatrix}, \tag{5.15}$$

where $D = \sqrt{\langle Q_{n,x}^2 \rangle \langle Q_{n,y}^2 \rangle - \langle Q_{n,x}Q_{n,y} \rangle^2}$ and $N = D\left(\langle Q_{n,x}^2 \rangle + \langle Q_{n,y}^2 \rangle + 2D\right)$, which is a normalized inverse square root of the covariance matrix. Such multiplication, called the skewness correction, results in $\langle Q_{n,x}Q_{n,y} \rangle = 0$ and $\langle Q_{n,x}^2 \rangle = \langle Q_{n,y}^2 \rangle$. The corrected Q_n vector have no skew and have the same width in the $Q_{n,x}$ and $Q_{n,y}$ axes. Figure 5.3

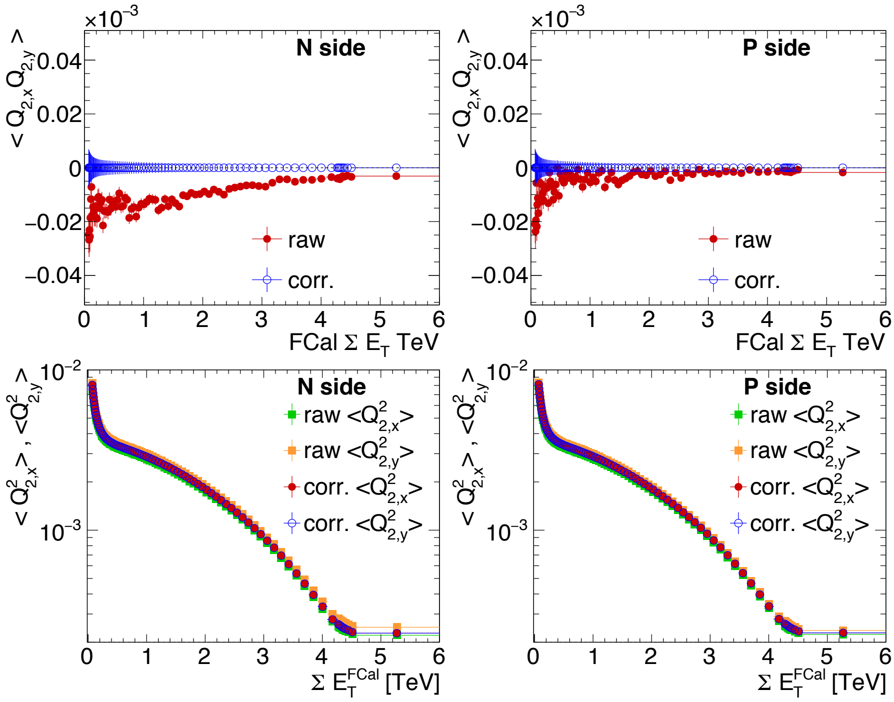

FIGURE 5.3: Top raw: $\langle Q_{2,x}Q_{2,y}\rangle$ as function of $\Sigma E_{\mathrm{T}}^{FCal}$ before and after Q_n-vector corrections. Bottom row: $\langle Q^2_{n,x}\rangle$ and $\langle Q^2_{n,y}\rangle$ as function of $\Sigma E_{\mathrm{T}}^{FCal}$ after Q_n-vector corrections.

shows the $\langle Q_{2,x}Q_{2,y}\rangle$, $\langle Q^2_{2,x}\rangle$ and $\langle Q^2_{2,y}\rangle$ distributions before and after the skewness correction, obtained at N and P side as a function of $\Sigma E_{\mathrm{T}}^{FCal}$. Higher-order Q_n-vectors behave similarly. The distributions for $n > 2$ are included in the Appendix A. The $\langle Q_{n,x}Q_{n,y}\rangle$ distribution is centrality dependent and therefore the second-step of Q_n-vector correction is done in narrow 1% centrality bins as well. The effect of the Q_n-vector corrections on the Ψ_n angle uniformity is shown in Figure 5.4 for $n = 2$ and two example centrality intervals: 0–10% and 30–40%. Ψ_2 distributions are shown for both FCal sides, before, after applying only re-centering Q_n-vector correction and after applying both Q_n-vector corrections. The first-step correction significantly improves the event-plane angle modulations, but some biases are still present. The second-step correction removes any residual non-uniformities and Ψ_n distributions become fully uniform. The first and second Q_n-vector corrections can be crosschecked by looking at Ψ_n^N vs. Ψ_n^P correlation. The Ψ_n^N and Ψ_n^P are expected to be fully uniform and thus correlated when following the above procedure. Figure 5.5 shows the event plane angles from N and P side correlations before and after first and second corrections for $n = 2$–7 harmonics. The left column corresponds to the Ψ_n^N vs. Ψ_n^P without correction. The right column shows the event-plane correlations after applying both corrections. For n=2–6 both event planes are strongly correlated as it should be, since they are estimates of the same, unique for a given event, reaction plane. The correlation for $n = 7$ is less pronounced but not negligible.

Figure 5.6 shows the $\Sigma E_{\mathrm{T}}^{FCal}$ dependence of resolution corrections for the scalar-product (left panel) and event-plane (right panel) methods for n =2−7 harmonics. The binning in the plot corresponds to 1% centrality intervals (see section 4.3 for centrality definition). In both methods the maximum values of the resolution correction

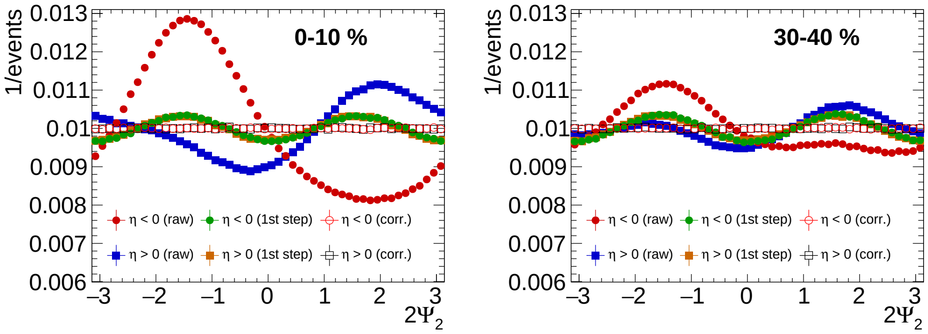

FIGURE 5.4: The distributions of the event-plane angles Ψ_2 before (solid points) and after the Q_n-vector corrections (open points). The event plane angle is measured in the FCal at negative (dots) and positive (squares) η for central 0-10% and mid-central 30-40% events. Distributions are normalized to the number of events.

factors (smallest correction) are observed in mid-centrality region, where the v_2 is well pronounced. For higher order harmonics ($n = 3$–7) resolution correction factors are smaller and less centrality dependent.

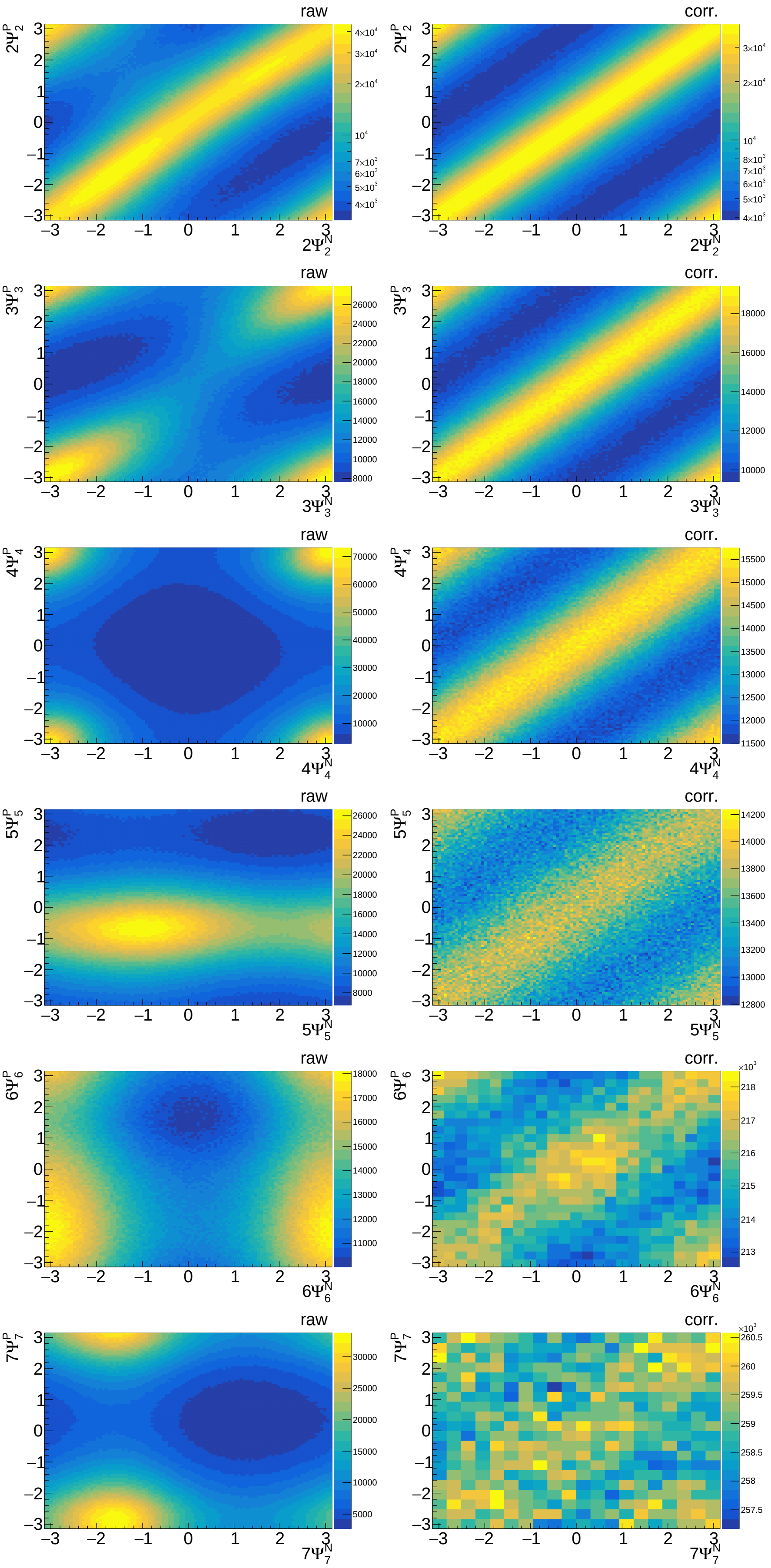

FIGURE 5.5: Event plane angle correlations at negative N and positive P side of FCal for the harmonic order n =2–7, before (left column) and after (right column) Q_n-vector correction. Each row corresponds to a different harmonic, starting from $n = 2$ in top row up to $n = 7$ in bottom row.

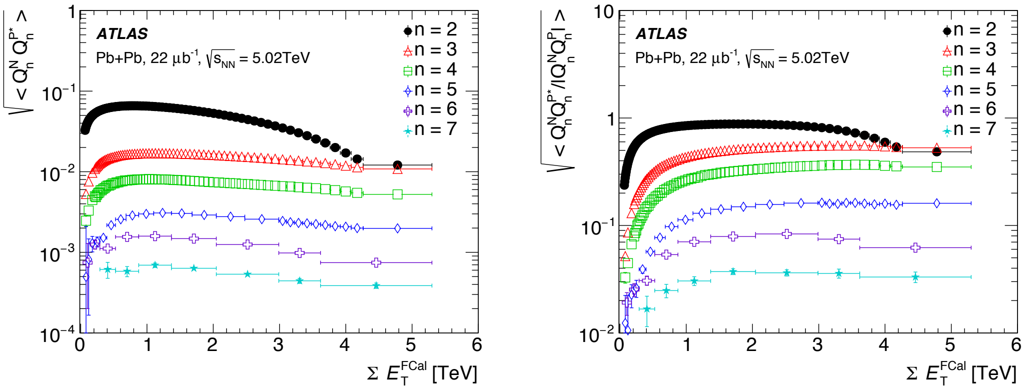

FIGURE 5.6: The resolution correction factors $R_n\{\text{SP}\}$ (left) and $R_n\{\text{EP}\}$ (right), dependence on ΣE_T^{FCal}.

5.2.2 Tracking corrections

Similarly to the signals measured in the FCal, it is expected that the azimuthal angle distributions of ID tracks should be uniform, showing no modulation when averaged over many events. In order to achieve that, tracks are weighted to make ϕ-distribution uniform in each narrow η slice of 0.1 width. Track weights are calculated as a ratio of mean number of tracks in the η slice, over the number of tracks in each $\eta \times \phi = 0.1 \times 0.1$ bin: $w_i^{trk} = \frac{\langle N\rangle^{\eta}}{\langle N\rangle^{\eta,\phi}}$. The $\eta - \phi$ maps of weights are extracted for each run. Track weights are then applied track by track in the further analysis. Figure 5.7 shows an example of $\eta - \phi$ maps for one example run (~0.7 M of events) before and after applying track weighting (left and middle panel respectively), and the $\eta - \phi$ map of track weights for this run (right panel).

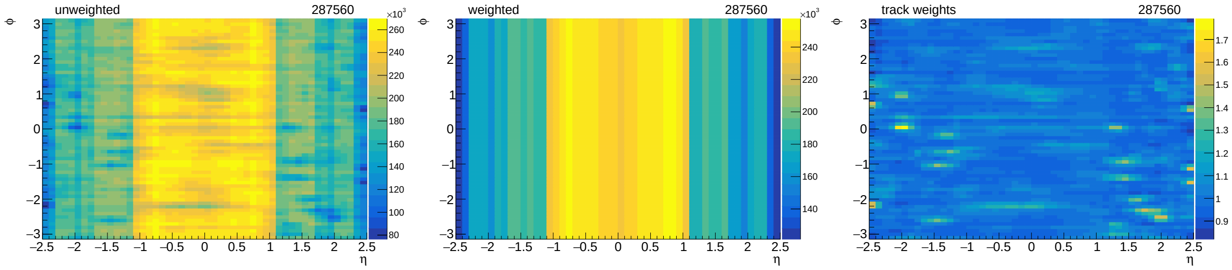

FIGURE 5.7: The $\eta - \phi$ map before track weighting (left panel) extracted from one run. The same $\eta - \phi$ map after applying track weighting (middle panel). The $\eta - \phi$ map with track weights (right panel).

5.2.3 Flow harmonics measurements with the scalar-product and event-plane methods

The analysis chain is similar for both methods and requires several passes over the full 5.02 TeV Pb+Pb dataset consisting of 32 runs. About 136 M events pass the selection requirements, which are described in section 4.1. The analysis steps can be summarized as follows:

1. At first, a loop over all events is performed to determine the $\langle Q_n^{raw} \rangle$ separately in each run.

2. In the second step, the Q_n-vectors are centered at (0,0) as described in section 5.2.1. Such centered Q_n-vectors are used to determine elements of matrix in Eq. (5.15) required in the next step of analysis procedure.

3. In the third pass over events, the second-step Q_n-vector correction is applied according to the procedure described in section 5.2.1. The azimuthal modulation in the calorimeter is fully uniform at this step. The resolution factors for both, SP and EP, methods are calculated run by run as a function of the narrow 1% collision centrality bins. The resolution correction factors for SP and EP are calculated according to denominators in Eqs. 5.11 and 5.8 (or 5.12 and 5.7), respectively. Simultaneously, in the third pass, the track weighting matrices are determined as described in section 5.2.2.

   The final formula for SP resolution factor:

   $$R_n\{\mathrm{SP}\} = \sqrt{\frac{1}{N^{total}} \sum_{k=1}^{runs} \sum_{j=1}^{events} |Q_{n,k,j}^{N}||Q_{n,k,j}^{P}| \cos n(\Psi_{n,k,j}^{N} - \Psi_{n,k,j}^{P})}, \tag{5.16}$$

   where all symbols have the same meaning as in Eq. (5.12) and N^{total} is the total number of events in all runs in a given centrality bin.

   The final formula for EP resolution factor:

   $$R_n\{\mathrm{EP}\} = \sqrt{\frac{1}{N^{total}} \sum_{k=1}^{runs} \sum_{j=1}^{events} \cos n(\Psi_{n,k,j}^{N} - \Psi_{n,k,j}^{P})}, \tag{5.17}$$

   where $\Psi_n^{N|P}$ is obtained using Eq. 5.2.

4. Finally, in the last step the v_n harmonics are determined in narrow centrality, p_{T} and η intervals to avoid biases related to a finite bin width. Table 5.1 describes the fine binning over the full phase space used for the v_n measurement. The SP and EP v_n harmonics are obtained in each p_{T}, η and centrality bin according to the formulas:

	number of bins	bin width	range
p_{T}	600	0.1	0.5 - 60 GeV
η	50	0.1	-2.5 - 2.5
centrality	79	1%	1-80%
centrality	10	0.1%	0-1%

TABLE 5.1: Summary of the fine binning over the full phase space used in the analysis.

for the scalar-product method:

$$v_n^{fine}\{\mathrm{SP}\} = \frac{1}{R_n\{SP\}} \sum_{k=1}^{runs} \sum_{j=1}^{events} \sum_{i=1}^{tracks} c_{k,i} |Q_{n,j,k}^{N|P}| \cos n(\phi_i - \Psi_{n,j,k}^{N|P}), \tag{5.18}$$

for the event-plane method:

$$v_n^{fine}\{\mathrm{EP}\} = \frac{1}{R_n\{EP\}} \sum_{k=1}^{runs} \sum_{j=1}^{events} \sum_{i=1}^{tracks} c_{k,i} \cos n(\phi_i - \Psi_{n,j,k}^{N|P}), \tag{5.19}$$

where $c_{k,i}$ is track weight, applied to correct for detector biases as described in 5.2.1.

5.2.4 Integrated v_n

The analysis chain presented in the previous section uses much narrower p_{T}, η and centrality bins than bins used for the final SP and EP v_n harmonics presentations. To obtain integrated v_n, for a wider intervals of p_{T}, η or centrality, integration over the fine-binning v_n weighted by the total number of tracks in that bin is performed. Corrections for tracking reconstruction inefficiency and fake rates (described in section 4.6) are significant and have to be included. To account for them, each sum over phase space bins is scaled by the additional correction factor:

$$(1 - f)/\epsilon,$$

where f is the fake fraction and ϵ is the tracking efficiency. Both, f and ϵ are functions of particle transverse momentum, pseudorapidity and centrality. The correction factors are obtained in bins, corresponding to those used in the v_n measurement, thus, they are the same for tracks belonging to a given fine p_{T}, η and centrality bin. The formula for integrated v_n taking into account the tracking efficiency correction factors reads:

$$v_n = \frac{1}{\sum_i \sum_j N_{i,j} \frac{1-f(\eta_i, p_{\mathrm{T},j})}{\epsilon(\eta_i, p_{\mathrm{T},j})}} \sum_j \sum_i v_n^{fine}(\eta_i, p_{\mathrm{T},j}) N_{i,j} \frac{1 - f(\eta_i, p_{\mathrm{T},j})}{\epsilon(\eta_i, p_{\mathrm{T},j})}, \tag{5.20}$$

where subscripts i and j iterate over the bins of p_{T} and η, respectively. $N_{i,j}$ is the number of tracks in given bin of p_{T} and η. The $(1 - f)/\epsilon$ correction has the most significant impact, when either the v_n harmonics or tracking performance vary significantly over the measurement range.

Chapter 6

Monte Carlo studies

A valuable handle on studying the azimuthal anisotropy is provided by the detector simulation of Pb+Pb collisions. A detailed MC study of the v_n harmonics is performed using the MC HIJING sample described in Section 4.5. HIJING does not incorporate any final state re-interactions among the produced particles (partons or hadrons), and thus does not provide anisotropic particle flow. Therefore, for the studies of anisotropic effects, a special procedure called flow "afterburner" [89] to simulate flow effects was developed. The flow harmonics v_n are implemented via redistribution of the particles azimuthal angles in order to get the desired elliptic flow signal. In this process, the azimuthal angle of each particle is changed: $\phi \longrightarrow \phi + \Delta\phi$, where $\Delta\phi$ depends on v_n values known from experimental measurements and the reaction plane angles [48].

6.1 Monte Carlo closure test

The MC analysis procedure is identical to that from real data analysis. The v_n^{true} obtained from the MC generated particles are compared to the v_n^{reco}. The v_n^{reco} is determined by applying the same procedures to the MC sample as are applied to the real data. Such comparison, known as *closure test*, provides information about the validity of the reconstruction procedure and any additional detector effects that the data analysis should be corrected for. Due to statistics limitation the v_n measurement can not be established for the small v_n signals, such as v_7, thus, the MC studies are done for $n = 2$–6. This section covers the MC studies for v_2, while the results for higher-order harmonics are included in Appendix B.

Figure 6.1 shows the $\frac{v_2^{reco}}{v_2^{true}}$ dependence on p_{T} obtained in 9 centrality bins for both SP and EP methods. The v_n^{reco} is determined using selected reconstructed tracks (see section 4.4) and true event-plane angle as used by the flow afterburner program. The v_n^{true} is determined using generated primary particles from ID and the same event-plane angle. Overall, a good agreement between v_2^{reco} and v_2^{true} harmonics is observed. However, about 6% difference between reconstructed and true v_2 is found in the most central collisions at low $p_{\text{T}} < 1$ GeV. The non-closure is attributed in the first place to an additional in-plane inefficiency and, in a lesser extent, to the presence of fake tracks. These effects are discussed in the Section 6.2. Since the sources of the non-closure are known, its magnitude is used to correct the measurement based on experimental data, to provide more reliable results. The non-closure correction, resulting mainly from the in-plane tracking inefficiency correction, is established for a wide p_{T} and η bins (to avoid statistical fluctuations) and then applied to the real data bin-by-bin in p_{T} and η

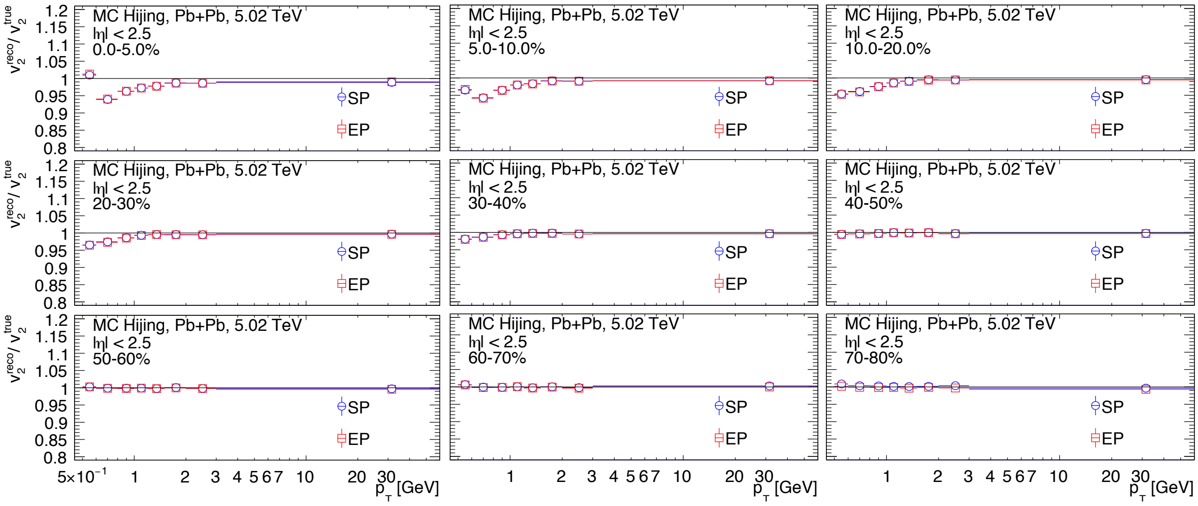

FIGURE 6.1: The v_2 (p_T) closure test for SP (blue solid points) and EP (red open points) in 9 centrality bins. Error bars correspond to statistical uncertainties

for 0–40% most central events as follows:

$$v_n^{\text{corr}} = \frac{v_n}{r_{\text{closure}}}, \quad \text{where} \quad r_{\text{closure}} = \frac{v_n^{\text{reco}}}{v_n^{\text{true}}}. \tag{6.1}$$

Results shown in chapter 8 include above correction.

6.2 Sources of Monte Carlo non-closure

The v_n MC closure test revealed some inefficiencies in low p_T bins and in the most central events. Generally, lower v_n^{reco} values are obtained when compared to v_n^{true}. This effect is found to be the result of azimuthal variation of track reconstruction efficiency that is correlated with event-plane angle. The $\Delta\phi = \phi - \Psi_n$ efficiency distributions show lower inefficiency in-plane than out-of-plane direction. An example of $\Delta\phi$ distribution, obtained for the second order event plane ($n = 2$), for in 5−10% centrality bin and $p_T = 0.8{-}1$ GeV, is shown in Figure 6.2. The top panel shows comparison of $\Delta\phi$ distributions for reconstructed and generated particles both normalized independently. The efficiency $\epsilon_n = \frac{\phi_n^{reco} - \Psi_n}{\phi_n^{true} - \Psi_n}$ is presented at the bottom panel. Moreover, the efficiency is fitted with the cosine function: $fit(\phi - \Psi_n) = A(1 + v_n \cos[2(\phi - \Psi_n)]$ also shown in the plot. To remove the non-closure of v_n values at low-p_T in the most central collisions, the $\Delta\phi$-dependent efficiency was used track-by-track in the v_n harmonics calculation. Figure 6.3 shows an example result of such correction, where the v_n closure is shown as a function of p_T and η in one centrality bin. The application of $\Delta\phi$-based correction improves the v_n closure. Similar behavior of the correction is observed for higher order harmonics. However, due to low MC event statistics the $\Delta\phi$-dependent efficiency correction was not applied in the measurement.

In the most central events at $p_T \approx 0.5$ GeV, closure test revealed that the v_n^{reco} is larger than v_n^{true}. It was found that the overestimation of v_n harmonics results from high rates of fake tracks. In more peripheral events and at higher p_T the v_n^{reco} and v_n^{true} agree well (see Figure 4.8). To examine the problem, additional crosscheck was done. The closure test

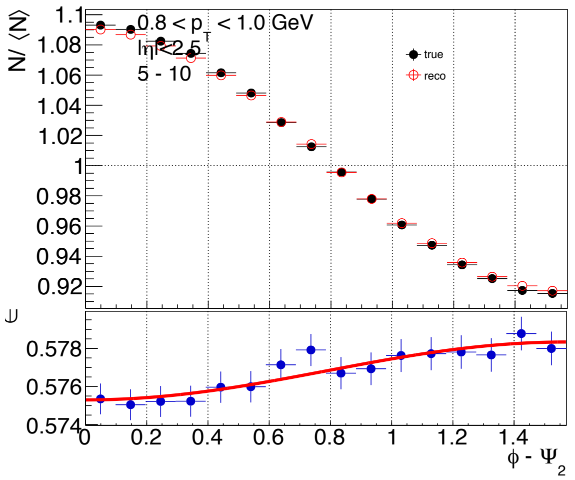

FIGURE 6.2: The $\phi - \Psi_2$ distribution for true and reconstructed tracks (top panel) in centrality bin 5−10%. The track reconstruction efficiency as a function of $\phi - \Psi_2$ (lower panel). The red line is a fit to efficiency, fit$(\phi - \Psi_2) = A(1 + v_2 \cos[2(\phi - \Psi_2)]$.

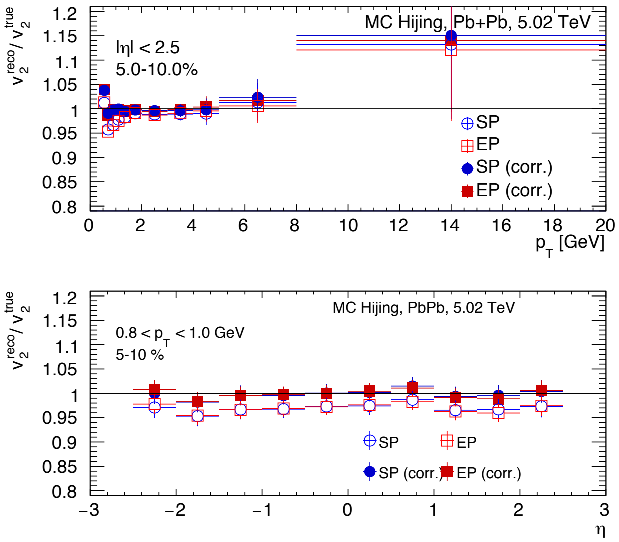

FIGURE 6.3: The v_2 closure without any correction (open points) compared to v_2 closure obtained with $\Delta\phi$-dependent efficiency correction (solid points). Comparison is shown as a function p_{T} (top panel) and η (bottom panel) in one 5−10% centrality bin.

was repeated excluding reconstructed tracks that did not match to the primary particles in calculation of v_n^{reco}. Figure 6.4 shows an example of v_2 closure test performed for SP and EP methods using all reconstructed tracks and only tracks that are matched to the generated particles. The top plot shows $\frac{v_2^{\mathrm{reco}}}{v_2^{\mathrm{true}}}$ as a function of p_{T} up to 20 GeV, while the right plot corresponds to the same quantity obtained in $p_{\mathrm{T}} = 0.5$−0.6 GeV interval as a function of η. The difference between v_n^{reco} and v_n^{true} at low p_{T} follows the trend observed for higher p_{T} as a result of $\Delta\phi$ dependent efficiency effect. In previous ATLAS analysis it was found that in HIJING and detector simulation the number of fake particles is overestimated. The effect is accounted for using a dedicated fake correction described in the next section. To obtain the correction factor, the rate of the fake tracks in the MC

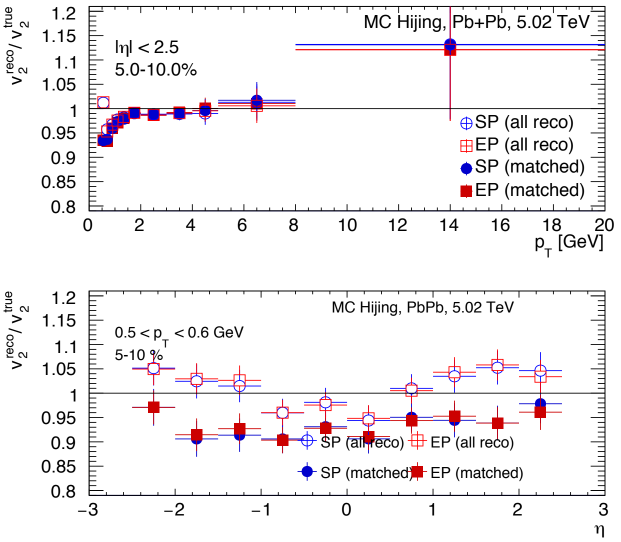

FIGURE 6.4: The v_2 closure test comparison between v_2^{reco} extracted from selected reconstructed tracks (open points) and v_2^{reco} extracted from tracks matched to generated primary particles (solid points). Both methods, EP (red points) and SP (blue points), are shown in one centrality interval 5−10% as a function of p_T (top) and η (bottom).

simulations was reexamined and scaled to the fake rates seen in the data.

6.3 Fake correction

HIJING does not describe the number of fakes very well. The difference in the fraction of fakes in data and MC can be seen in the impact parameter distributions. The left panel of Figure 6.5 shows distributions of transverse impact parameter in data and MC. There is a good agreement for $|d_0| < 1$ mm, while in the tails MC HIJING and data distributions do not agree. The former region ($|d_0| < 1$ mm) is dominated by the primaries that have almost exclusively small $|d_0|$ values. Fakes (including secondaries) have a much broader d_0-distribution and, thus, have almost 100% purity in the later region of $|d_0| > 2$ mm. The comparison indicated that there is more fakes in MC sample than in the data.

To quantify and correct the fraction of fakes in the MC sample an approach used in the minimum bias pp analysis [90] is adopted. In the approach, the primary and fake d_0 distributions are used as templates to fit the data d_0 distribution:

$$f^{data}(d_0) = A \cdot f_p(d_0) + B \cdot f_f(d_0), \tag{6.2}$$

where $f_p(d_0)$ and $f_f(d_0)$ are the d_0 distributions for primary and fake tracks, respectively, and the A and B are free parameters. The template fit to the data is performed in the range 2 mm < $|d_0|$ < 10 mm in different p_T and centrality ranges. The fitted parameters, A and B, can be used to estimate the fraction of fakes in the data as follows:

$$r_f^{data} = \frac{\int_{-1mm}^{1mm} \left(B \cdot f_f(d_0)\right) d(d_0)}{\int_{-1mm}^{1mm} (A \cdot f_p(d_0) + B \cdot f_f(d_0)) d(d_0)}. \tag{6.3}$$

The corresponding fraction of fakes in MC sample is given by the same above formula but A and B = 1:

$$r_f^{MC} = \frac{\int_{-1mm}^{1mm} \left(f_f^{MC}(d_0) \right) d(d_0)}{\int_{-1mm}^{1mm} \left(f_p^{MC}(d_0) + f_f^{MC}(d_0) \right) d(d_0)} \tag{6.4}$$

Eqs. (6.3) and (6.4) define scaling factor, s_f, used in MC to correct the number of fakes:

$$s_f = \frac{r_f^{data}}{r_f^{MC}}. \tag{6.5}$$

Applying the scaling factor as a weight to fake tracks, a corrected MC d_0 distribution is obtained, which is shown in the middle panel of Figure 6.5 for an example p_{T} and centrality intervals. The corrected MC distribution is consistent with data for the whole range of d_0. The right panel of Figure 6.5 shows the d_0 distributions for primaries and fakes, before and after applying fake scaling. After the scale-factor correction, the primary distribution is almost unchanged, while the number of fakes significantly decreased.

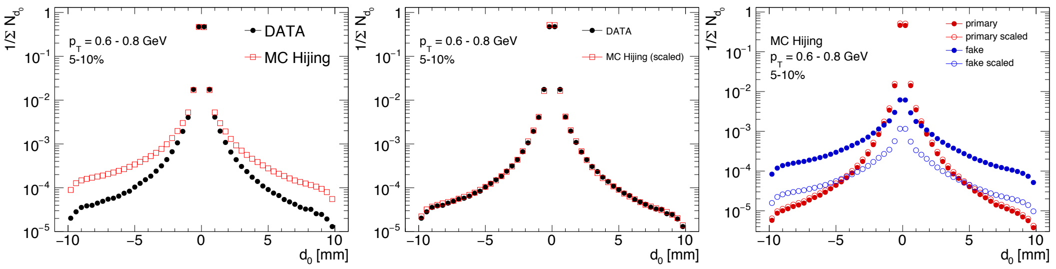

FIGURE 6.5: Left: "raw" d_0 distributions obtained using data (black points) and MC (red open points); middle: comparison of the d_0 distribution from data with the scaled MC distribution; right: the primary and fake d_0 distributions before and after applying fake scaling correction. All three panels are for 5–10% centrality bin and for p_{T} = 0.6–0.8 GeV.

It has been checked that fakes have an impact on v_n harmonics only for the most central events up to 20% and for $p_T < 0.8$ GeV. The fake scaling factors were applied in the MC closure test. The fake-corrected MC closure was later used as a correction to the data. However, it should be noted that the impact of the additional fake scale-factor correction on measured v_n harmonics is minimal as the overall impact of fakes on v_n is small.

Chapter 7

Sources of systematic uncertainty

Seven sources of systematic uncertainty affecting the v_n harmonics measurement are considered. The v_n results obtained after varying some aspects of the analysis are compared with the base v_n results and a relative difference: $\Delta_{\text{check}} v_n = \frac{v_n^{\text{base}} - v_n^{\text{check}}}{v_n^{\text{base}}}$ is used as the systematic uncertainty from a given source. Such cross-checks are done for all measured harmonics, $n = 2\text{–}7$, as functions of p_{T}, η and centrality over the phase space used in the baseline v_n measurement, as well as for both SP and EP methods. Due to limited statistics for higher order flow harmonics or/and peripheral collisions, the fine p_{T}, η or centrality bins are merged to avoid biases due to random fluctuations. In particular, such merging is done for high-p_{T}, peripheral collisions and/or higher order flow harmonics. The contributions estimated from the different sources are summed in quadrature in order to estimate the total systematic uncertainty on the v_n measurement. The following checks are performed in order to assess systematic uncertainties:

1. **Track selection:** Different track quality selections control the number of genuine charged particles and fake tracks that enter the analysis. Therefore, the v_n measurement is repeated with varied tracking selection requirements.

2. **Tracking efficiency:** The uncertainty of the efficiency estimation that results from e.g. uncertainty on the detector material needs to be accounted for in the v_n measurement. The tracking reconstruction efficiency is varied within its uncertainty.

3. **Centrality determination:** Uncertainty in estimation of the sampling fraction leads to an uncertainty of centrality binning. The former is known to a 1% precision and therefore a modification of centrality selections is performed to account for this effect.

4. **MC corrections:** The closure test quantifies an influence of the ϕ-dependent tracking efficiency and fake rates by comparing v_n measured using truth particles and reconstructed tracks.

5. **Residual sine term:** The imaginary parts of equations 5.11 and 5.8 should be zero. Any non-vanishing contributions are considered as systematic uncertainty.

6. **Variation of FCal acceptance in the $Q_n^{N|P}$ estimation:** To check the impact of FCal response on the v_n harmonics the measurement is repeated with subset of information from FCal.

7. **Detector non-uniformity:** Even after the correction procedures the residual non-uniformities have to be assessed. The asymmetry in v_n values of negative and positive η are used to quantify the effect.

All sources listed above are common for both, SP and EP, measurements. Sections 7.1 to 7.7 contain more detailed descriptions of each source. Magnitudes of all systematic uncertainties and the total systematic uncertainty are presented in the summary Figures 7.4 and 7.5 for two example centrality intervals and are discussed in Section 7.8.

7.1 Track selection

To study the impact of different track selection sets on the v_n values, the analysis is repeated with *HILoose* and *HITight+* track selections. Both are summarized in Table 4.4. The looser selection, i.e. *HILoose*, compared with the default set of cuts, uses less restrictive impact parameter cuts, $|d_0|$ and $|z_0 \sin\theta| < 1.5$ mm and more relaxed requirements for the number of SCT hits ($N_{hits} \geq 6$) and the number of holes ($N_{holes} \leq 2$), with other criteria unchanged. In turn, the *HITight+* selection differs from the default one by a more constraining pointing requirement of $|d_0|$ and $|z_0 \sin\theta|$ to be less than 0.5 mm.

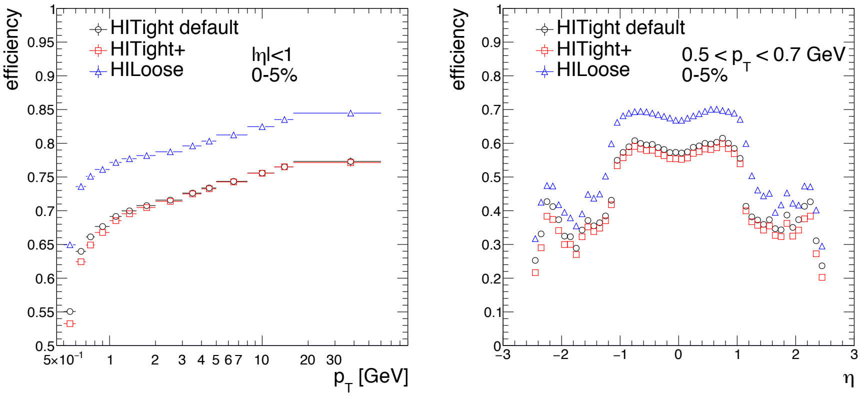

FIGURE 7.1: Tracking efficiencies of the nominal selection and two systematic variations as a function of p_{T} (left) and η (right). Kinematic and centrality selections are denoted in the legend.

Tracking performance of these selections are compared in Figure 7.1 and 7.2. The *HILoose* selection is systematically more efficient by about ~10% (in absolute terms). The fake track rate changes significantly for different selection cuts. As expected the largest fake rate is observed for the *HILoose*. For a given selection, the larges fake rates are seen at low p_{T} in the most central collisions.

The differential v_n harmonics are measured with the modified track selections and then they are integrated applying corresponding efficiency and fake rates. Using the $v_2 - v_7$ harmonics, relative changes, $\Delta_{trkloose} = \frac{v_n^{base} - v_n^{loose}}{v_n^{base}}$ for *HILoose* and $\Delta_{trktight} = \frac{v_n^{base} - v_n^{tight}}{v_n^{base}}$ for *HITight+*, are measured as functions of p_{T}, η and centrality. The $\Delta_{trkloose}$

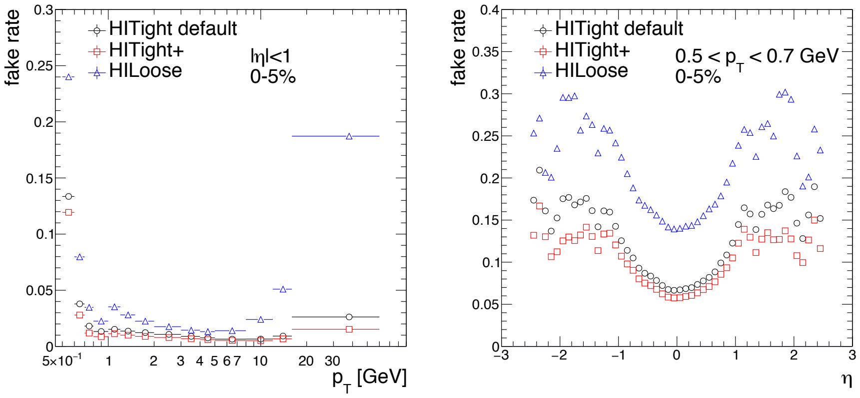

FIGURE 7.2: Fake tracks rate of the nominal selection and two systematic variations as a function of p_{T} (left) and η (right). Kinematic and centrality selections are denoted in the legend.

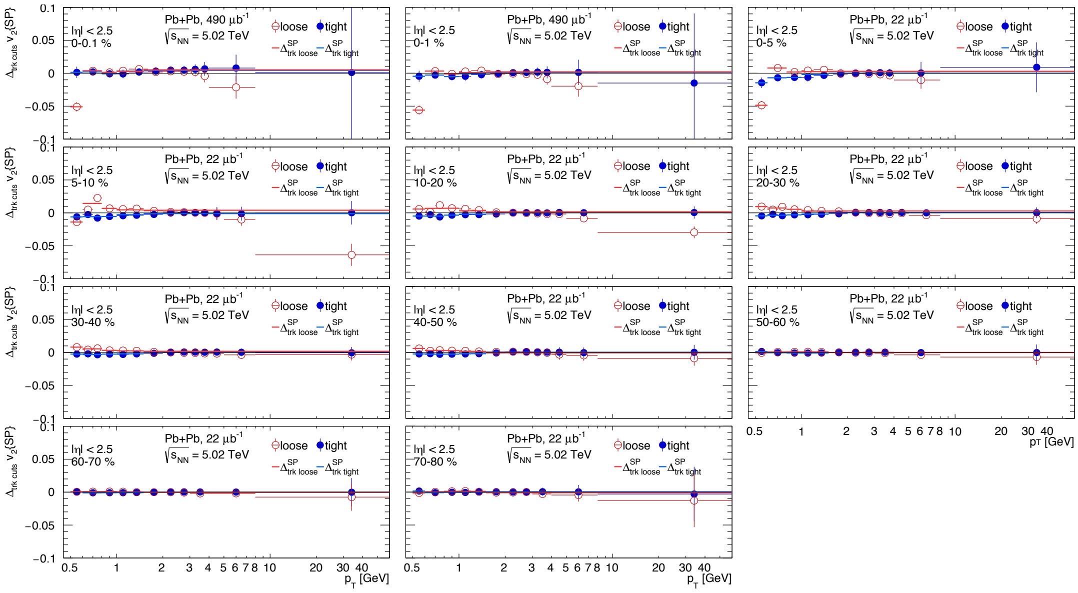

FIGURE 7.3: The relative difference $\Delta_{trkloose}$ (red open points) and $\Delta_{trktight}$ (blue solid points) for v_2 as a function of p_{T} obtained with the SP method. $\Delta_{trkloose}$ and $\Delta_{trktight}$ for merged p_{T} bins are indicated with red and blue lines, respectively.

and $\Delta_{trktight}$ obtained for $v_2\{\mathrm{SP}\}$ as a function of p_{T} in several centrality intervals are shown in Figure 7.3. The largest values of $\Delta_{trk} v_2\{\mathrm{SP}\}$ are observed for the most central collisions at low-p_{T}. This difference decreases for higher p_{T} and more peripheral events. The Δ_{trk} uncertainty for higher order flow harmonics shows similar p_{T} trend and are presented in summary plots in Figures 7.4 and 7.5 for two example centrality bins. To avoid large statistical fluctuations points of high values of p_{T} are merged together. As the systematic uncertainty from this source the larger of the $|\Delta_{trkloose}|$ or $|\Delta_{trktight}|$ is taken point by point, using points after merging. The flow values of v_6 and v_7 are very small and have large statistical uncertainty, thus, such point by point systematic uncertainty estimation for these harmonics is imprecise. Therefore, as the systematic uncertainties for higher order harmonics, v_6 and v_7, ratio of v_n integrated over the full

p_T range is considered. Additionally, for these harmonics, more peripheral events are merged together into wider bins, i.e. for v_6 60–80% and for v_7 40–60% bin is used.

7.2 Tracking efficiency

To account for the effects of the tracking efficiency and fake rate the tracks are weighted by $(1 - f(p_\mathrm{T}, \eta))/\epsilon(p_\mathrm{T}, \eta)$ in each centrality interval. The tracking efficiency is determined with the uncertainty that needs to be propagated to the v_n measurement. Uncertainties in the efficiency result from imprecisions in the detector geometry description in simulations, including uncertainties in the detector material budget. The systematic uncertainty of tracking efficiency is found[1] to be bound within at most 0.04 at different p_T and η. Therefore, the tracking efficiency is varied by the maximum uncertainty of 0.04 according to the formula:

$$\epsilon_\pm(p_\mathrm{T}) = \epsilon(p_\mathrm{T}) \pm 0.04 \frac{\epsilon(p_\mathrm{T}) - \epsilon(p_\mathrm{T}^{up})}{\epsilon(p_\mathrm{T}^{low}) - \epsilon(p_\mathrm{T}^{up})} \tag{7.1}$$

for each η and centrality bin, where $p_\mathrm{T}^{up} = 10$ GeV and $p_\mathrm{T}^{low} = 0.5$ GeV. To assess the systematic uncertainty, the v_n harmonics are measured using $\epsilon_\pm$ and compared to the baseline measurement done with the efficiency obtained from the MC studies. As the systematic uncertainty derived from this source the relative difference between v_n^{base} and $v_n^{\epsilon_+}$ or $v_n^{\epsilon_-}$ is used:

$$\Delta_{\epsilon^\pm}\, v_n = 1 - \frac{v_n^{\epsilon_\pm}}{v_n^{base}} \tag{7.2}$$

For harmonics $v_2 - v_4$ the systematic uncertainty is taken point by point, whereas for higher order harmonics the average absolute ratio integrated over full range of centralities is used. Additionally, the uncertainty for v_7 is averaged over full range of p_T. The $\Delta_{\epsilon^\pm}\, v_n$ is presented in the summary Figures 7.4 and 7.5 for 5–10% and 40–50% centrality intervals.

7.3 Centrality determination

Uncertainty in estimation of the sampling fraction described in Section 4.3, is found to be 1%. To account for this effect, the v_n measurement is repeated with a modified centrality cut on $\Sigma E_\mathrm{T}^{FCal}$ corresponding to 83.5% and 85.5% sampling fractions. Exact values are summarized in Table 4.3. The relative difference between the base measurement and v_n obtained with 83.5% and 85.5% sampling fractions is defined as $\Delta_{84\%} = \frac{v_n^{base} - v_n^{84\%}}{v_n^{base}}$ and $\Delta_{86\%} = \frac{v_n^{base} - v_n^{86\%}}{v_n^{base}}$, respectively. The larger value of $|\Delta_{84\%}|$ and $|\Delta_{86\%}|$ taken point by point is considered as the systematic uncertainty. To avoid large statistical fluctuations for peripheral collisions or for all centralities for higher order harmonics, points are merged together over the full p_T range i.e. the uncertainty is constant in p_T.

---

[1] Determination of the systematic uncertainty of tracking efficiency is not part of this thesis.

7.4 Monte Carlo corrections

The correction due to the MC closure test is at a level of few a percent for the low-p_{T} region in the most central events. The correction, which takes into account additional in-plane tracking inefficiency is used in the flow measurement up to v_5. Due to the limited MC statistics the correction can not be established for small v_n signals of higher order harmonic v_6 and v_7. However, HIJING does not describe the data perfectly, thus, a systematic uncertainty is assigned to the correction. To this end, for the flow harmonics v_2-v_5, the MC closure test is repeated for *HILoose* and *HITight+* tracking selections and the differences $\Delta_{closure} = 1 - \frac{v_n^{reco}}{v_n^{true}}$ are obtained as a function of p_{T}, and compared with the MC closure test for the baseline measurement. As the systematic uncertainty related to the MC correction the larger absolute value of $\left|\frac{\Delta^{loose}_{closure}}{\Delta^{base}_{closure}}\right|$ or $\left|\frac{\Delta^{tight}_{closure}}{\Delta^{base}_{closure}}\right|$ is considered. Such defined uncertainty of the MC correction is then added to the systematic uncertainty on the v_n measurement.

7.5 Residual sine terms

With an ideal detector and with the infinite statistics the imaginary part (sine terms) of equations 5.11 and 5.8, for SP and EP methods should be zero due to symmetry with respect to the reaction plane. In real detector and finite statistics this is not the case. Thus, the relative deviations from zero, $\Delta_{\sin} = \frac{Im\{v_n\}}{v_n^{base}}$, are considered as the uncertainty. Such defined uncertainty is measured for harmonics v_2–v_7 as a functions of p_{T}, η and centrality intervals. The absolute ratio of v_7 harmonics integrated over full p_{T} range is considered as the systematic uncertainty. To get better systematic uncertainty estimation for v_7, the merging is also done in centrality so that two bins of: 0–30% and 30–60% are used.

7.6 Variation of FCal acceptance in the $Q_n^{N|P}$ estimation

The Q_n-vectors are obtained using tower transverse energies measured in the FCal detector. To quantify the impact of the FCal response on the v_n measurement the pseudorapidity range of FCal is divided into two smaller subregions: $3.2 < |\eta| < 4.0$ and $4.0 < |\eta| < 4.8$. The analysis is repeated twice using Q_n-vectors determined in the smaller FCal η-regions. The relative difference between v_n^{base} and v_n obtained using two distinct FCal subregions is defined as $\Delta_{\mathrm{FCal}\{3.2-4.0\}} = \frac{v_n^{base} - v_n^{\mathrm{FCal}\{3.2-4.0\}}}{v_n^{base}}$ and $\Delta_{\mathrm{FCal}\{4.0-4.8\}} = \frac{v_n^{base} - v_n^{\mathrm{FCal}\{4.0-4.8\}}}{v_n^{base}}$. As the systematic uncertainty from this source the larger ratio of $|\Delta_{\mathrm{FCal}\{3.2-4.0\}}|$ or $|\Delta_{\mathrm{FCal}\{4.0-4.8\}}|$) is taken point by point. To avoid large statistical fluctuations some data points are merged (in cases when the merging is performed over the full p_{T} range the systematic uncertainty is just a constant in p_{T}). For each of the two FCal parts, the v_6 and v_7 have rather large statistical uncertainties. However it was observed that statistical fluctuations for v_6 and v_7 harmonics for FCal signal $\{4.0\text{-}4.8\}$ are significantly larger than those for FCal $\{3.2 - 4.0\}$. Therefore, as the systematic uncertainty for these harmonics the difference $\Delta_{\mathrm{FCal}\{3.2-4.0\}}$ is used.

7.7 Residual detector non-uniformity

It is expected that particles produced in a collision are emitted isotropically with respect to $x - y$ plane when averaged over many events. However, due to detector limitations and non-ideal efficiency corrections, the measured flow signal may differ when using only $(\eta < 0)$ or $(\eta > 0)$ hemispheres. The relative difference of the flow signal measured using charged particles with negative (N, $\eta < 0$) and with positive (P, $\eta > 0$) pseudorapidities, $\Delta_{N-P}(\eta) = (v_N(\eta) - v_P(\eta))/v_n^{base}$ is treated as systematic uncertainty. This uncertainty is measured for harmonics $v_2 - v_7$ as a functions of p_T, η and centrality intervals. For more peripheral events or all centralities for higher order harmonics, merging is done for full p_T range i.e. the uncertainty is constant in p_T.

7.8 Systematics summary

The total systematics uncertainty results from uncertainties of all sources added in quadrature. It is presented independently of the statistical one. Table 7.1 quotes uncertainties for all sources in a characteristic p_T and centrality ranges. For the SP harmonics, the summary of systematic uncertainties for each source as well as the total uncertainty as a function of p_T in two centrality classes, 5–10% and 40–50%, is shown in Figures 7.4 and 7.5. The uncertainties of the EP results are very similar to these for SP and are not discussed separately, however they are listed in the Table 7.1.

The contribution from the tracking selection is the most significant at low-p_T in the most central events, typically of the order of 5–10%, as the fake rate is the largest in this region of the phase space. For higher p_T changing the set of tracks used in the analysis have less significant influence on the measurement.

Uncertainties in the efficiency, evaluated by varying the p_T dependence of the tracking efficiency overall is very small and amounts less than 1% in average. It is the largest for v_n harmonics integrated over the whole region of p_T = 0.5–60 GeV, reaching about 0.5%. In narrow p_T intervals uncertainties fluctuate around 0, except of the lowest p_T = 0.5–0.8 GeV bin where it is about 0.3% uncertainty. It does not change significantly neither with centrality nor with the harmonic order.

Influence of centrality binning uncertainty on the measured v_n is largest in the peripheral collisions for which the centrality bin definitions are significantly changed by the procedure. For v_2 a change of ~1% (SP) is observed in the most central events (0–5%) to mid-central events (30–40%). This is because the v_2 changes rapidly with centrality in central collisions and, thus, slight variations in the centrality definition result in a significant variation in v_2.

The systematic uncertainty related to the MC correction is largest, at the level of a few percent, at low-p_T region in the most central events. For $p_\mathrm{T} > 2$ GeV it is less than 0.5–1% depending on the harmonic order.

The contribution from residual imaginary part of v_n is at the level of 1% in most of the phase-space, while for the higher order harmonics, v_5 and v_6, and for very low p_T = 0.5–0.6 GeV in the most central collisions it fluctuates up to about 15%. The ratio $\frac{Imv_7\{\mathrm{SP}\}}{v_7^{base}\{\mathrm{SP}\}}$ vary significantly in p_T bins of lower statistics due to smallness of the v_n values. Therefore, for the v_7 harmonic, the contribution is taken from the integration of the whole p_T region and it is about 20%.

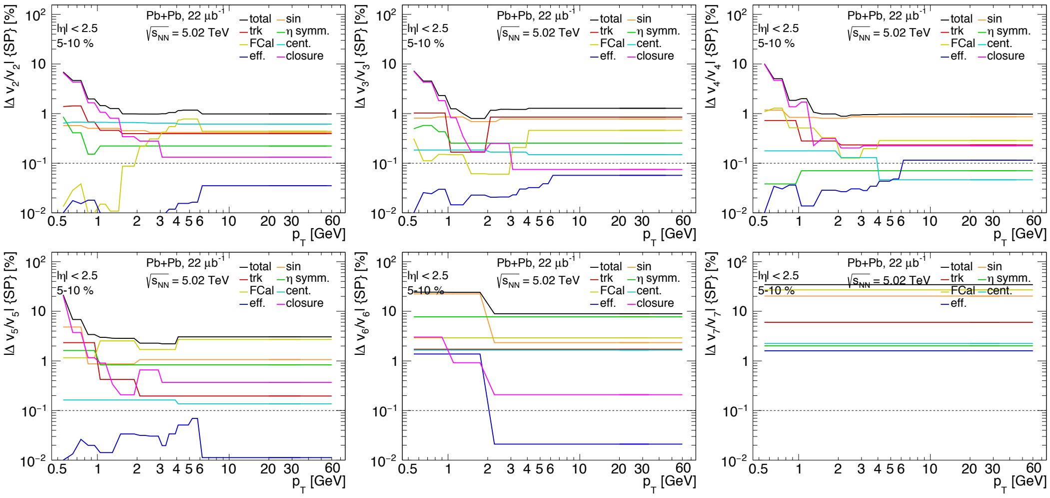

FIGURE 7.4: Summary of systematic uncertainties in 5–10% centrality interval as a function of p_T. Each color corresponds to different source. Each panel shows different harmonic.

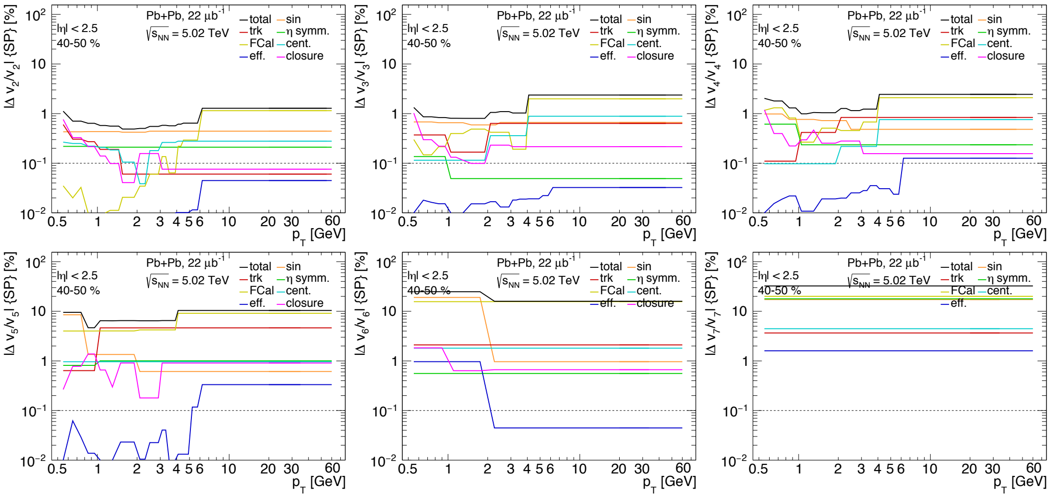

FIGURE 7.5: Summary of systematic uncertainties in 40–50% centrality interval as a function of p_T. Each color corresponds to different source. Each panel shows different harmonic.

Uncertainty arising from the FCal response probed by using FCal subregions is in general small for $p_T < 2$ GeV. For higher p_T the contribution is at the level of a few percent. For v_2 and v_3 it is of the order of about 0.2% but starts growing for higher order harmonics to be ~25% for v_7.

Any difference between the event-averaged v_n at $\pm\eta$ arise from residual detector non-uniformity. This uncertainty is in general very low (at a level of 1%) except for high order harmonics v_6 and v_7. It reaches about 10% for harmonic v_6 in the case of central events, while for v_7 it is at the level of 20%.

Systematic sources	n^{th} harmonic	5–10%		40–50%	
		0.8–1 GeV	9–10 GeV	0.8–1 GeV	9–10 GeV
Track selection	v_2	0.5 (1)	0.5 (<0.5)	<0.5 (<0.5)	<0.5 (<0.5)
	v_3	1 (1)	1 (<0.5)	0.5 (0.5)	0.5 (0.5)
	v_4	0.5 (0.5)	<0.5 (0.5)	<0.5 (<0.5)	1 (1)
	v_5	2 (1)	0.5 (<0.5)	0.6 (0.5)	5 (4)
	v_6	2 (2)		2 (2)	
	v_7	6 (6)		4 (5)	
Tracking efficiency	v_2	0.1 (0.1)		0.1 (0.1)	
	v_3	0.1 (0.1)		0.1 (0.1)	
	v_4	0.1 (0.1)		0.1 (0.1)	
	v_5	0.1 (0.1)		0.1 (0.1)	
	v_6	1 (1)	0.1 (0.1)	1 (1)	0.1 (0.1)
	v_7	1.5 (1.5)		1.5 (1.5)	
Centrality determination	v_2	0.5 (0.5)	0.5 (0.5)	<0.5 (<0.5)	<0.5 (<0.5)
	v_3	<0.5 (<0.5)	<0.5 (<0.5)	<0.5 (<0.5)	0.5 (1)
	v_4	<0.5 (<0.5)	<0.5 (<0.5)	0.5 (0.5)	<0.5 (<0.5)
	v_5	<0.5 (<0.5)	<0.5 (0.5)	1 (1)	1 (1)
	v_6	2 (2)		2 (3)	2 (3)
	v_7	2 (3)		5 (5)	
Residual sine term	v_2	0.5 (0.5)	0.5 (0.5)	0.5 (0.5)	0.5 (0.5)
	v_3	1 (1)	1 (1)	0.5 (1)	0.5 (0.5)
	v_4	1 (0.5)	1 (1)	1 (0.5)	1 (1)
	v_5	1 (0.5)	1 (1)	1 (1)	0.5 (0.5)
	v_6	22 (26)	2 (1)	19 (11)	1 (3)
	v_7	20 (20)		17 (4)	
MC corrections	v_2	2 (2)	<0.5 (<0.5)	<0.5 (<0.5)	<0.5 (<0.5)
	v_3	2 (2)	<0.5 (<0.5)	<0.5 (<0.5)	<0.5 (<0.5)
	v_4	1 (1)	<0.5 (<0.5)	<0.5 (<0.5)	<0.5 (<0.5)
	v_5	1 (1)	<0.5 (0.5)	1 (1)	1 (0.5)
	v_6	3 (3)	<0.5 (0.5)	2 (2)	0.5 (0.5)
	v_7	-	-	-	-
FCal response	v_2	<0.5 (1)	0.5 (1)	<0.5 (0.5)	1 (1)
	v_3	0.5 (0.5)	0.5 (1)	<0.5 (<0.5)	2 (3)
	v_4	1 (2)	<0.5 (<0.5)	1 (1)	2 (2)
	v_5	1 (1)	3 (1)	4 (8)	9 (16)
	v_6	3 (5)		16 (14)	
	v_7	27 (34)		20 (9)	
Detector non-uniformity	v_2	<0.5 (<0.5)	<0.5 (<0.5)	<0.5 (<0.5)	<0.5 (<0.5)
	v_3	0.5 (<0.5)	<0.5 (<0.5)	<0.5 (<0.5)	<0.5 (<0.5)
	v_4	<0.5 (1)	<0.5 (0.5)	0.5 (0.5)	<0.5 (0.5)
	v_5	2 (2)	1 (0.5)	1 (0.5)	1 (0.5)
	v_6	8 (10)		0.5 (2)	
	v_7	2 (3)		18 (14)	

TABLE 7.1: Contributions of the systematic uncertainties associated with the SP and EP (in parentheses) v_n measurements for v_n in 5–10% and 40–50% centrality bins. The contributions are expressed in %.

Chapter 8

Results

The flow harmonics in Pb+Pb collisions at the energy $\sqrt{s_{\mathrm{NN}}}$ = 5.02 TeV are measured using SP and EP methods over an extended transverse momentum range up to p_{T} = 60 GeV, wide pseudorapidity range $|\eta| < 2.5$ and collision centrality 0–80%. Corrections for tracking efficiency and fake rate are applied for integrated distributions $v_n(p_{\mathrm{T}})$, $v_n(\eta)$ and $v_n(N_{\mathrm{part}})$. Results obtained with both techniques are compared to each other. Moreover, the SP method is compared to two-particle correlation method. The comparison to ATLAS results at the lower energy system, $\sqrt{s_{\mathrm{NN}}}$ = 2.76 TeV, to measurements from the CMS experiment as well as to theoretical predictions are also presented. For clarity, this chapter covers the scalar-product results, while the event-plane results are included in Appendix C. The 5.02 TeV Pb+Pb measurements presented in this chapter have been published in Ref. [12].

8.1 The transverse momentum dependence of $v_n\{\mathrm{SP}\}$

The $v_n\{\mathrm{SP}\}$ (n = 2–7) harmonics as a function of transverse momentum are shown in Figure 8.1. Each panel presents a different centrality bin. The integrated luminosity of 0.49 nb^{-1} and 45 μb^{-1} are used for measurements in ultra-central events of 0–0.1% and 0–1%, respectively. The measured v_n in remaining centralities are obtained with the luminosity of 22 μb^{-1} (see sec. 4.1). Results are integrated over $|\eta| < 2.5$. All harmonics show a similar p_{T} trend in all centrality bins. It is understood as originating from the hydrodynamic expansion in the low-p_{T} [91, 92] region and path-length dependent energy-loss at high-p_{T} [93, 94]. The flow signal increases almost linearly up to about 2–3 GeV and then gradually reaches its maximum value at $p_{\mathrm{T}} \cong$ 3–4 GeV. This is followed by a gradual fall of v_n values for higher p_{T}. The magnitudes of the v_n significantly decrease with the harmonic number indicating the harmonics ordering of $v_n > v_{n+1}$. The elliptic flow is a dominant anisotropy, except for the most central bins (0–0.1%, 0–1%, 0–5%). In 0-5% central Pb+Pb collisions the third and fourth harmonic exceed v_2 for p_{T} around 2 GeV, while in 0–0.1% and 0–1% collisions, additionally, the fifth harmonic exceeds v_2 for p_{T} around 4–5 GeV. The geometrical shape of the collision zone is almost ideally spherical in the most central events resulting in small v_2. Thus, higher order harmonics, which reflect the initial geometry fluctuations, become more pronounced. Such behaviour leads to change in the v_n ordering to be $v_3 > v_4 > v_5 \approx v_2$ in this region. The v_2 strongly depends on the event centrality indicating variable shape of the overlap region going from the circular for the most central collisions to the elliptical for mid-central collisions. The strongest elliptic flow is observed in centralities 30–50%, due to the high asymmetries in the initial geometry of the collision shape. Higher-order flow harmonics show weaken centrality dependence. This is expected due to the fact that fluctuations (or eccentricities) of the created medium remain at the similar level for all centralities.

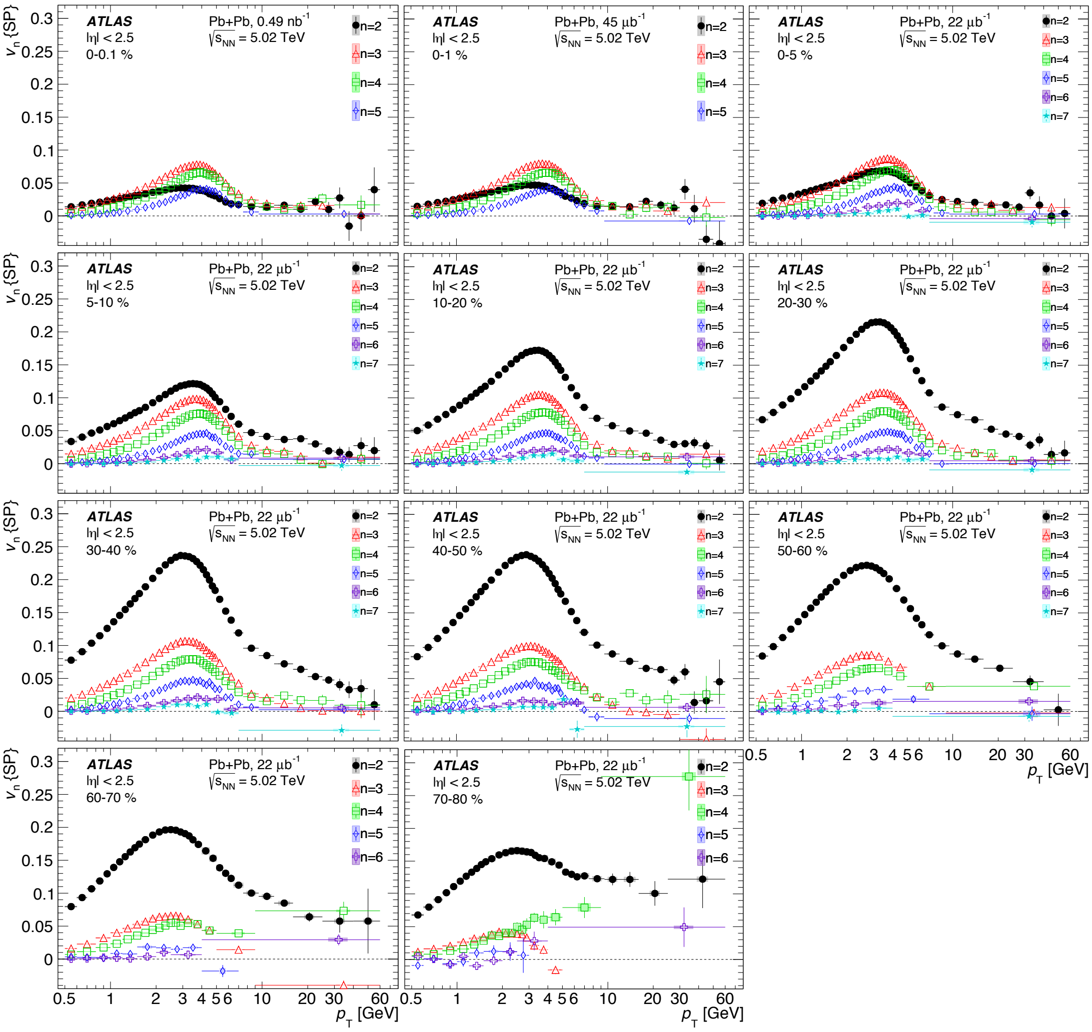

Figure 8.1: The v_n obtained with the SP method as a function of the transverse momentum in 11 centrality intervals integrated over $|\eta| < 2.5$. Due to large statistical fluctuations for higher harmonics the 0–0.1% and 0–1% panels show only v_2–v_5 harmonics. For the same reason the v_7 harmonic is shown for centralities 0–60%. Vertical bars correspond to statistical uncertainties. The shaded boxes indicate systematic uncertainties.

The v_n signals remain significant at high-p_T (p_T > 20 GeV). In particular, the v_2 values persist positive in all centrality intervals even at p_T = 60 GeV. The non-zero v_2 at high-p_T reflects the path-length dependence of high-p_T parton energy-loss in the QCD matter. It is expected that energetic partons experience many successive interactions while traversing hot and dense medium and thus, lose their energy. Such energy loss is dependent on the colour charge density of the created nuclear matter and the path-length of the crossing parton. The overlap region of the heavy-ion collision has an elliptical shape with the short axis in the reaction plane direction. Therefore, the path-length of the parton depends on its azimuthal emission angle relative to the reaction plane. As a consequence, different parton energy-loss (yield) at different azimuthal angle is expected. This mechanism is the foundation for azimuthal anizotropy observed for high-p_T particles.

The v_7 coefficient is measured and presented for the first time. The v_7 signal is very small but the values are non-zero for centrality range 0–50% and are most pronounced in central and mid-central collisions at p_{T} = 2–4 GeV.

8.2 The pseudorapidity dependence of $v_n\{\mathrm{SP}\}$

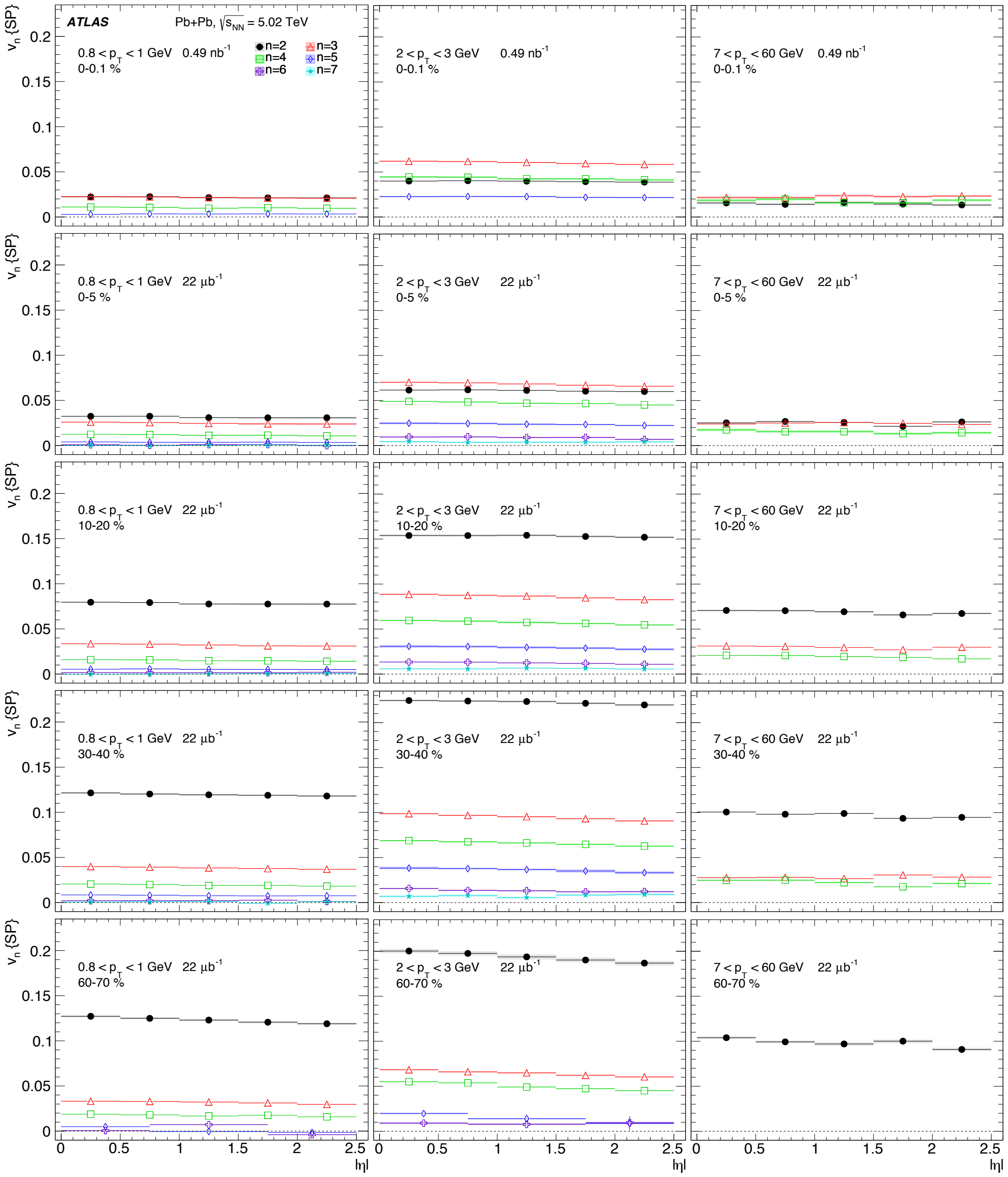

FIGURE 8.2: The v_n obtained with the SP method as a function of $|\eta|$ for three p_{T} slices: 0.8–1 GeV, 2–3 GeVand 7–60 GeV in five centrality bins: 0–0.1%, 0–5%, 10–20%, 30–40% and 60–70%. Vertical bars correspond to statistical uncertainties. The shaded rectangles indicate systematic uncertainties.

The v_n (η) distribution is observed to be symmetric with respect to $\eta = 0$. Therefore, the v_n pseudorapidity dependance is folded into the η range of η = 0–2.5. The v_n $(|\eta|)$ is defined as the average of v_n values in positive and negative η bins weighted by corresponding number of tracks. The scalar-product v_n results (n =2–7) as a function of $|\eta|$ are shown in Figure 8.2 for the three p_T regions: low $0.8 < p_T < 1$ GeV, intermediate $2 < p_T < 3$ GeV and high $7 < p_T < 60$ GeV and five centrality intervals: 0–0.1%, 0–5%, 10–20%, 30–40% and 60–70%. The $v_n(|\eta|)$ distribution is almost uniform within the statistical and systematical uncertainties for most of centrality and p_T intervals and harmonics. However, in some cases the difference between v_n values at $\eta = 0$ and $\eta = 2.5$ is not negligible. In central and mid-central collisions (0–40%) at low $p_T < 3$ GeV the v_2 ($\eta = 0$) is approximately 2–4% larger than v_2 ($\eta = 2.5$). For peripheral collisions and $p_T > 7$ GeV this difference is more pronounced reaching about 10%. The v_3 and v_4 harmonics drop by about 10% in central and mid-central collisions for p_T = 2–3 GeV. In peripheral collisions the drop is about 15% and 25% for v_3 and v_4, respectively.

8.3 The number of participants dependence of $v_n\{\mathrm{SP}\}$

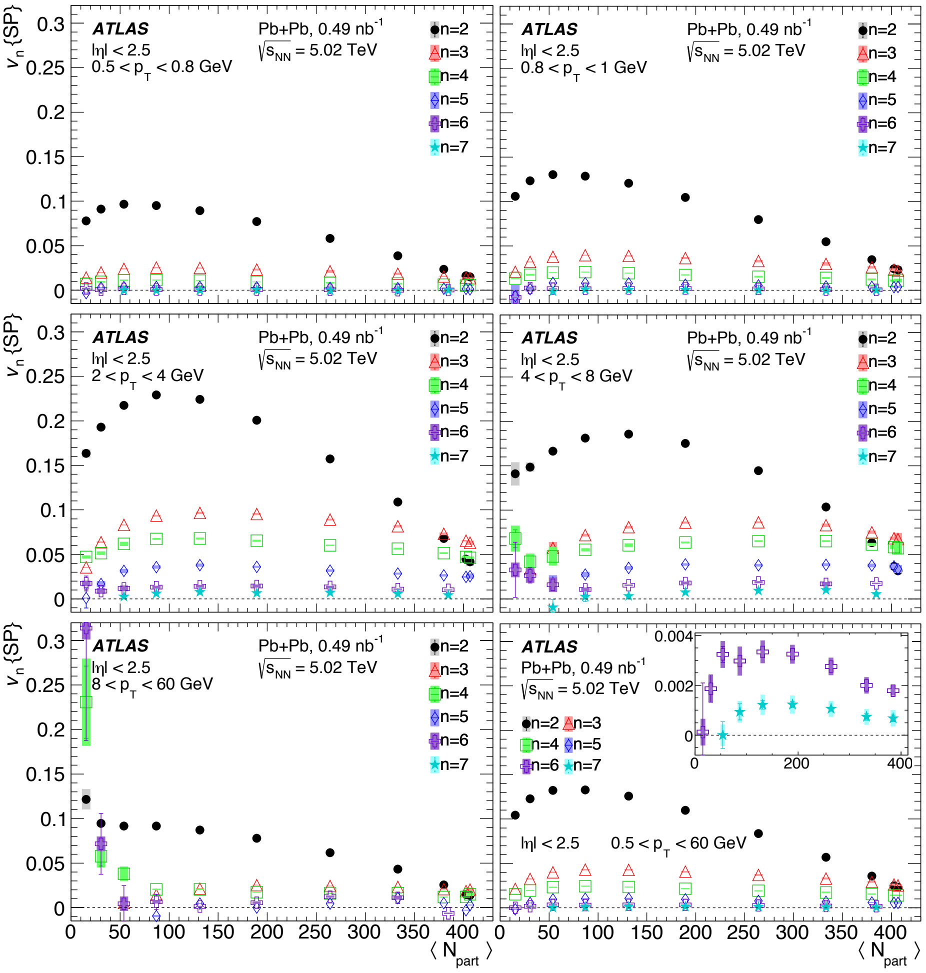

FIGURE 8.3: Integrated v_n vs. N_{part} for six p_T ranges as indicated in the legend extracted from the SP method. Bottom right panel correspond to results integrated over the full range of measured p_T. The inset panel shows the v_6 and v_7 harmonics with adjusted scale. Vertical bars correspond to statistical uncertainties. The shaded rectangles indicate systematic uncertainties.

Figure 8.3 shows the N_{part} dependence of v_n integrated over broad p_{T} ranges and $|\eta| < 2.5$. Results integrated over the full p_{T} range are also presented. Integration procedure is described in section 5.2.4. The v_2 harmonic significantly varies with N_{part}. It is dominant anisotropy except for the most central collisions - indicated by the three points at largest N_{part} ($N_{\text{part}} \gtrsim 350$). Going from central to peripheral events (from right to left along the x-axis), the v_2 first increases, reaching a maximum in the 30–50% centrality range ($N_{\text{part}} \approx 70$–$110$), and then it decreases. The higher-order harmonics v_3–v_4 show similar but much weaker trend. The v_5–v_7 coefficients show almost no centrality dependence.

8.4 The scalar-product and event-plane methods comparison

The scalar-product method always measures $\sqrt{\langle v_n^2 \rangle}$ independently of the resolution correction. In the event-plane method the same resolution correction is applied for all events in a centrality class. In reality, the reaction plane resolution depends on the multiplicity of particles used to define the event-plane angle and the magnitude of the anisotropy v_n. The multiplicity may vary significantly within a centrality bin, depending on the size of the interval. Consequently, the v_n measured with the event-plane method does not estimate the $\sqrt{\langle v_n^2 \rangle}$ but the quantity in between $\langle v_n \rangle$ and $\sqrt{\langle v_n^2 \rangle}$ in a detector dependent manner. The results obtained from the scalar-product measurements can be directly compared between different experiments, while comparison of the event-plane results can be ambiguous [87]. The elliptic flow, v_2 estimated with the scalar-product method are expected to differ (be larger) by a few percent from the measurements obtained with the event-plane method for events with high resolution (R close to 1). In low resolution limit (higher flow harmonics or peripheral collisions), both methods are expected to result in compatible estimates [87]. Figure 8.4 shows the v_n results obtained with the SP and EP methods as a function of p_{T} for three centrality intervals: 0–5%, 20–30% and 40–50%. Each panel corresponds to different harmonic order, except for bottom right plot which shows all harmonics as a function of N_{part} integrated over $p_{\text{T}} = 0.5$–60 GeV. This effect is the most pronounced for the second harmonic. The bottom subpanels show corresponding ratio $\frac{v_n\{SP\}}{v_n\{EP\}}$. The v_2 values obtained with the SP method are larger than those obtained from the EP method by about 1% in central and about 2-3% in mid-central and peripheral collisions. For v_3 the difference between SP and EP results is about 0.5–1% in central and mid-central events and is negligible in peripheral collisions. For the v_4, v_5 and v_6 both methods are comparable within ±0.5%.

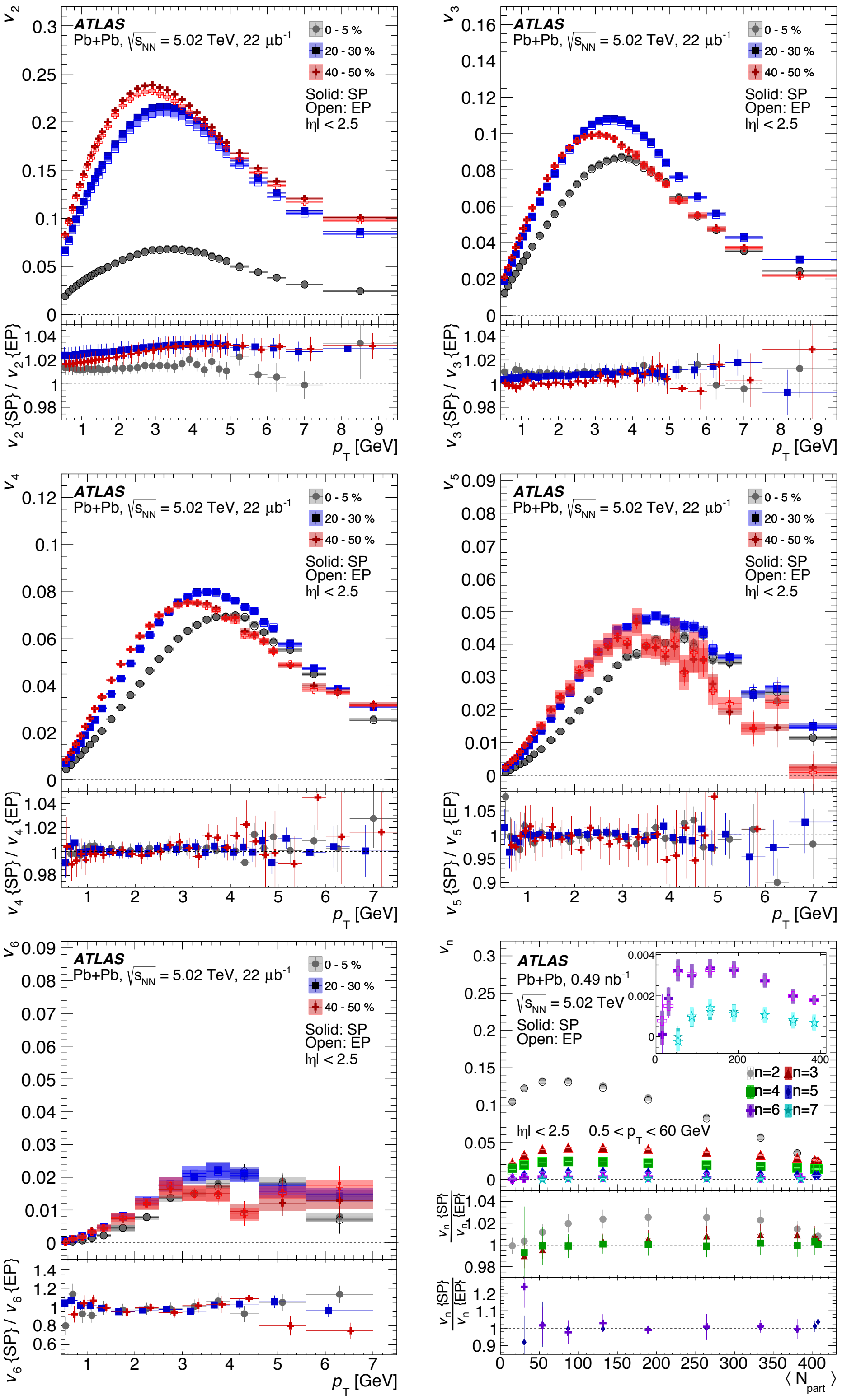

FIGURE 8.4: Comparison of the v_n obtained with the EP and SP methods as a function of p_T in three centrality bins: 0–5%, 20–30% and 40–50%. The right bottom panel shows the v_n as a function of N_{part}, integrated over $0.5 < p_T < 60$ GeV. In the inset the v_6 and v_7 integrated over $0.5 < p_T < 60$ GeV are shown with adjusted scale. The vertical bars indicate the quadrature sum of statistical and systematical uncertainties.

8.5 The scalar-product and two-particle correlation methods comparison

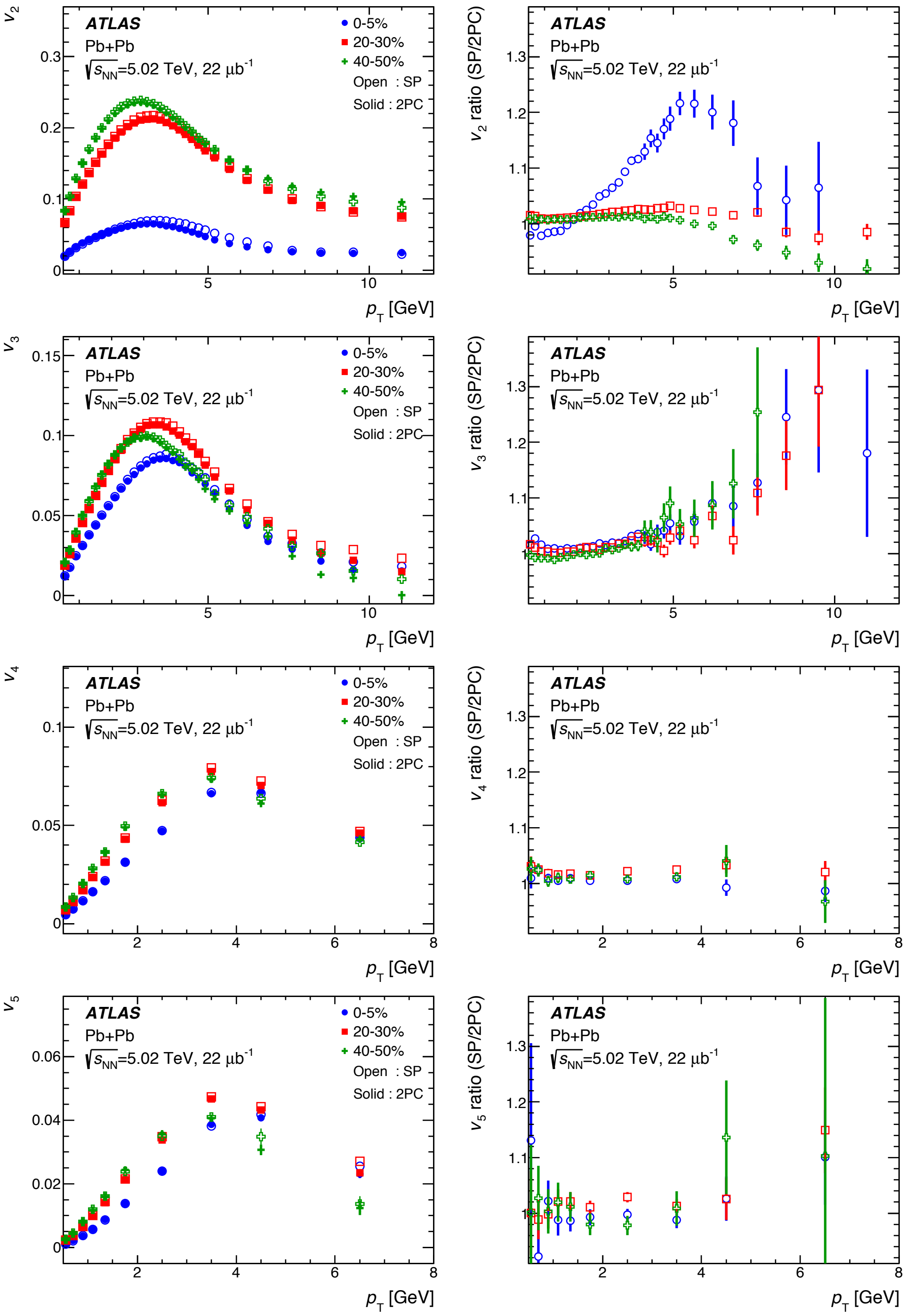

FIGURE 8.5: Comparison of the v_n obtained with the 2PC and SP methods as a function of p_T. Each panel shows the comparison for a different order harmonic. The comparisons are shown for three different centrality intervals: 0–5%, 20–30% and 40–50%. The vertical bars indicate statistical uncertainties only.

The two-particle correlation method (2PC) is another method commonly used in studying flow harmonics [51]. The 2PC results presented below are complementary to the SP measurements. The 2PC measurement[1] was performed in parallel to the main subject of the presented work using the same datasets and has been also published in Ref. [12]. The 2PC function is constructed from the correlation between two particles in relative azimuthal angle $\Delta\phi = \phi_a - \phi_b$ and pseudorapidity $\Delta\eta = \eta_a - \eta_b$. The $\Delta\phi$ distribution is expanded into a Fourier series, similarly to single particle distribution in Eq. 2.2.

$$\frac{dN_{pairs}}{d\Delta\phi} \propto 1 + 2\sum_n v_{n,n}(p_{\mathrm{T}}^a, p_{\mathrm{T}}^b)\cos(n\Delta\phi),$$

where $v_{n,n}$ corresponds to p_{T}^a and p_{T}^b dependent Fourier pair harmonics. The particles are denoted as particle 'a' and particle 'b' corresponding to the *reference* and *associate* particle, respectively. The $v_{n,n}$ is expected to factorize as $v_{n,n} = v_n(p_{\mathrm{T}}^a)v_n(p_{\mathrm{T}}^b)$ if the anisotropy is driven by the collective expansion. Then, the anisotropy flow harmonics for a single particle is obtained as:

$$v_n(p_{\mathrm{T}}^a) = v_{n,n}(p_{\mathrm{T}}^a, p_{\mathrm{T}}^b)/\sqrt{v_{n,n}(p_{\mathrm{T}}^b, p_{\mathrm{T}}^b)}. \tag{8.1}$$

Figure 8.5 shows the comparison between the SP and 2PC measurements. The results are presented in three centrality intervals: 0–5%, 20–30% and 40–50% for harmonics v_2-v_5. Overall, both techniques give quite similar v_n values. However, some discrepancies are observed. In particular, the $v_2\{\mathrm{SP}\}$ harmonic gives larger values than 2PC v_2 in 0–5% centrality and at $p_{\mathrm{T}} > 2$ GeV. For $p_{\mathrm{T}} < 2$ GeV the $v_2\{\mathrm{SP}\}$ is smaller than $v_2\{\mathrm{2PC}\}$ by about 2%. In more peripheral collisions v_2 obtained using both methods match within 2–5% for $p_{\mathrm{T}} \lesssim 10$ GeV. The differences between methods are less prominent for higher order flow harmonics. The harmonics v_3-v_5 within 4%.

Both methods measure the same quantity of $\sqrt{\langle v_n^2\rangle}$ and thus, the $v_n\{\mathrm{SP}\}$ should be equal to $v_n\{\mathrm{2PC}\}$. However, some systematic differences in the v_n measurement in both methods are expected due to a breakdown of factorization (Eq. (8.1)). The studies on factorization breakdown effect have shown that it is most prominent for the v_2 in central events, where the v_2 is small and the initial-state fluctuations become the primary source of anisotropy [95]. The breakdown is also observed at high-p_{T} irrespectively of the harmonic order. One more difference that may lead to the differences between SP and 2PC results is in the η separation used to remove short-range correlations like: jet fragmentation, resonance decays or Hanbury Brown and Twiss corerlations. In the SP method the $\Delta\eta$ gap between the FCal reference flow and the tracks is chosen to be larger than 3.2 units in η, while in the 2PC method the gap is $|\Delta\eta| > 2$.

8.6 Comparison to Pb+Pb results at $\sqrt{s_{\mathrm{NN}}} = 2.76$ TeV

Figure 8.6 shows the v_2–v_6 as a function of p_{T}, obtained in the event-plane method using Pb+Pb data at $\sqrt{s_{NN}} = 2.76$ TeV and $\sqrt{s_{NN}} = 5.02$ TeV. The comparison is presented for 0–5%, 20–30% and 40–50% centralities and results are integrated over pseudorapidity region of $|\eta| < 2.5$. The $\sqrt{s_{NN}} = 2.76$ TeV Pb+Pb analysis [51] was

---

[1] 2PC results for Pb+Pb are not part of the PhD thesis - only used for comparison with the SP v_n.

performed with slightly modified event-plane method, which uses full-FCal to estimate event-plane angles. The full-FCal method combines N-side and P-side of FCal thus reducing the η separation between tracks and the event-plane detector. As a result the full-FCal method is more sensitive to non-flow correlations. Moreover, the MC non-closure correction was not applied in the $\sqrt{s_{NN}} = 2.76$ TeV measurement. Despite the above differences in the measurement technique details, the v_n results at the two energies are almost consistent within statistical and systematical uncertainties. The conclusions are in agreement with the ALICE statement that the differential v_n measurements are consistent at the two collision energies [57].

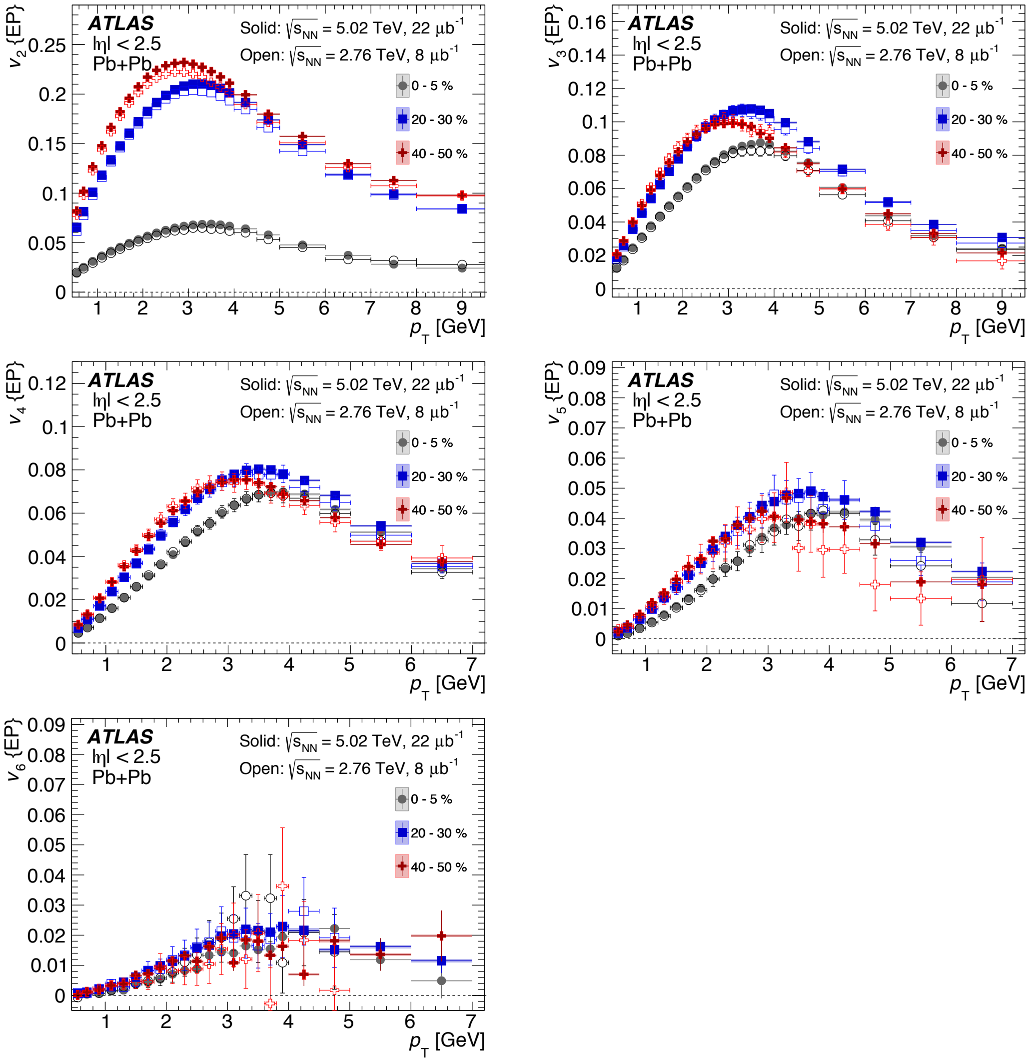

FIGURE 8.6: Comparison of the v_n obtained with the EP method in Pb+Pb collisions at the energy $\sqrt{s_{\mathrm{NN}}}$ = 2.76 TeV and $\sqrt{s_{\mathrm{NN}}}$ = 5.02 TeV as a function of p_{T}. The results are shown in three centrality bins: 0–5 %, 20–30% and 40–50%. The vertical bars indicate statistical uncertainties. The shaded boxes indicate systematic uncertainties.

8.7 Comparison to Xe+Xe results at $\sqrt{s_{\mathrm{NN}}}$ = 5.44 TeV

In October 2017 LHC performed Xe+Xe collisions at a centre-of-mass energy per nucleon-nucleon of $\sqrt{s_{\mathrm{NN}}}$ = 5.44 TeV. The Xe+Xe is an interesting system to measure v_n since the ions of xenon are almost twice smaller than lead ions which introduce larger spatial variations. Generally, such system is expected to have larger event-by-event fluctuations in the initial geometry (see Figure 2.5) than the Pb+Pb system and thus, to enhance the spatial deformation of the overlap region and thus higher the observed flow. At the same time, the effect of increase maybe compensated by the viscous effects which are expected to weaken the flow signal [96]. The results of the presented work are compared with the recent ATLAS $\sqrt{s_{\mathrm{NN}}}$ = 5.44 TeVXe+Xe results [20]. The Xe+Xe flow measurement is a "twin" analysis to the work in the presented thesis. The v_n were obtained using three methodologies: the SP method, the 2PC method and the cumulant method. The later is not discussed here.

Figure 8.7 shows the v_2–v_5 harmonics as a function of p_{T} in three centrality intervals: 0–5%, 20–30% and 50–60%, measured with the SP method. The typical p_{T} dependence of the v_n is observed in Xe+Xe collisions: first the almost linear increase up to 2–3 GeV followed by the gradually reached maximum at p_{T} = 3–4 GeV and then gradual fall for higher p_{T}. The measurements are presented in p_{T} range of p_{T} = 0.5–20 GeV. The v_2 is found to be dominant in all centrality classes except of the most central collisions. The v_3 is observed to be larger than v_2 for p_{T} = 3–5 GeV in 0–5% centrality interval.

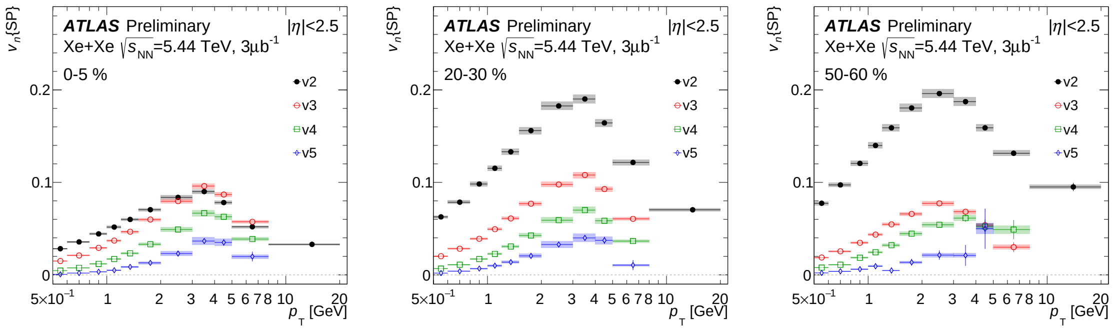

FIGURE 8.7: The v_n (p_{T}) for n = 2–5 measured with SP method at $\sqrt{s_{\mathrm{NN}}}$ = 5.44 TeV collisions in three centrality intervals: 0–5%, 20–30% and 50–60%. Vertical bars correspond to statistical uncertainties, while systematic uncertainties are indicated by shaded areas.

The comparison of the Pb+Pb results [16], which are preliminary to those presented in this thesis, to Xe+Xe v_n harmonics is shown in Figure 8.8. The v_n harmonics are integrated over the p_{T} range of p_{T} = 0.5–5 GeV and are shown as a function of centrality and the number of participants. In general, over the full centrality range the matching of v_n is quite good between both systems. This consistency implies that the flow is derived from the initial shape of the produced QGP fireball rather than fluctuations of the number of participants in the initial state of a collision. However, the Xe+Xe v_2 values are markedly larger than for Pb+Pb collisions in the most central events. This behaviour is expected due to the larger initial fluctuations present in the lighter collision system. The fluctuations have an impact on the initial collision geometry, and thus, with the increased fluctuations component the v_n is enhanced in Xe+Xe system.

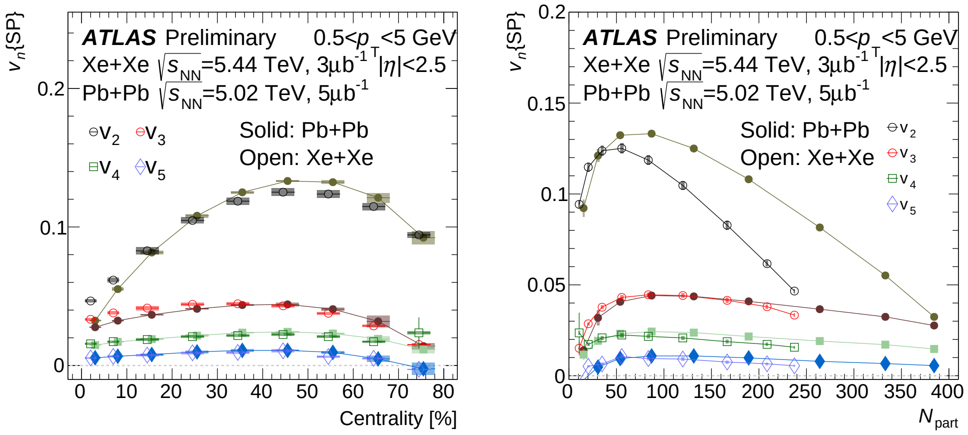

FIGURE 8.8: The v_2–v_5 harmonics measured with the SP method in Pb+Pb and Xe+Xe collisions. Left: as a function of centrality percentile. Right: as a function of N_{part}. Results are integrated over p_{T} = 0.5–5 GeV and $|\eta| < 2.5$.

On the other hand, for mid-central and peripheral collisions the Xe+Xe v_2 coefficient is observed to be consistently smaller than those in Pb+Pb collisions. This trend is explained using expectations from hydrodynamic models. The viscous effects, which suppress the v_n values, are larger for the smaller, Xe+Xe, system. The reduction of v_n is more pronounced with decreasing centrality and increasing harmonic order compared to the Pb+Pb. Furthermore, the differences between Pb+Pb and Xe+Xe collision systems might be explained by a quadrupole deformation of the xenon ion [96]. For the higher order flow coefficients the effect in most central events is less pronounced.

8.8 Comparison to CMS results

Figure 8.9 shows the measurement of SP v_2 and v_3 harmonics integrated over $|\eta| < 1$ as a function of p_{T} compared to results obtained by the CMS experiment at the same collision energy [58] in four centrality intervals: 0–5%, 10–20%, 30–40% and 50–60%. The values of p_{T} given by the CMS are the mean p_{T} within the bin in which the v_n values are measured, while the results obtained in the presented work are shown for p_{T} at the center of the bin. The results from the two experiments agree well, although with some differences, which are larger than the uncertainties. The comparison is plausible only for p_{T} between 1 GeV to about 12 GeV due to statistical fluctuations for higher p_{T}. The presented v_2 values are smaller than measured by CMS at most by about 5%, while the differences for v_3 are larger and reaching ~ 6–7% in the specified p_{T} region. However, the two analyses differ in some details:

- Presented analysis is based on so-called 2-subevent setup for the resolution factor, while the CMS is using 3-subevent expression. The SP definition in CMS is then slightly modified:

$$v_n\{SP\} = \frac{\langle Q_n Q_{nA}^{*} \rangle}{\sqrt{\frac{\langle Q_{nA} Q_{nB}^{*} \rangle \langle Q_{nA} Q_{nC}^{*} \rangle}{\langle Q_{nB} Q_{nC}^{*} \rangle}}}, \text{ with } Q_n, Q_{nA}, Q_{nB}, Q_{nC} = \sum_{k=1}^{M} \omega_k e^{in\phi_k} \tag{8.2}$$

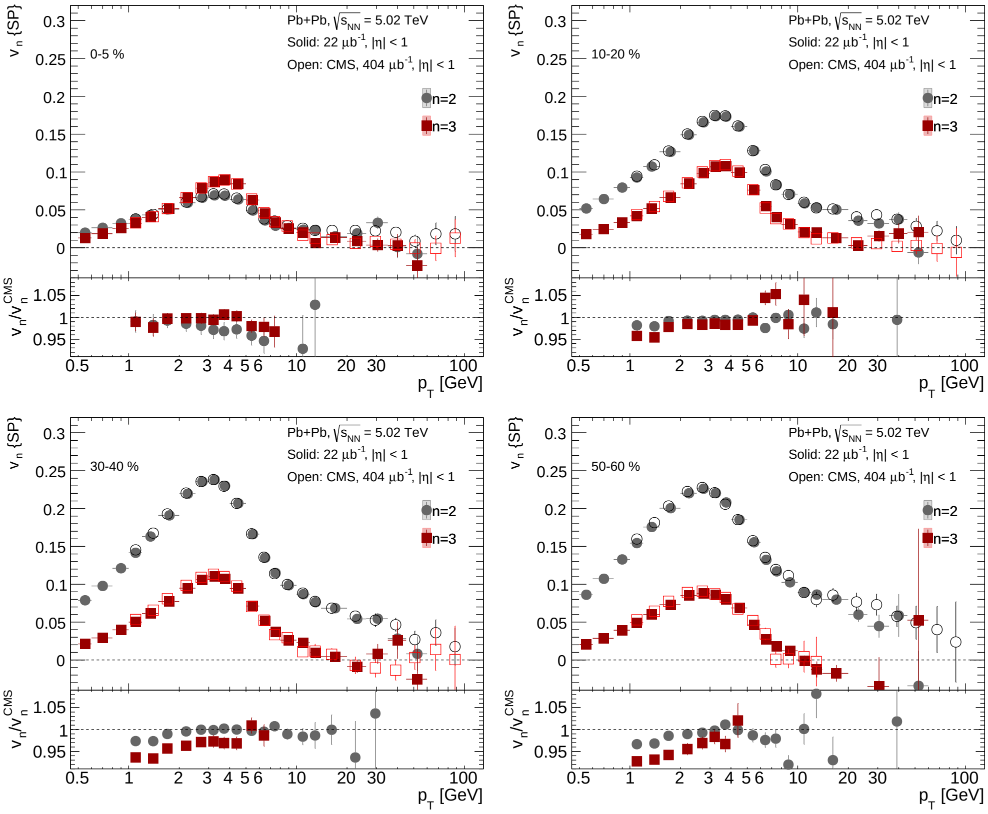

FIGURE 8.9: The v_2 and v_3 results compared with the CMS measurement obtained with the SP method as a function of p_{T}. The comparison is presented in four centrality bins: 0–5%, 10–20%, 30–40% and 50–60%. Vertical bars represent the statistical and systematical uncertainties combined. Ratios are shown at the bottom of each panel.

where M represents the number of tracks or E_{T} deposited in hadron forward (HF) calorimeter towers, the ϕ_k is the azimuthal angle of k-th track or tower and the ω_k is a weight equal to unity for Q_n, p_{T} for the Q_{nC} and E_{T} for Q_{nA} and Q_{nB}. The Q_n vector is based on particles of interest, i.e. tracks with $|\eta| < 1$. The Q_{nA} and Q_{nB} vectors are determined from the two HF calorimeters. The Q_{nC} vector is obtained using tracks in $|\eta| < 0.75$. The Q_{nA} is calculated using the negative-η side of HF when particles of interest comes from positive-η side of the tracker and vice versa. The denominator is modified to use an additional subset of tracks for $|\eta| < 0.75$ with the p_{T} weighting, combined with the positive and negative sides of HF calorimeters. Both, ATLAS and CMS approaches, lead to the same results in the case of "idea" factorization of two-particle correlations functions. In reality the factorization is slightly broken, and therefore the two methods may lead to slightly different results on v_n.

- ATLAS FCal and CMS HF may be sensitive to different kinematical ranges of p_{T} particles hitting the detector. The effect may also lead to different results on v_n due to the factorization problem mentioned above.
- CMS uses a different pseudorapidity gap between HF and the Inner Tracker which amounts to 2.9 units. Presented analysis uses 3.2 units. Therefore, slightly

different impact from non-flow effects, like jets, resonance decays or energy conservation is expected in both measurements.

8.9 Comparison to theoretical predictions

The v_n coefficients measured with the SP method are compared to the theoretical calculations in two relevant p_{T} regions: low- and high-p_{T} to study the hydrodynamics effects and the path-length dependence of the parton energy-loss, respectively.

The comparison at low-p_{T}, relevant for hydrodynamic models, is presented in Figure 8.10. The v_2-v_4 coefficients obtained using 5.02 TeV Pb+Pb data are shown as a function of p_{T} for the range from 0.5 to 2 GeV, in the 0–5% and 30–40% centrality intervals. The results are integrated over pseudorapidity range of $|\eta| < 1$. The charged hadron $v_n\{\mathrm{SP}\}$ are obtained using a hydrodynamic and hadronic cascade hybrid simulations [92]. In this approach the initial state of heavy-ion collision is generated using the IP-Glasma model. Then, the medium evolution is handled by the relativistic viscous hydrodynamics. Finally, the system is passed through the hadronic cascade generation procedure. Generally, the predictions are consistent with the data for low p_{T} $\lesssim$ 1 GeV in central and mid-central collisions, but the v_n are overestimated for higher p_{T}. In the 0–5% centrality the theoretical calculations describe the data within about 5–10% up to p_{T} = 1 GeV for the v_2 and up to p_{T} = 1.4 GeV for v_3 and v_4. For higher p_{T} the discrepancy between theory and data is larger and amounts approximately 25–30% for all v_n coefficients. For the 30–40% collisions the agreement is restricted to lower p_{T}. The 5%-consistency is observed only up to 0.8 GeV for v_2 and up to 1 GeV for higher order coefficients. At higher p_{T} the theory calculations overestimate the v_n by approximately 30–35%.

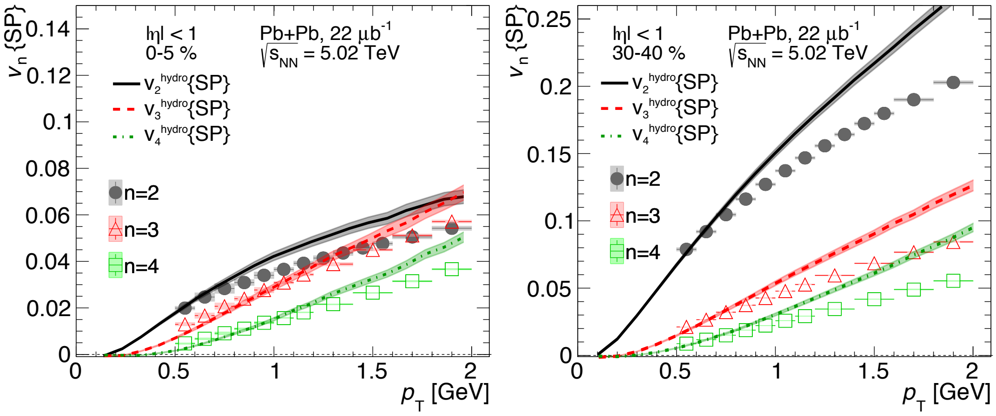

FIGURE 8.10: The differential $v_n(p_{\mathrm{T}})$ compared with the theoretical calculations for n = 2–4 in 0–5% and 30–40% centrality intervals in Pb+Pb collisions at 5.02 TeV from Ref. [92].

The v_2 and v_3 results at high-p_{T} compared to the CUJET3.0 [97] and SHEE [94, 98] models for 0–5% and 30–40% centrality bins are shown in Figure 8.11. The comparison is done for p_{T} > 5 GeV. The CUJET3.0 is a jet quenching framework constructed from the perturbative QCD calculations and semi-QGP model. In this model, the hard parton interactions in the QGP are described using perturbative QCD calculations, which are complemented by a perfect-fluid hydrodynamic evolution of the overlap region. The

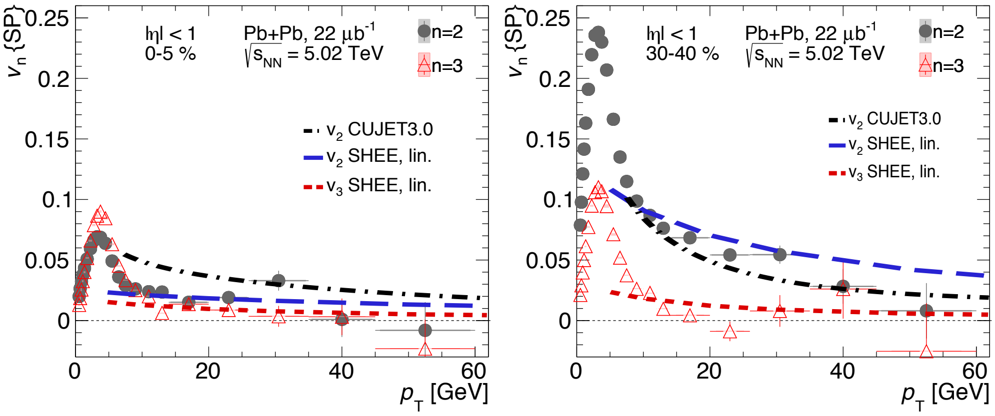

FIGURE 8.11: The differential v_n (p_T) compared with the theoretical calculations for n = 2–3 in 0–5% and 30–40% centrality intervals in Pb+Pb collisions at $\sqrt{s_{NN}}$ = 5.02 TeV made with the CUJET3.0 [97] and the SHEE models [94, 98].

semi-QGP model is used to describe the QCD at temperature $T \rightarrow T_C$. The SHEE framework (Soft-Hard Event Engineering) is designed to combine the soft event-by-event fluctuations generated with viscous hydrodynamics [94, 99] with a jet energy loss model [94, 100]. The calculations are implemented with a low $\eta/s \leq 0.12$ ratio, a chemical freeze-out temperature of 160 MeV and a linear path-length dependence of the jet energy loss based on perturbative QCD. The main difference between both models is that CUJET3.0 uses smooth hydrodynamic background, while the SHEE introduces the fluctuations in the initial geometry of a collision.

In the 0–5% centrality bin the CUJET3.0 calculations overestimate the v_2 data results by about 30%. The agreement is better for the 30–40% centrality where the data and predictions match within 5%. Nevertheless, the CUJET3.0 model qualitatively describes the p_T-trend of the v_2 at $p_T > 10$ GeV in both centralities. The SHEE predictions are presented for v_2 and v_3. They are quantitatively consistent with data within a few percent in both centralities. This agreement implies that introducing the initial-state fluctuations into the hard parton energy-loss model is important to accurately describe the experimental data.

Chapter 9

Conclusions

In this thesis comprehensive studies of azimuthal anisotropies of charged particle distributions in Pb+Pb collisions at $\sqrt{s_{\mathrm{NN}}}$ = 5.02 TeV performed using data from the ATLAS experiment at the LHC are presented. The measurement is based on the minimum-bias Pb+Pb sample with an integrated luminosity of 22 $\mu\mathrm{b}^{-1}$. In addition, the statistics in the ultra-central collisions, i.e. 0–1% and 0–0.1% centralities, are enhanced to 45 $\mu\mathrm{b}^{-1}$ and 0.49 nb^{-1}, respectively. The Fourier harmonic amplitudes v_n are determined for $n = 2$–7 using SP and EP methods in a broad transverse momentum (p_{T} = 0–60 GeV), pseudorapidity ($|\eta| < 2.5$) and centrality (0–80%) phase space. Precise measurements of the higher order harmonics, sensitive to fluctuations in the initial state, are also presented. The high-statistics Pb+Pb sample allows for a detailed study of the azimuthal anisotropy. In particular, v_2–v_5 coefficients are obtained in the ultra-central collisions in a wide range of p_{T} up to 60 GeV. Furthermore, the measurement of the v_7 harmonic is presented for the first time.

Both, SP and EP methods are based on the event-plane angle and flow vector distributions. To suppress any biases due to detector effects the Ψ_n and Q_n vector modulations measured in the FCal were calibrated using a two-steps correction procedure. Such an approach provides full uniformity in Ψ_n and Q_n vector distributions needed for precise v_n measurements.

The MC cross-check analysis was performed in parallel to the real data measurement which utilized 4M HIJING events. The MC studies revealed the difference between reconstructed v_n^{reco} values and generated v_n^{true} values in the most central collisions (0–40%) at low p_{T} (< 2 GeV). The investigation of the MC sample indicated two sources of such MC non-closure. There were the reconstruction inefficiency correlated with the event-plane direction and the high rate of fake tracks in the aforementioned phase space regions. As the origin of the MC non-closure was fully understood the real data results were corrected accordingly. The correction uncertainty was evaluated and added to the total systematic uncertainty.

The v_n harmonics, measured with both SP and EP methods, show the same trend of p_{T} dependence in all centrality bins. The v_n values increase with the p_{T} reaching the maximum at p_{T} = 3–4 GeV and gradually decrease for higher p_{T}. However, the $v_2(p_{\mathrm{T}})$ remains positive even at the highest measured p_{T} = 60 GeV, which is attributed to the parton energy-loss in the QCD matter. The second-order harmonic is the main source of the anisotropy except for 0–5% centralities where higher harmonics dominate. This is due to the initial geometry of the collision zone. The interaction region in a non-central collision has an elliptical shape leading to large elliptic flow values. In the most central collisions the interaction zone has a spherical shape resulting in relatively small v_2 in comparison to values of higher order flow harmonics. The ordering of flow harmonics observed in mid-central and peripheral collisions, i.e. $v_n > v_{n+1}$, is modified to $v_3 > v_4 > v_5 \approx v_2$ for the most central collisions at p_{T} around the v_n peak. The v_n harmonics have weak $|\eta|$ dependence. The exceptions are seen for v_2 in central and mid-central collisions at $p_{\mathrm{T}} < 3$ GeV as well as in peripheral collisions at $p_{\mathrm{T}} > 7$ GeV, where the difference between $v_2(|\eta| = 0)$ and $v_2(|\eta| = 2.5)$ is about 2–4% and 10%, respectively. For v_3 and v_4 in central and mid-central collisions at $p_{\mathrm{T}} = 2$–3 GeV the variation is observed to be about 10%, while in peripheral collisions about 15% and 25% for v_3 and v_4, respectively. The centrality dependence of integrated v_n is examined as a function of the number of nucleons participating in Pb+Pb collisions, N_{part}. The largest anisotropies are observed in mid-central collisions, i.e. $N_{\mathrm{part}} = 70$–110, for the v_2 harmonic. The v_2 simultaneously shows the most prominent dependence with the collision centrality as the initial elliptical geometry significantly varies from central to peripheral collisions. The N_{part} trend is much weaker for higher order harmonics, which indicates that the fluctuations present in the created medium for higher order modes are of similar magnitude for all centralities. Large statistics utilized in presented analysis allow for the measurement of the v_7 coefficient, which is found to be non-zero for centralities 0–50%.

The v_n harmonics obtained with SP and EP methods are consistent within ±0.5–1% for $n \geq 3$. The second order flow harmonic values measured with the SP method are systematically larger than those measured with the EP method by 1% in central and 2–3% in mid-central and peripheral events. Such differences are expected as the v_n measured with the EP method depends on the detector acceptance, while the SP method gives a well-defined measurement regardless the detector resolution.

The v_n harmonics obtained with the SP method are also compared with values measured with the complementary 2PC method. Both methods measure the same quantity of $\sqrt{\langle v_n^2 \rangle}$ and, thus, give consistent results up to $p_{\mathrm{T}} \sim 10$ GeV. However, due to factorization breakdown some systematic differences between $v_n\{\mathrm{SP}\}$ and $v_n\{2\}$ are expected. In particular, in the most central collisions at $p_{\mathrm{T}} < 2$ GeV the $v_2\{\mathrm{SP}\}$ is observed to be smaller than the $v_2\{\mathrm{2PC}\}$, while at $p_{\mathrm{T}} > 2$ GeV the $v_2\{\mathrm{SP}\}$ is systematically larger than $v_2\{\mathrm{2PC}\}$.

To study the energy dependence the $v_n\,(p_{\mathrm{T}})$ values obtained with the EP method are compared with corresponding measurements in Pb+Pb collisions at $\sqrt{s_{\mathrm{NN}}} = 2.76$ TeV. The comparison shows that the p_{T} dependence of the v_n is consistent within statistic and systematic uncertainties between both, $\sqrt{s_{\mathrm{NN}}} = 2.76$ TeV and $\sqrt{s_{\mathrm{NN}}} = 5.02$ TeV.

Comparisons with the measurements in Xe+Xe collisions at $\sqrt{s_{\mathrm{NN}}} = 5.44$ TeV, presented for the SP method, show qualitative agreement between both collision systems implying that the flow is derived from the initial geometry of the created medium. However, the quantitative comparison shows that the Pb+Pb v_n is smaller than Xe+Xe v_n in the most central events, which is due to larger initial fluctuations in the smaller collision system. On the other hand, in mid-central and peripheral collisions the Pb+Pb v_n values are larger than those obtained in Xe+Xe collisions. This is expected as the viscous effects, which reduce the v_n values, could be larger for the lighter, Xe+Xe, collision system.

The $v_2(p_{\mathrm{T}})$ and $v_3(p_{\mathrm{T}})$ harmonics obtained with the SP method are compared to corresponding measurements published by the CMS experiment. The comparison is done for 0–5%, 10–20%, 30–40% and 50–60% centrality intervals and for pseudorapidity restricted to $|\eta| < 1$. The results from the two experiments agree well overall, though some differences up to 5% are observed. Such differences may result from slightly different analysis details e.g. the 2-subevent vs 3-subevent SP method definition or a different pseudorapidity gap between the calorimeter and the inner detector.

Moreover, the v_n results obtained with the SP method are compared to hydrodynamic predictions as well as to theoretical calculations of high-p_{T} v_n harmonics. For the hydrodynamic p_{T} region, $p_{\mathrm{T}} < 1$ GeV, the v_2, v_3 and v_4 harmonics obtained using 5.02 TeV Pb+Pb data are generally consistent with predictions in central and mid-central collisions. However, for higher p_{T}, yet still in the hydrodynamic domain, the measurements and predictions start to diverge and the discrepancies are observed to be 25–35% at $p_{\mathrm{T}} = 2$ GeV. For the high-p_{T} region, $p_{\mathrm{T}} > 5$ GeV, the v_2 and v_3 coefficients obtained with the SP method in 0–5% and 30–40% centrality intervals are compared with the CUJET3.0 and SHEE models. The former describes well the shape of the p_{T} dependence, however the v_n magnitudes significantly diverge from the measurements. The latter model is found to be quantitatively consistent with the data for the v_2 and v_3 measured in the analysis.

The work presented in the thesis provides precise measurements of the flow harmonics that can be used to constrain the theoretical modelling of the dense and hot medium created in heavy-ion collisions.

Appendix A

Event plane uniformity

The mean $Q_{n,x}$ and $Q_{n,y}$ of flow vector distributions as a function of $\Sigma E_{\mathrm{T}}^{\mathrm{FCal}}$ before and after applying re-centering Q_n-vector bias correction for $n = 2 - 7$ are shown in Figure A.1. The distributions are shown for both FCal sides: $\eta < 0$ and $\eta > 0$. Mean flow vectors are assumed to be centered at (0,0) in the whole detector, independently on collision centrality, which is achieved using uniformity procedure described in section 5.2.1.

Figure A.2 shows the elements of matrix defined in Eq. 5.15, the $\langle Q_{n,x}Q_{n,y}\rangle$, $\langle Q_{n,x}^2\rangle$ and $\langle Q_{n,y}^2\rangle$ distributions, as a function of $\Sigma E_{\mathrm{T}}^{FCal}$ for $n = 2 - 7$ and for both, N and P, sub-regions of the FCal. The Q_n-vector skewness correction, described in section 5.2.1, results in $\langle Q_{n,x}Q_{n,y}\rangle = 0$ and $\langle Q_{n,x}^2\rangle = \langle Q_{n,y}^2\rangle$.

Figure A.3 shows the Ψ_n angle distributions for n = 2–7 and for both, N and P, sub-regions of the FCal, before, after the re-centering Q_n-vector correction and after both the Q_n-vector corrections. The distributions, normalized to the number of events, are presented for central (0–10%), semi-central (30–40%) and peripheral (50–60%) collisions. Applying two-step Q_n-vector corrections results in fully uniform Ψ_n distributions throughout all centrality intervals for each n.

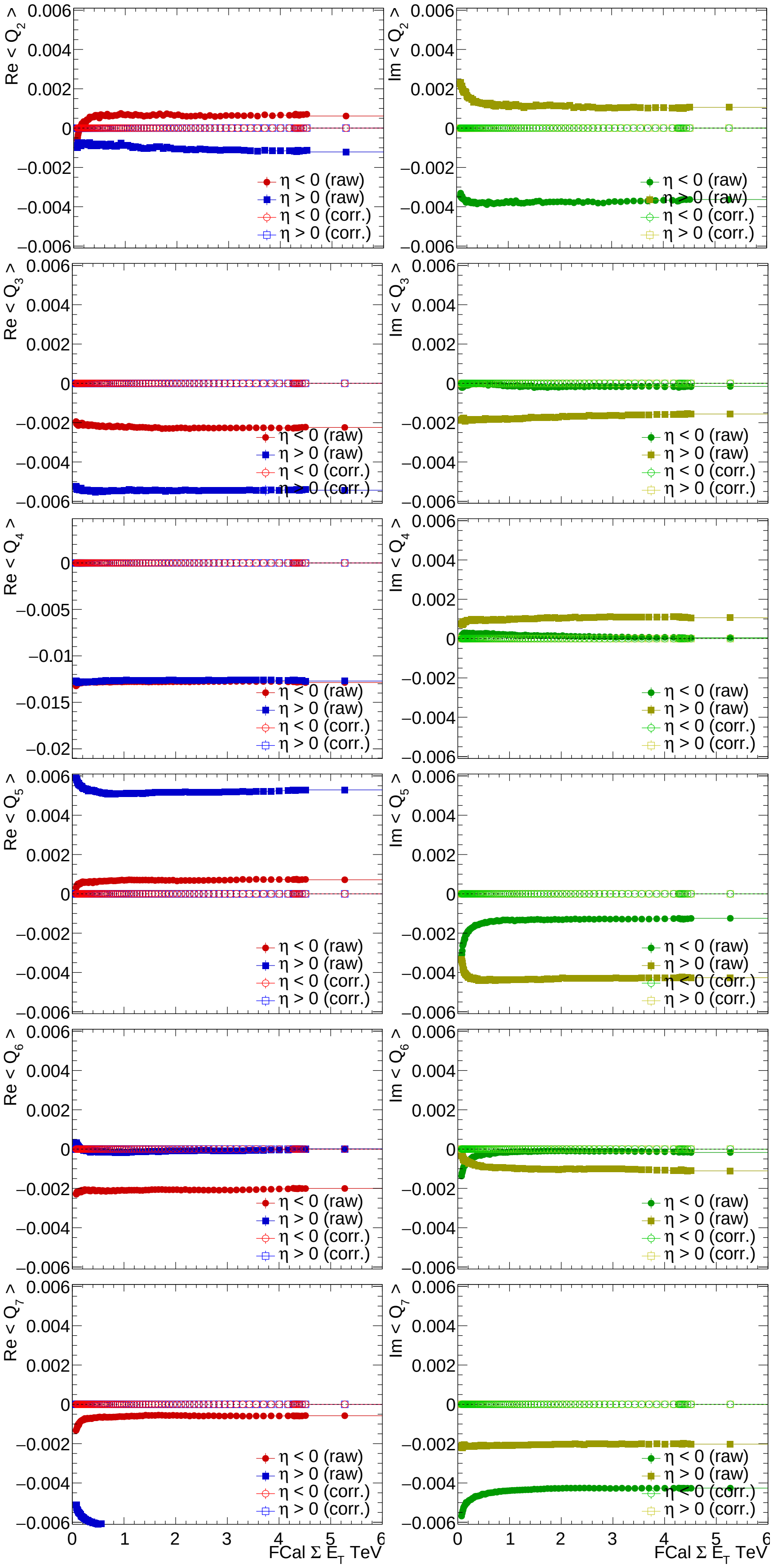

Figure A.1: Mean Q_n-vector constituents, i.e. the real part $Q_{n,x}$ (left panels), and the imaginary part $Q_{n,y}$ (right panels), as function of $\Sigma E_{\mathrm{T}}^{\mathrm{FCal}}$ before (solid points) and after Q_n-vector correction (open points) for $n = 2$–7. Each row corresponds to different harmonic order, top row is for $n = 2$.

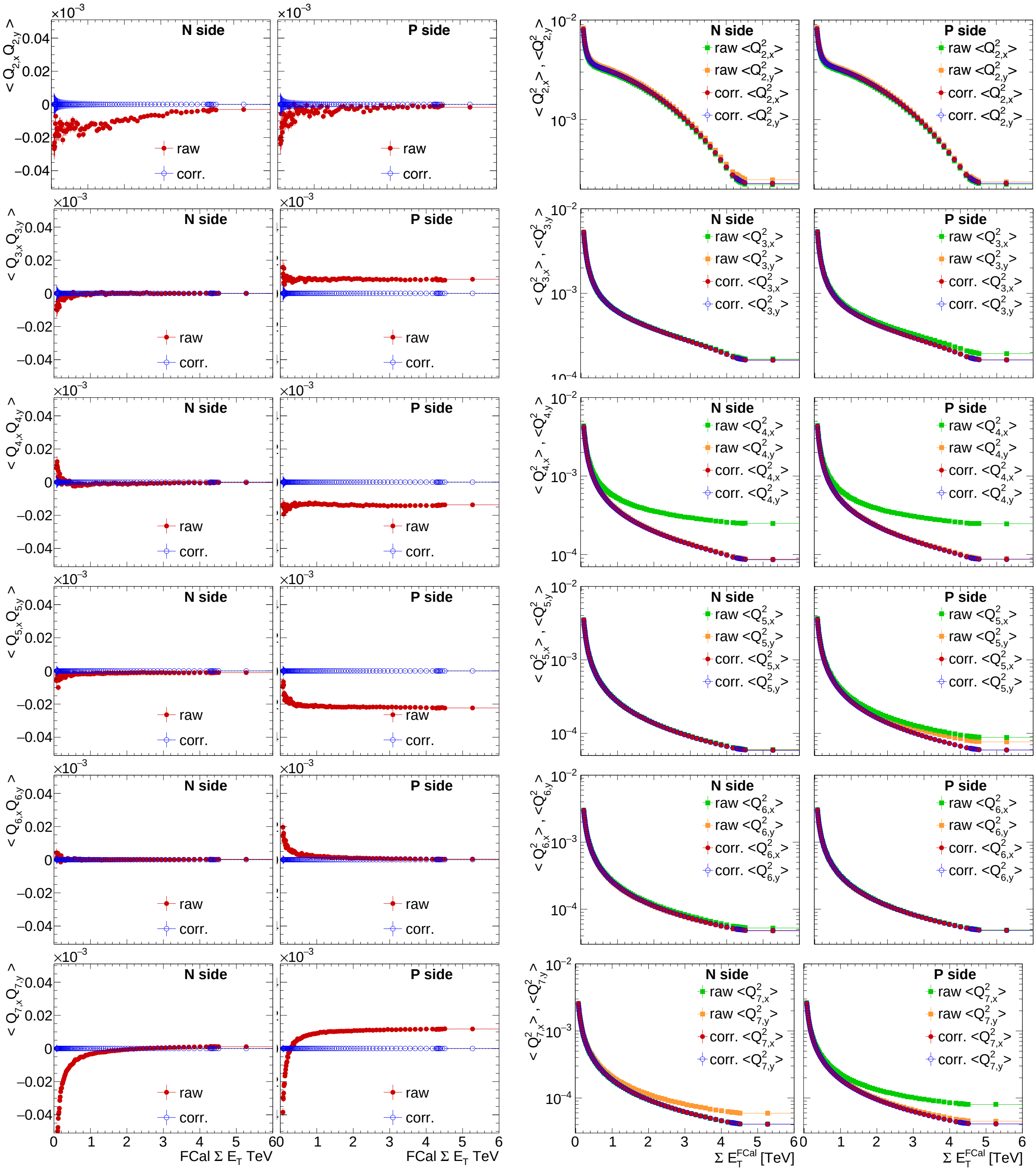

FIGURE A.2: Left and middle left column: $\langle Q_{n,x}Q_{n,y}\rangle$ as function of $\Sigma E_{\mathrm{T}}^{FCal}$ before and after Q_n-vector corrections for n = 2–7. Middle right and right column: $\langle Q^2_{n,x}\rangle$ and $\langle Q^2_{n,y}\rangle$ as function of $\Sigma E_{\mathrm{T}}^{FCal}$ before and after Q_n-vector corrections for n = 2–7. Each row corresponds to different harmonic order, top row is for n = 2.

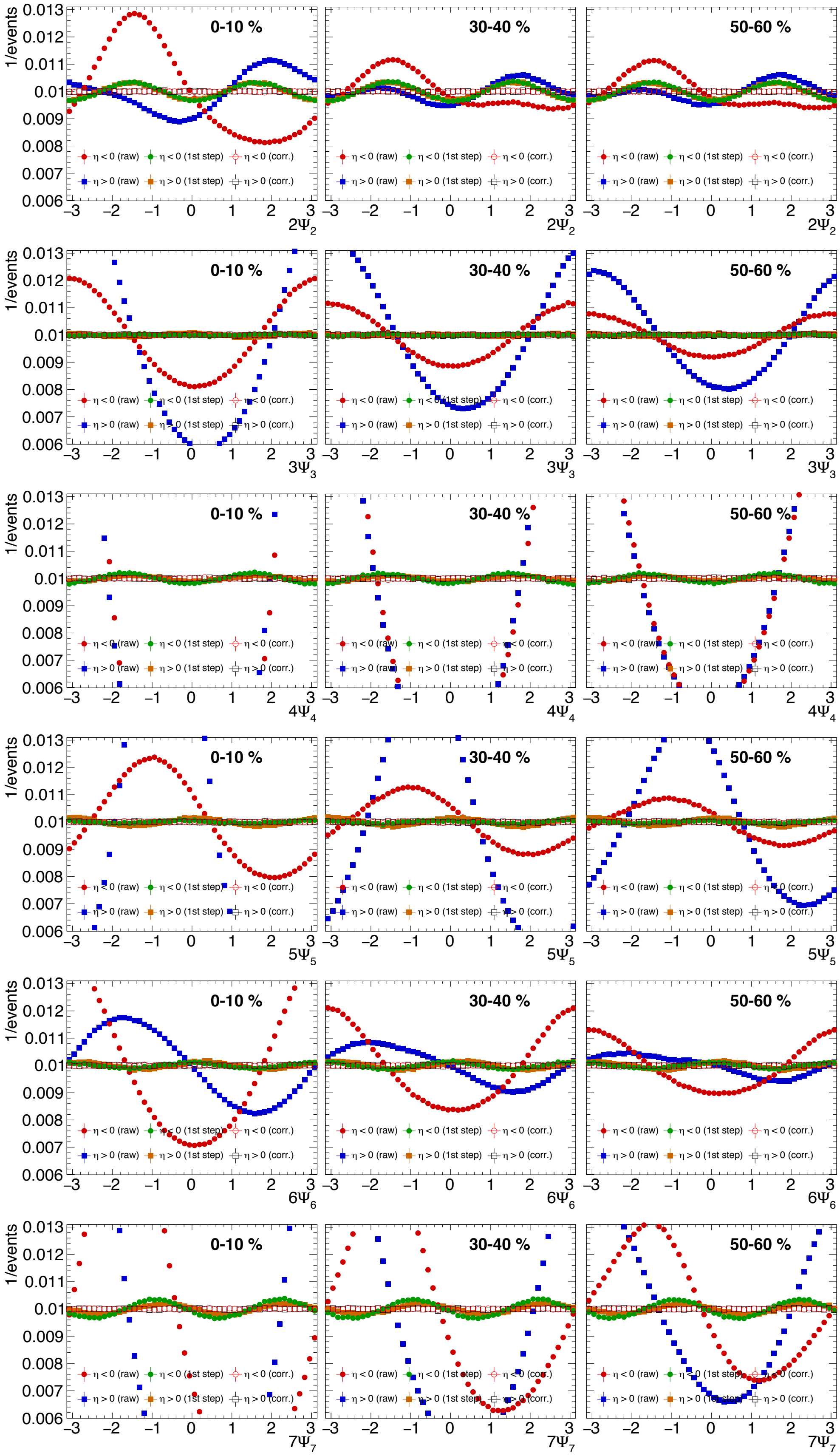

FIGURE A.3: The distributions of the event-plane angles Ψ_n for harmonics $n = 2$–7 before (row), after the re-centering Q_n-vector correction (1st step) and after both the Q_n-vector corrections (corr.). The event plane angle is measured in the FCal at negative and positive η for central (0–10%, left panels), mid-central (30–40%, middle panels) and peripheral (50–60%, right panels) events correspondingly. Each row indicates different harmonic, starting from $n = 2$ at the upper panels up to $n = 7$ at the lower panel. Distributions are normalized to the number of events.

Appendix B

Monte Carlo closure test

The MC closure test is done for $v_2 - v_6$ harmonics and for both, SP and EP methods. Figures B.1 to B.5 show the p_T dependence of the $\frac{v_n^{reco}}{v_n^{true}}$ up to 60 GeV for centrality intervals from the most central (0–5%) to the most peripheral (70–80%). The non-closure is observed for each v_n harmonic at low-p_T up to about 1 GeV for centralities of 0–40%. The non-closure is used to correct the $v_2 - v_5$ measurement based on experimental data, to provide more reliable results. The correction for v_6 is not established due to statistical fluctuations. The MC non-closure is also considered as one of the systematic uncertainty sources for v_2–v_5 harmonics.

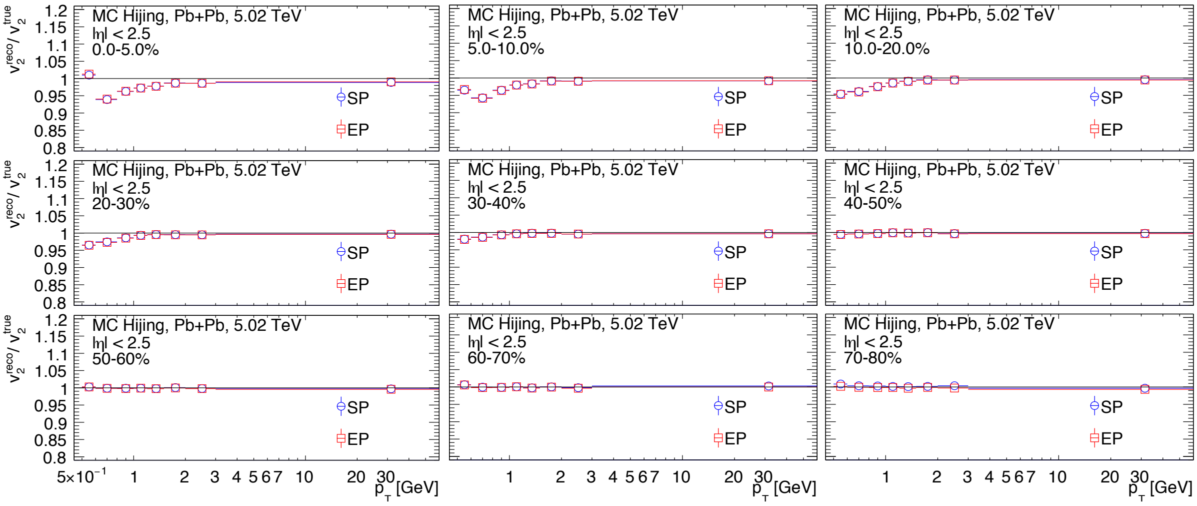

FIGURE B.1: The $v_2(p_T)$ closure test for SP (blue solid points) and EP (red open points) methods in 9 centrality bins. Error bars correspond to statistical uncertainties.

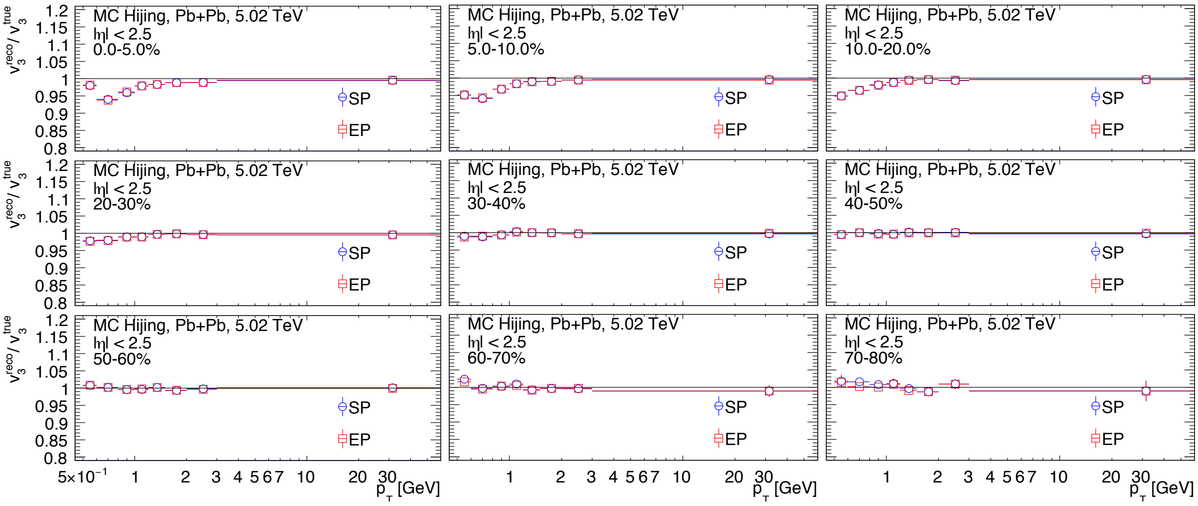

FIGURE B.2: The $v_3(p_T)$ closure test for SP (blue solid points) and EP (red open points) methods in 9 centrality bins. Error bars correspond to statistical uncertainties.

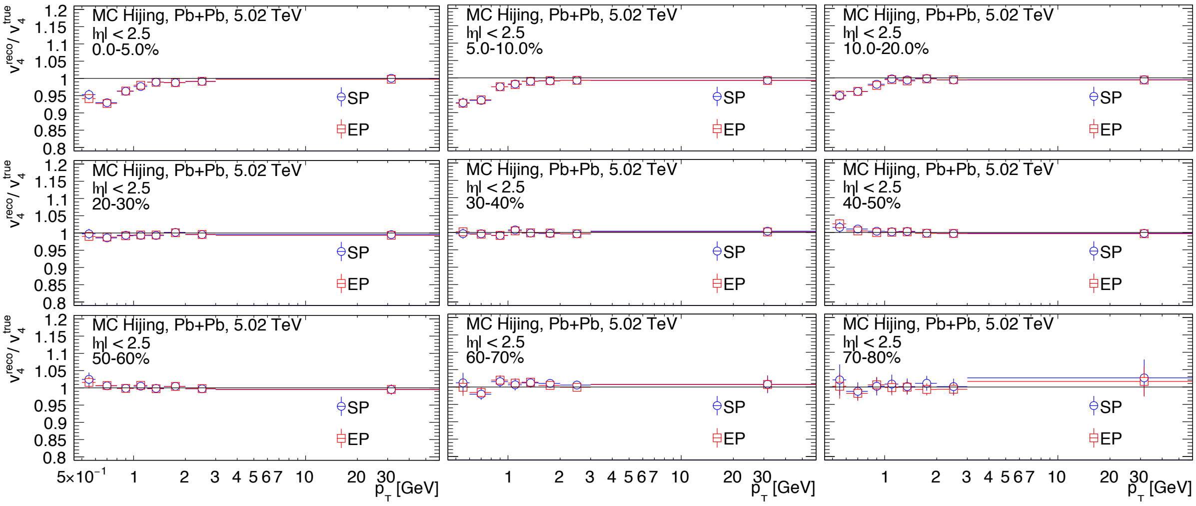

FIGURE B.3: The $v_4(p_T)$ closure test for SP (blue solid points) and EP (red open points) methods in 9 centrality bins. Error bars correspond to statistical uncertainties.

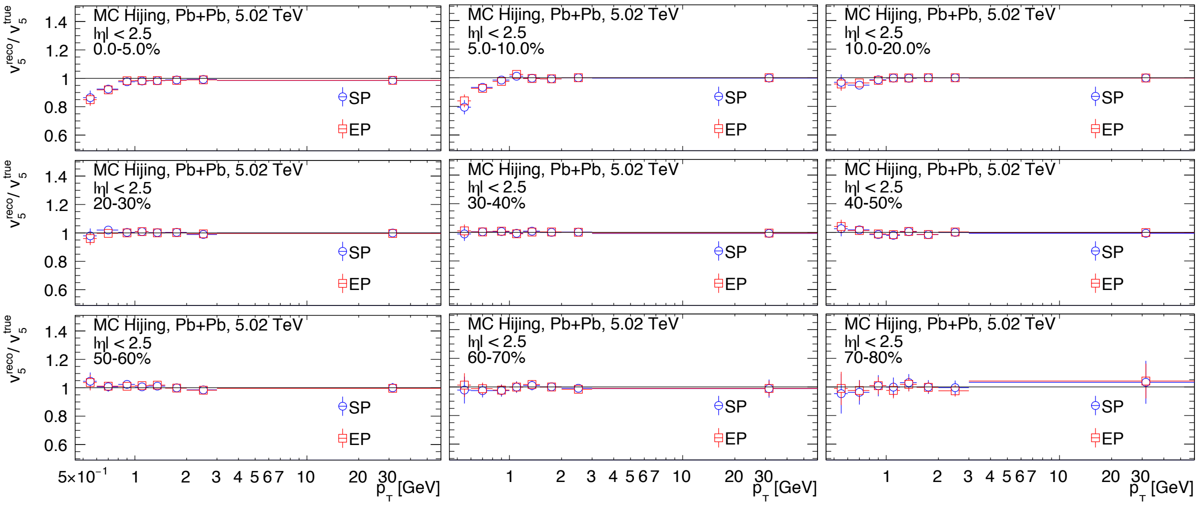

FIGURE B.4: The $v_5(p_T)$ closure test for SP (blue solid points) and EP (red open points) methods in 9 centrality bins. Error bars correspond to statistical uncertainties.

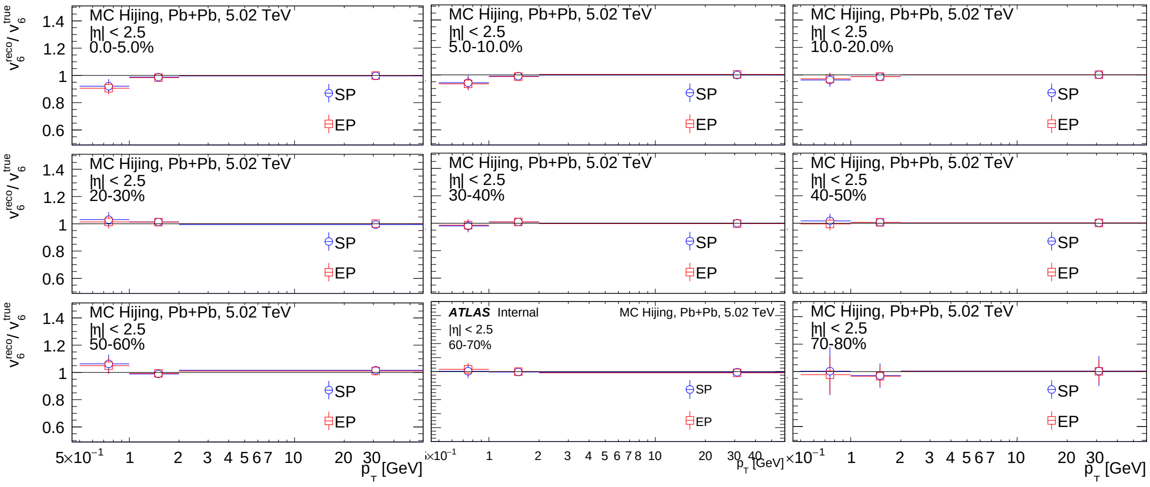

FIGURE B.5: The $v_6(p_T)$ closure test for SP (blue solid points) and EP (red open points) methods in 9 centrality bins. The v_6^{reco} is obtained using all reconstructed tracks. Error bars correspond to statistical uncertainties.

Appendix C

Event-plane results

The flow harmonics were also measured using the event-plane method. Figure C.1 shows the $v_n\{\mathrm{SP}\}$ (n = 2–7) measurements as a function of transverse momentum for several centrality bins. Figure C.2 shows v_n results as a function of pseudorapidity integrated over p_{T} = 0.8–1 GeV, p_{T} = 2–3 GeV and p_{T} = 7–60 GeV. Figure C.3 shows the N_{part} dependence of integrated v_n for several p_{T} slices. Conclusions are the same as for the SP measurement.

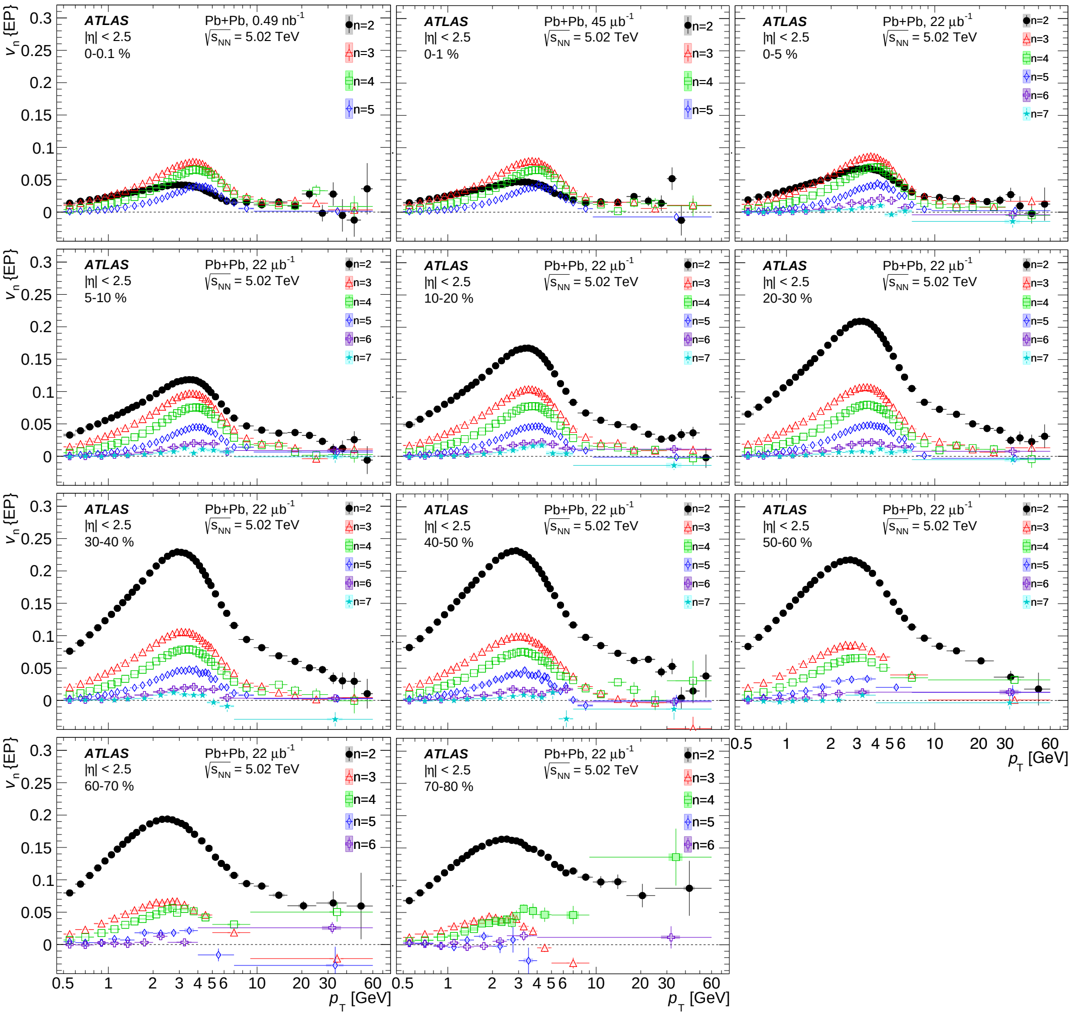

Figure C.1: The v_n obtained with the EP method as a function of the transverse momentum in 11 centrality intervals integrated over $|\eta| < 2.5$. The 0–0.01% and 0–1% panels show v_2–v_5 harmonics due to large statistical fluctuations for higher order harmincs. The v_7 harmonic is shown for centralities 0–60%. Error bars correspond to statistical uncertainties. The shaded boxes indicates systematic uncertainties.

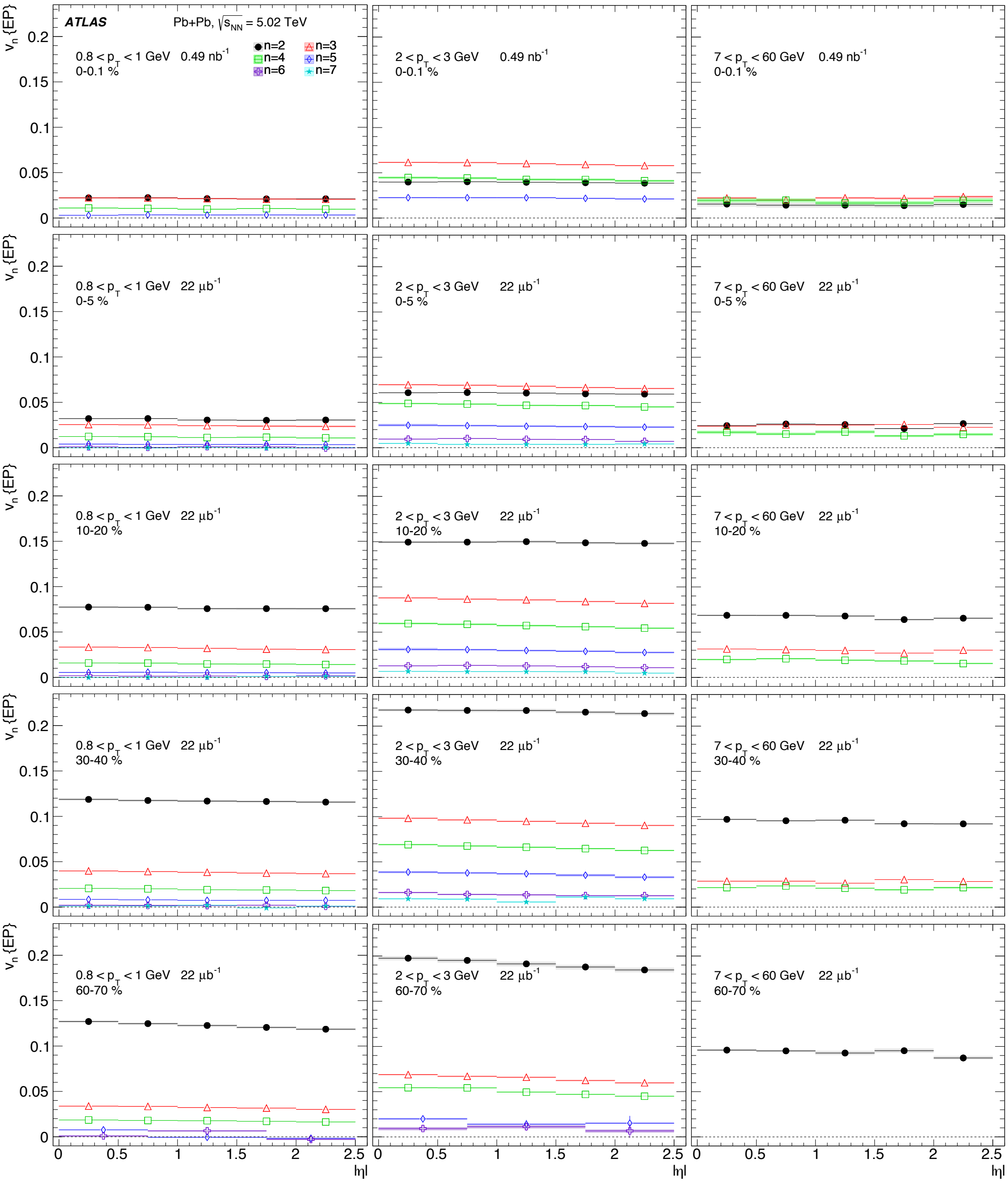

FIGURE C.2: The integrated v_n obtained with the EP method as a function of $|\eta|$ in 11 centrality intervals integrated over $0.8 < p_T < 1$ GeV, $2 < p_T < 3$ GeV and $7 < p_T < 60$ GeV. Error bars correspond to statistical uncertainties. The shaded rectangles indicates systematic uncertainties.

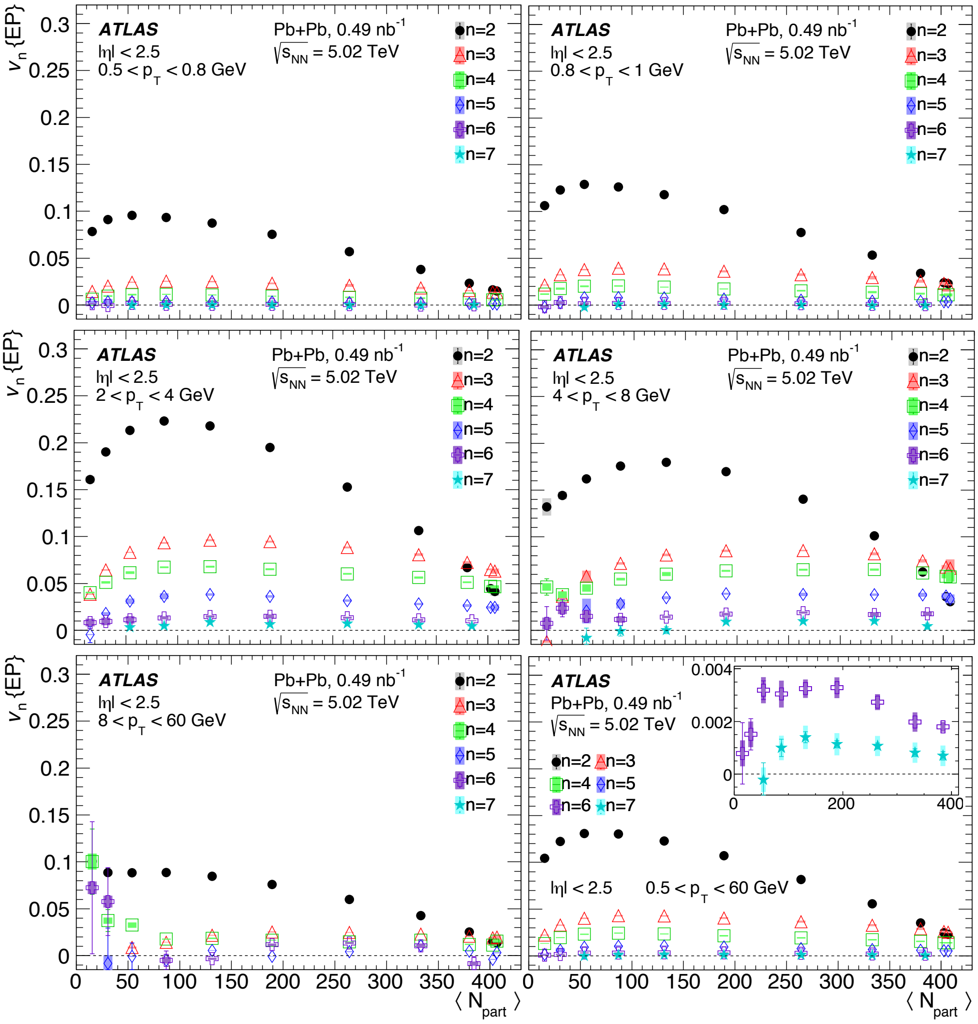

FIGURE C.3: Integrated v_n vs. N_{part} for six p_T ranges (0.5–60 GeV) extracted from the EP method. Error bars correspond to statistical uncertainties. The shaded rectangles indicates systematic uncertainties.

Bibliography

[1] L. R. Evans and P. Bryant, *LHC Machine*, JINST **3** (2008) S08001. 164 p, URL: `http://cds.cern.ch/record/1129806`.

[2] ATLAS and CMS Collaboration, *Combined Measurement of the Higgs Boson Mass in pp Collisions at* $\sqrt{s} = 7$ *and 8 TeV with the ATLAS and CMS Experiments*, Phys. Rev. Lett. **114** (2015) 191803, arXiv: `1503.07589 [hep-ex]`.

[3] ATLAS Collaboration, *The ATLAS Experiment at the CERN Large Hadron Collider*, JINST **3** (2008) S08003.

[4] CMS Collaboration, *The CMS Experiment at the CERN LHC*, JINST **3** (2008) S08004.

[5] ALICE Collaboration, *The ALICE experiment at the CERN LHC*, JINST **3** (2008) S08002.

[6] LHCb Collaboration, *The LHCb Detector at the LHC*, JINST **3** (2008) S08005.

[7] R. K. Ellis and W. J. Stirling, "QCD and collider physics", *The 1990 CERN School of Physics Mallorca, Spain, September 16-29, 1990*, URL: `http://lss.fnal.gov/cgi-bin/find_paper.pl?conf-90-164`.

[8] PHOBOS Collaboration, Back, B. B. et al. *The PHOBOS perspective on discoveries at RHIC*, Nucl. Phys. **A757** (2005) 28, arXiv: `nucl-ex/0410022 [nucl-ex]`.

[9] STAR Collaboration, Adams, J. et al. *Experimental and theoretical challenges in the search for the quark gluon plasma: The STAR Collaboration's critical assessment of the evidence from RHIC collisions*, Nucl. Phys. **A757** (2005) 102, arXiv: `nucl-ex/0501009 [nucl-ex]`.

[10] BRAHMS Collaboration, Arsene, I. et al. *Quark gluon plasma and color glass condensate at RHIC? The Perspective from the BRAHMS experiment*, Nucl. Phys. **A757** (2005) 1, arXiv: `nucl-ex/0410020 [nucl-ex]`.

[11] PHENIX Collaboration, Adcox, K. et al. *Formation of dense partonic matter in relativistic nucleus-nucleus collisions at RHIC: Experimental evaluation by the PHENIX collaboration*, Nucl. Phys. **A757** (2005) 184, arXiv: `nucl-ex/0410003 [nucl-ex]`.

[12] ATLAS Collaboration, *Measurement of the azimuthal anisotropy of charged particles produced in* $\sqrt{s_{\text{NN}}} = 5.02$ *TeV Pb+Pb collisions with the ATLAS detector*, (2018), arXiv: `1808.03951 [nucl-ex]`.

[13] ATLAS Collaboration, *Measurement of longitudinal flow decorrelations in Pb+Pb collisions at* $\sqrt{s_{NN}} = 2.76$ *and* 5.02 *TeV with the ATLAS detector*, Eur. Phys. J. **C78** (2018) 142, arXiv: `1709.02301 [nucl-ex]`.

[14] ATLAS Collaboration, *Measurement of four-particle azimuthal cumulants in Pb+Pb collisions at* $\sqrt{s_{NN}} = 5.02$ *TeV with the ATLAS detector*, tech. rep. ATLAS-CONF-2017-066, CERN, 2017, URL: `http://cds.cern.ch/record/2285570`.

[15] ATLAS Collaboration, *Measurement of* v_n *- mean* p_T *correlations in lead-lead collisions at* $\sqrt{s_{NN}} = 5.02$ *TeV with the ATLAS detector.*, tech. rep. ATLAS-CONF-2018-008, CERN, 2018, URL: `http://cds.cern.ch/record/2318589`.

[16] ATLAS Collaboration, *Measurement of the azimuthal anisotropy of charged particles produced in 5.02 TeV Pb+Pb collisions with the ATLAS detector*, tech. rep. ATLAS-CONF-2016-105, CERN, 2016, URL: `http://cds.cern.ch/record/2220372`.

[17] K. Burka, *Measurement of azimuthal flow of soft and high-* p_T *charged particles in 5.02 TeV Pb+Pb collisions with the ATLAS detector*, Nucl. Part. Phys. Proc. **289-290** (2017) 441.

[18] K. Burka, *The Flow Harmonics Measurement with the Event Plane and Multi-particle Cumulant Methods in Pb+Pb Collisions at 2.76 TeV in ATLAS*, Acta Phys. Polon. **B47** (2016) 1625.

[19] K. Burka, *Measurement of the ridge correlations in pp and pPb collisions with the ATLAS detector at the LHC*, PoS **DIS2016** (2016) 053.

[20] ATLAS Collaboration, *Measurement of the azimuthal anisotropy of charged particle production in Xe+Xe collisions at* $\sqrt{s_{\mathrm{NN}}}$*=5.44 TeV with the ATLAS detector*, tech. rep. ATLAS-CONF-2018-011, CERN, 2018, URL: `http://cds.cern.ch/record/2318870`.

[21] D. J. Griffiths, *Introduction to elementary particles; 2nd rev. version*, Physics textbook, Wiley, 2008, URL: `https://cds.cern.ch/record/111880`.

[22] K. G. Wilson, *Confinement of Quarks*, Phys. Rev. **D10** (1974) 2445, [,319(1974)].

[23] D. J. Gross and F. Wilczek, *Ultraviolet Behavior of Non-Abelian Gauge Theories*, Phys. Rev. Lett. **30** (26 1973) 1343, URL: `https://link.aps.org/doi/10.1103/PhysRevLett.30.1343`.

[24] D. J. Gross and F. Wilczek, *Asymptotically Free Gauge Theories - I*, Phys. Rev. **D8** (1973) 3633.

[25] H. D. Politzer, *Reliable Perturbative Results for Strong Interactions?*, Phys. Rev. Lett. **30** (1973) 1346, [,274(1973)].

[26] R. Brock et al., *Handbook of perturbative QCD: Version 1.0*, Rev. Mod. Phys. **67** (1995) 157.

[27] F. Karsch, *Properties of the Quark Gluon Plasma: A Lattice perspective*, Nucl. Phys. A783 **783** (2007) 13.

[28] *The Frontiers of Nuclear Science, A Long Range Plan*, (2008), arXiv: `0809.3137 [nucl-ex]`.

[29] J. I. Kapusta, *Quantum chromodynamics at high temperature*, Nuclear Physics B **148** (1979) 461, ISSN: 0550-3213, URL: `http://www.sciencedirect.com/science/article/pii/0550321379901469`.

[30] E. V. Shuryak, *Quark-Gluon Plasma and Hadronic Production of Leptons, Photons and Pions*, Phys. Lett. **78B** (1978) 150, [Yad. Fiz.28,796(1978)].

[31] Y. Aoki, G. Endrodi, Z. Fodor, S. D. Katz, and K. K. Szabo, *The Order of the quantum chromodynamics transition predicted by the standard model of particle physics*, Nature **443** (2006) 675, arXiv: `hep-lat/0611014 [hep-lat]`.

[32] A. Bazavov et al., *The chiral and deconfinement aspects of the QCD transition*, Phys. Rev. **D85** (2012) 054503, arXiv: `1111.1710 [hep-lat]`.

[33] A. Bazavov et al., *Equation of state in (2+1)-flavor QCD*, Phys. Rev. **D90** (2014) 094503, arXiv: `1407.6387 [hep-lat]`.

[34] A. Aduszkiewicz, *Recent results from NA61/SHINE*, Nucl. Phys. **A967** (2017) 35, arXiv: `1704.08071 [hep-ex]`.

[35] X. Luo and N. Xu, *Search for the QCD Critical Point with Fluctuations of Conserved Quantities in Relativistic Heavy-Ion Collisions at RHIC : An Overview*, Nucl. Sci. Tech. **28** (2017) 112, arXiv: `1701.02105 [nucl-ex]`.

[36] P. Senger, *The heavy-ion program of the future FAIR facility*, Journal of Physics: Conference Series **798** (2017) 012062, URL: `http://stacks.iop.org/1742-6596/798/i=1/a=012062`.

[37] B.Alver, M.Baker, C.Loizides, and P.Steinberg, *The PHOBOS Glauber Monte Carlo*, (), arXiv: `0805.4411v1`.

[38] M. L. Miller, K. Reygers, S. J. Sanders, and P. Steinberg, *Glauber modeling in high energy nuclear collisions*, Ann. Rev. Nucl. Part. Sci. **57** (2007) 205, arXiv: `nucl-ex/0701025 [nucl-ex]`.

[39] R. Snellings, *Collective Expansion at the LHC: selected ALICE anisotropic flow measurements*, J. Phys. **G41** (2014) 124007, arXiv: `1408.2532 [nucl-ex]`.

[40] M. Strickland, *Anisotropic Hydrodynamics: Three lectures*, Acta Phys. Polon. **B45** (2014) 2355, arXiv: `1410.5786 [nucl-th]`.

[41] J.-Y. Ollitrault, *Anisotropy as a signature of transverse collective flow*, Phys. Rev. D **46** (1 1992) 229, URL: `http://link.aps.org/doi/10.1103/PhysRevD.46.229`.

[42] S. Voloshin and Y. Zhang, *Flow study in relativistic nuclear collisions by Fourier expansion of Azimuthal particle distributions*, Z. Phys. **C70** (1996) 665, arXiv: `hep-ph/9407282 [hep-ph]`.

[43] ALICE Collaboration, *Elliptic flow of charged particles in Pb-Pb collisions at 2.76 TeV*, Phys. Rev. Lett. **105** (2010) 252302, arXiv: `1011.3914 [nucl-ex]`.

[44] ATLAS Collaboration, *Measurement of the pseudorapidity and transverse momentum dependence of the elliptic flow of charged particles in lead-lead collisions at* $\sqrt{s_{NN}} = 2.76$ *TeV with the ATLAS detector*, Phys. Lett. **B707** (2012) 330, arXiv: `1108.6018 [hep-ex]`.

[45] CMS Collaboration, *Measurement of the elliptic anisotropy of charged particles produced in PbPb collisions at* $\sqrt{s_{NN}} = 2.76$ *TeV*, Phys. Rev. C **87** (1 2013) 014902, URL: `http://link.aps.org/doi/10.1103/PhysRevC.87.014902`.

[46] D. Teaney, *The Effects of viscosity on spectra, elliptic flow, and HBT radii*, Phys. Rev. **C68** (2003) 034913, arXiv: `nucl-th/0301099 [nucl-th]`.

[47] S. Ryu et al., *Importance of the Bulk Viscosity of QCD in Ultrarelativistic Heavy-Ion Collisions*, Phys. Rev. Lett. **115** (2015) 132301, arXiv: `1502.01675 [nucl-th]`.

[48] A. M. Poskanzer and S. Voloshin, *Methods for analyzing anisotropic flow in relativistic nuclear collisions*, Phys.Rev. **C58** (1998) 1671, arXiv: `nucl-ex/9805001 [nucl-ex]`.

[49] S. A. Voloshin, A. M. Poskanzer, and R. Snellings, *Collective phenomena in non-central nuclear collisions*, Landolt-Bornstein **23** (2010) 293, arXiv: `0809.2949 [nucl-ex]`.

[50] E. Iancu, “QCD in heavy ion collisions”, *Proceedings, 2011 European School of High-Energy Physics (ESHEP 2011): Cheile Gradistei, Romania, September 7-20, 2011*, 2014 197, arXiv: `1205.0579 [hep-ph]`, URL: `https://inspirehep.net/record/1113441/files/arXiv:1205.0579.pdf`.

[51] ATLAS Collaboration, *Measurement of the azimuthal anisotropy for charged particle production in* $\sqrt{s_{NN}} = 2.76$ *TeV lead-lead collisions with the ATLAS detector*, Phys. Rev. **C86** (2012) 014907, arXiv: `1203.3087 [hep-ex]`.

[52] P. Kovtun, D. T. Son, and A. O. Starinets, *Viscosity in strongly interacting quantum field theories from black hole physics*, Phys. Rev. Lett. **94** (2005) 111601, arXiv: `hep-th/0405231 [hep-th]`.

[53] P. Romatschke and U. Romatschke, *Viscosity Information from Relativistic Nuclear Collisions: How Perfect is the Fluid Observed at RHIC?*, Phys. Rev. Lett. **99** (2007) 172301, arXiv: `0706.1522 [nucl-th]`.

[54] STAR Collaboration, Adams, J. et al. *Azimuthal anisotropy in Au+Au collisions at s(NN)**(1/2) = 200-GeV*, Phys. Rev. **C72** (2005) 014904, arXiv: `nucl-ex/0409033 [nucl-ex]`.

[55] PHENIX Collaboration, Adare, A. et al. *Azimuthal anisotropy of neutral pion production in Au+Au collisions at* $\sqrt(s_N N)$ *= 200 GeV: Path-length dependence of jet quenching and the role of initial geometry*, Phys. Rev. Lett. **105** (2010) 142301, arXiv: `1006.3740 [nucl-ex]`.

[56] ATLAS Collaboration, *Measurement of flow harmonics with multi-particle cumulants in Pb+Pb collisions at* $\sqrt{s_{\mathrm{NN}}} = 2.76$ *TeV with the ATLAS detector*, Eur. Phys. J. **C74** (2014) 3157, arXiv: `1408.4342 [hep-ex]`.

[57] ALICE Collaboration, *Anisotropic flow of charged particles in Pb-Pb collisions at* $\sqrt{s_{\mathrm{NN}}} = 5.02$ *TeV*, Phys. Rev. Lett. **116** (2016) 132302, arXiv: `1602.01119 [nucl-ex]`.

[58] CMS Collaboration, *Azimuthal anisotropy of charged particles with transverse momentum up to 100 GeV/ c in PbPb collisions at* $\sqrt{s}_{NN}$*=5.02 TeV*, Phys. Lett. **B776** (2018) 195, arXiv: `1702.00630 [hep-ex]`.

[59] ATLAS Collaboration, *Observation of Long-Range Elliptic Azimuthal Anisotropies in* $\sqrt{s}$ *=13 and 2.76 TeV pp Collisions with the ATLAS Detector*, Phys. Rev. Lett. **116** (2016) 172301, arXiv: `1509.04776 [hep-ex]`.

[60] ATLAS Collaboration, *Measurement with the ATLAS detector of multi-particle azimuthal correlations in p+Pb collisions at* $\sqrt{s_{NN}}$ *=5.02 TeV*, Phys. Lett. **B725** (2013) 60, arXiv: `1303.2084 [hep-ex]`.

[61] CMS Collaboration, *Evidence for collectivity in pp collisions at the LHC*, Phys. Lett. **B765** (2017) 193, arXiv: `1606.06198 [nucl-ex]`.

[62] ATLAS Collaboration, *Measurement of long-range pseudorapidity correlations and azimuthal harmonics in* $\sqrt{s_{NN}} = 5.02$ *TeV proton-lead collisions with the ATLAS detector*, Phys. Rev. **C90** (2014) 044906, arXiv: `1409.1792 [hep-ex]`.

[63] CMS Collaboration, *Evidence for Collective Multiparticle Correlations in p-Pb Collisions*, Phys. Rev. Lett. **115** (2015) 012301, arXiv: `1502.05382 [nucl-ex]`.

[64] CMS Collaboration, *Charged particle angular correlations in XeXe collision at* $\sqrt{s_{NN}} = 5.44$ *TeV*, tech. rep. CMS-PAS-HIN-18-001, CERN, 2018, URL: `https://cds.cern.ch/record/2318319`.

[65] P. Bożek, *Observation of the collective flow in proton-proton collisions*, Acta Phys. Polon. **B41** (2010) 837, arXiv: `0911.2392 [nucl-th]`.

[66] P. Bożek, *Elliptic flow in proton-proton collisions at* $sqrt(S) = 7$ *TeV*, Eur. Phys. J. **C71** (2011) 1530, arXiv: `1010.0405 [hep-ph]`.

[67] P. Bożek, *Collective flow in p-Pb and d-Pd collisions at TeV energies*, Phys. Rev. **C85** (2012) 014911, arXiv: `1112.0915 [hep-ph]`.

[68] T. Sjostrand, S. Mrenna, and P. Z. Skands, *A Brief Introduction to PYTHIA 8.1*, Comput. Phys. Commun. **178** (2008) 852, arXiv: `0710.3820 [hep-ph]`.

[69] PHENIX Collaboration, Adare, A. et al. *Scaling properties of azimuthal anisotropy in Au+Au and Cu+Cu collisions at s(NN) = 200-GeV*, Phys. Rev. Lett. **98** (2007) 162301, arXiv: `nucl-ex/0608033 [nucl-ex]`.

[70] STAR Collaboration, Abelev, B. I. et al. *Charged and strange hadron elliptic flow in Cu+Cu collisions at* $\sqrt{s_{NN}}$ *= 62.4 and 200 GeV*, Phys. Rev. **C81** (2010) 044902, arXiv: `1001.5052 [nucl-ex]`.

[71] C. De Melis, *The CERN accelerator complex.*, (2016), General Photo, URL: `https://cds.cern.ch/record/2119882`.

[72] W. Herr and B. Muratori, *Concept of luminosity*, (2006), URL: `https://cds.cern.ch/record/941318`.

[73] ATLAS Collaboration, *Study of the material of the ATLAS inner detector for Run 2 of the LHC*, JINST **12** (2017) P12009, arXiv: `1707.02826 [hep-ex]`.

[74] M. Capeans et al., *ATLAS Insertable B-Layer Technical Design Report*, tech. rep. CERN-LHCC-2010-013. ATLAS-TDR-19, 2010, URL: `https://cds.cern.ch/record/1291633`.

[75] ALICE Collaboration, *Centrality determination of Pb-Pb collisions at* $\sqrt{s_{NN}}$ *= 2.76 TeV with ALICE*, Phys. Rev. **C88** (2013) 044909, arXiv: `1301.4361 [nucl-ex]`.

[76] ALICE Collaboration, *Charged-particle multiplicity density at mid-rapidity in central Pb-Pb collisions at* $\sqrt{s_{NN}} = 2.76$ *TeV*, Phys. Rev. Lett. **105** (2010) 252301, arXiv: `1011.3916 [nucl-ex]`.

[77] S. S. Adler et al., *Identified charged particle spectra and yields in Au + Au collisions at* $\sqrt{s_{\mathrm{NN}}} = 200$ *GeV*, Phys. Rev. C **69** (3 2004) 034909, URL: `https://link.aps.org/doi/10.1103/PhysRevC.69.034909`.

[78] C. Loizides, J. Nagle, and P. Steinberg, *Improved version of the PHOBOS Glauber Monte Carlo*, SoftwareX **1-2** (2015) 13, arXiv: `1408.2549 [nucl-ex]`.

[79] X.-N. Wang and M. Gyulassy, *HIJING: A Monte Carlo model for multiple jet production in p p, p A and A A collisions*, Phys. Rev. **D44** (1991) 3501.

[80] S. Agostinelli et al., *GEANT4: A Simulation toolkit*, Nucl. Instrum. Meth. **A506** (2003) 250.

[81] W. Lukas, *Fast Simulation for ATLAS: Atlfast-II and ISF*, tech. rep. ATL-SOFT-PROC-2012-065, CERN, 2012, URL: `https://cds.cern.ch/record/1458503`.

[82] T. Yamanaka, *The ATLAS calorimeter simulation FastCaloSim*, J. Phys. Conf. Ser. **331** (2011) 032053.

[83] ATLAS Collaboration, *Measurement of charged-particle spectra in Pb+Pb collisions at* $\sqrt{s_{\mathrm{NN}}} = 2.76$ *TeV with the ATLAS detector at the LHC*, JHEP **09** (2015) 050, arXiv: `1504.04337 [hep-ex]`.

[84] S. Collaboration, Adler, C. et al. *Elliptic flow from two and four particle correlations in Au+Au collisions at s(NN)**(1/2) = 130-GeV*, Phys.Rev. **C66** (2002) 034904, arXiv: `nucl-ex/0206001 [nucl-ex]`.

[85] N. Borghini, P. M. Dinh, and J.-Y. Ollitrault, *A New method for measuring azimuthal distributions in nucleus-nucleus collisions*, Phys. Rev. **C63** (2001) 054906, arXiv: `nucl-th/0007063 [nucl-th]`.

[86] N. Borghini, R. S. Bhalerao, and J. Y. Ollitrault, *Anisotropic flow from Lee-Yang zeroes: A Practical guide*, J. Phys. **G30** (2004) S1213, arXiv: `nucl-th/0402053 [nucl-th]`.

[87] M. Luzum and J.-Y. Ollitrault, *Eliminating experimental bias in anisotropic-flow measurements of high-energy nuclear collisions*, Phys.Rev. **C87** (2013) 044907, arXiv: `1209.2323 [nucl-ex]`.

[88] ATLAS Collaboration, *Azimuthal femtoscopy in central p+Pb collisions at* $\sqrt{s_{\mathrm{NN}}} = 5.02$ *TeV with ATLAS*, tech. rep. ATLAS-CONF-2017-008, CERN, 2017, URL: `https://cds.cern.ch/record/2244818`.

[89] J. Jia and S. Mohapatra, *Disentangling flow and nonflow correlations via Bayesian unfolding of the event-by-event distributions of harmonic coefficients in ultrarelativistic heavy-ion collisions*, Phys. Rev. **C88** (2013) 014907, arXiv: `1304.1471 [nucl-ex]`.

[90] ATLAS Collaboration, *Charged-particle multiplicities in pp interactions at* $\sqrt{s} = 900$ *GeV measured with the ATLAS detector at the LHC*, Phys. Lett. **B688** (2010) 21, arXiv: `1003.3124 [hep-ex]`.

[91] B. Schenke, S. Jeon, and C. Gale, *Anisotropic flow in* $\sqrt{s} = 2.76$ *TeV Pb+Pb collisions at the LHC*, Phys. Lett. **B702** (2011) 59, arXiv: `1102.0575 [hep-ph]`.

[92] S. McDonald, C. Shen, F. Fillion-Gourdeau, S. Jeon, and C. Gale, *Hydrodynamic predictions for Pb+Pb collisions at 5.02 TeV*, Phys. Rev. **C95** (2017) 064913, arXiv: `1609.02958 [hep-ph]`.

[93] B. Betz, M. Gyulassy, and G. Torrieri, *Fourier Harmonics of High-pT Particles Probing the Fluctuating Intitial Condition Geometries in Heavy-Ion Collisions*, Phys. Rev. **C84** (2011) 024913, arXiv: `1102.5416 [nucl-th]`.

[94] B. Betz et al., *Cumulants and nonlinear response of high* p_T *harmonic flow at* $\sqrt{s_{NN}} = 5.02$ *TeV*, Phys. Rev. **C95** (2017) 044901, arXiv: `1609.05171 [nucl-th]`.

[95] CMS Collaboration, *Studies of azimuthal dihadron correlations in ultra-central PbPb collisions at* $\sqrt{s_{NN}} = 2.76$ *TeV*, JHEP **02** (2014) 088, arXiv: `1312.1845 [nucl-ex]`.

[96] G. Giacalone, J. Noronha-Hostler, M. Luzum, and J.-Y. Ollitrault, *Hydrodynamic predictions for 5.44 TeV Xe+Xe collisions*, Phys. Rev. **C97** (2018) 034904, arXiv: `1711.08499 [nucl-th]`.

[97] J. Xu, J. Liao, and M. Gyulassy, *Bridging Soft-Hard Transport Properties of Quark-Gluon Plasmas with CUJET3.0*, JHEP **02** (2016) 169, arXiv: `1508.00552 [hep-ph]`.

[98] J. Noronha-Hostler, B. Betz, J. Noronha, and M. Gyulassy, *Event-by-event hydrodynamics + jet energy loss: A solution to the* $R_{AA} \otimes v_2$ *puzzle*, Phys. Rev. Lett. **116** (2016) 252301, arXiv: `1602.03788 [nucl-th]`.

[99] J. Noronha-Hostler, J. Noronha, and F. Grassi, *Bulk viscosity-driven suppression of shear viscosity effects on the flow harmonics at energies available at the BNL Relativistic Heavy Ion Collider*, Phys. Rev. **C90** (2014) 034907, arXiv: `1406.3333 [nucl-th]`.

[100] B. Betz and M. Gyulassy, *Examining a reduced jet-medium coupling in Pb+Pb collisions at the Large Hadron Collider*, Phys. Rev. **C86** (2012) 024903, arXiv: `1201.0281 [nucl-th]`.

List of Figures

2.1 The phase diagram of QCD matter. 6
2.2 Simplified sketch of a heavy-ion collision. 7
2.3 Diagram of the space-time evolution of a heavy-ion collision. 8
2.4 Sketch of the non-central heavy-ion collision. 10
2.5 Schematic distribution of nucleons in the initial geometry of a collision. 11
2.6 Integrated elliptic flow, v_2, as a function of the collision $\sqrt{s_{\mathrm{NN}}}$ energy. 12
2.7 Elliptic flow, v_2, as a function of the transverse momentum for different experiments. 12
2.8 The v_n vs. centrality for p_{T} = 1–2 GeV measured by ATLAS at $\sqrt{s_{\mathrm{NN}}}$ = 2.76 TeV. 13
2.9 Anisotropic flow v_n harmonics measured by ALICE in Pb+Pb collisions at $\sqrt{s_{\mathrm{NN}}}$ = 5.02 TeV. 14
2.10 The v_n vs. p_{T} measured by ATLAS at $\sqrt{s_{\mathrm{NN}}}$ = 2.76 TeV. 14
2.11 The $v_n(\eta)$ measured by ATLAS at $\sqrt{s_{\mathrm{NN}}}$ = 2.76 TeV. 15
2.12 The v_2 (p_{T}) and v_3 (p_{T}) obtained by CMS at $\sqrt{s_{\mathrm{NN}}}$ = 5.02 TeV. 15
2.13 Left: The v_2 (p_{T}) measured in 13 TeV pp collisions for three ${N_{\mathrm{ch}}}^{\mathrm{rec}}$ intervals; Right: The v_2 (p_{T}) measured in 5.02 TeV p+Pb collisions with 2PC and 4-particle cumulant. 15
2.14 The v_2 (pT) measured by CMS in Xe+Xe collisions at $\sqrt{s_{\mathrm{NN}}}$ = 5.44 TeV. 16

3.1 The CERN's Accelerator complex. 17
3.2 The schematic view of the ATLAS detector. 19
3.3 Cutaway view of the ATLAS ID. 20
3.4 A quater-section view of the ATLAS ID. 21
3.5 Profile of the ATLAS calorimeter system. 22
3.6 Segmentation of EM barrel layers. 23
3.7 The FCal structure. 23

4.1 The distribution of the z coordinate of the primary vertex for Pb+Pb collisions at $\sqrt{s_{\mathrm{NN}}}$ = 5.02 TeV. 28
4.2 Spectator energy deposited in the ZDC calorimeters. 29
4.3 Correlation between the number of reconstructed charged particles and the $\Sigma E_{\mathrm{T}}^{\mathrm{FCal}}$. 30
4.4 The distribution of N_{ch} vs. N_{part} and b. 30

4.5 The FCal $\sum E_{\mathrm{T}}$ distribution from Pb+Pb data at $\sqrt{s_{NN}}$ = 5.02 TeV. 32
4.6 Comparison of selected track quantities in Pb+Pb collisions at $\sqrt{s_{\mathrm{NN}}}$ = 5.02 TeV and MC simulations. 34
4.7 Tracking efficiency as a functions of p_{T}, $\Sigma E_{\mathrm{T}}^{FCal}$ and η. 35
4.8 Fake rates as a function of p_{T} and η. 36

5.1 Illustration of the flow vectors used in the EP method. 39
5.2 Mean Q_2-vector constituents as function of ΣE_{T}^{FCal} before and after correction for the harmonic $n = 2$. 41
5.3 $\langle Q_{2,x} Q_{2,y} \rangle$ as function of $\Sigma E_{\mathrm{T}}^{FCal}$; $\langle Q_{n,x}^2 \rangle$ and $\langle Q_{n,y}^2 \rangle$ as function of $\Sigma E_{\mathrm{T}}^{FCal}$ 42
5.4 The distributions of the event-plane angles Ψ_2 43
5.5 Event plane angle correlations at negative N and positive P side of FCal for the harmonic order n = 2–7. 44
5.6 The resolution correction factors $R_n\{\mathrm{SP}\}$ (left) and $R_n\{\mathrm{EP}\}$ (right), dependence on $\Sigma E_{\mathrm{T}}^{\mathrm{FCal}}$. 45
5.7 The $\eta - \phi$ maps before and after applying track weighting. 45

6.1 The v_2 (p_{T}) closure test for SP and EP in 9 centrality bins. 50
6.2 The $\phi - \Psi_2$ distribution for true and reconstructed tracks in centrality bin 5−10%. The track reconstruction efficiency as a function of $\phi - \Psi_2$. 51
6.3 The v_2 closure without any correction compared to v_2 closure obtained with $\Delta\phi$-dependent efficiency correction 51
6.4 The v_2 closure test comparison between v_2^{reco} extracted from selected reconstructed tracks and v_2^{reco} extracted from tracks matched to generated primary particles. 52
6.5 The d_0 distributions obtained using data and MC before and afetr applying fake scaling correction. 53

7.1 Tracking efficiencies of the nominal selection and two systematic variations. 56
7.2 Fake track rate of the nominal selection and two systematic variations. 57
7.3 The relative difference $\Delta_{trkloose}$ and $\Delta_{trktight}$ for v_2 as a function of p_{T} obtained with the SP method. 57
7.4 Summary of systematic uncertainties in 5–10% centrality interval as a function of p_{T}. 61
7.5 Summary of systematic uncertainties in 40–50% centrality interval as a function of p_{T}. 61

8.1 The v_n obtained with the SP method as a function of the transverse momentum in 11 centrality intervals integrated over $|\eta| < 2.5$. 64
8.2 The v_n obtained with the SP method as a function of $|\eta|$ for three p_{T} slices: 0.8–1 GeV, 2–3 GeVand 7–60 GeV in five centrality bins: 0–0.1%, 0–5%, 10–20%, 30–40% and 60–70%. 65
8.3 Integrated v_n vs. N_{part} for six p_{T} ranges as indicated in the legend extracted from the SP method. 66
8.4 Comparison of the v_n obtained with the EP and SP methods as a function of p_{T} in three centrality bins: 0–5%, 20–30% and 40–50%. The v_n as a function of N_{part}, integrated over $0.5 < p_{\mathrm{T}} < 60$ GeV. 68

8.5 Comparison of the v_n obtained with the 2PC and SP methods as a function of p_{T}. 69
8.6 Comparison of the v_n obtained with the EP method in Pb+Pb collisions at the energy $\sqrt{s_{\mathrm{NN}}}$ = 2.76 TeV and $\sqrt{s_{\mathrm{NN}}}$ = 5.02 TeV as a function of p_{T}. 71
8.7 The v_n (p_{T}) for n = 2–5 measured with SP method at $\sqrt{s_{\mathrm{NN}}}$ = 5.44 TeV collisions in three centrality intervals: 0–5%, 20–30% and 50–60%. 72
8.8 The v_2–v_5 harmonics measured with the SP method in Pb+Pb and Xe+Xe collisions. 73
8.9 The v_2 and v_3 results compared with the CMS measurement obtained with the SP method as a function of p_{T}. 74
8.10 The differential $v_n(p_{\mathrm{T}})$ compared with the theoretical calculations at low-p_{T}. 75
8.11 The differential v_n (p_{T}) compared with the theoretical calculations at high-p_{T}. 76

A.1 Mean Q_n-vector constituents as function of $\Sigma E_{\mathrm{T}}^{\mathrm{FCal}}$. 82
A.2 The $\langle Q_{n,x}Q_{n,y}\rangle$, $\langle Q_{n,x}^2\rangle$ and $\langle Q_{n,y}^2\rangle$ as function of $\Sigma E_{\mathrm{T}}^{FCal}$ for n=2–7. 83
A.3 The distributions of the event-plane angles Ψ_n for harmonics n = 2–7 before and after the Q_n-vector corrections. 84

B.1 The $v_2(p_{\mathrm{T}})$ closure test for the SP and EP methods in 9 centrality bins. 85
B.2 The $v_3(p_{\mathrm{T}})$ closure test for the SP and EP methods in 9 centrality bins. 86
B.3 The $v_4(p_{\mathrm{T}})$ closure test for the SP and EP methods in 9 centrality bins. 86
B.4 The $v_5(p_{\mathrm{T}})$ closure test for the SP and EP methods in 9 centrality bins. 87
B.5 The $v_6(p_{\mathrm{T}})$ closure test for the SP and EP methods in 9 centrality bins. 87

C.1 The v_n obtained with the EP method as a function of the transverse momentum in 11 centrality intervals integrated over $|\eta| < 2.5$. 89
C.2 The integrated v_n obtained with the EP method as a function of $|\eta|$ in 11 centrality intervals integrated over $0.8 < p_{\mathrm{T}} < 1$ GeV, $2 < p_{\mathrm{T}} < 3$ GeV and $7 < p_{\mathrm{T}} < 60$ GeV. 90
C.3 Integrated v_n vs. N_{part} for six p_{T} ranges extracted from the EP method. 91

List of Tables

4.1 The luminosities and number of events sampled by the triggers used in the analysis. 27
4.2 Number of events surviving successive selection requirements. 28
4.3 Centrality classes definition. 31
4.4 Differences between track quality selection. 33

5.1 Summary of the phase space binning used in the analysis. 46

7.1 Contributions of the systematic uncertainties associated with the SP and EP (in parentheses) v_n measurements for v_n in 5–10% and 40–50% centrality bins. The contributions are expressed in %. 62